

# **Short Range Correlations in Nuclei at Large $x_{bj}$ through Inclusive Quasi-Elastic Electron Scattering**

Zhihong Ye

Charlottesville, VA

A Dissertation presented to the Graduate Faculty  
of the University of Virginia in Candidacy for the Degree of  
Doctor of Philosophy

Department of Physics

University of Virginia

September, 2013

---

---

---

---

# Acknowledgements

Thanks!

## Abstract

E08-014 in Hall-A at Jefferson Lab aims to study the short-range correlations (SRCs) which is considered to explain the missing nuclear strength predicted by the mean field theory. The cross sections for  $^2H$ ,  $^3He$ ,  $^4He$ ,  $^{12}C$ ,  $^{40}Ca$ , and  $^{48}Ca$ , were measured via the inclusive quasielastic electron scattering from these nuclei in a  $Q^2$  range between 0.8 and 2.8 ( $GeV/c^2$ ) for  $x_{bj} > 1$ . The cross section ratios of heavy nuclei to  $^2H$  were extracted to study two-nucleon SRC for  $1 < x_{bj} < 2$ , while the study of three-nucleon SRC was proceeded by taking the cross section ratios of heavy nuclei to  $^3He$  for  $x_{bj} \geq 2$ . Meanwhile, the isospin dependence in SRCs has also been examined through the cross section ratio of  $^{48}Ca$  and  $^{40}Ca$ .

In this thesis, the theories of the nuclear structure and SRCs will be discussed followed by the introduction of the experimental setup. Then the detailed data analysis procedure will be given and preliminary results will also be presented.

# Contents

<b>1</b>	<b>Introduction</b>	<b>10</b>
1.1	Overview of Nuclear Structure . . . . .	10
1.2	Quasi-elastic Scattering . . . . .	14
1.2.1	Inclusive Cross Section . . . . .	16
1.2.2	Spectral Function and Momentum Distribution . . . . .	19
1.2.3	$y$ -Scaling . . . . .	21
1.2.4	Final State Interaction . . . . .	22
<b>2</b>	<b>Short Range Correlations in Nuclei</b>	<b>24</b>
2.1	The Features of SRCs . . . . .	25
2.1.1	Two-Nucleon Correlations . . . . .	27
2.1.2	Three-Nucleon Correlations . . . . .	29
2.1.3	Relativistic Approach . . . . .	30
2.1.4	Isospin Effect . . . . .	32
2.2	Probing SRCs using Electron-Nucleus Scattering . . . . .	34
2.2.1	Kinematics Conditions . . . . .	34
2.2.2	Inclusive Measurement . . . . .	36
2.2.3	Semi-Inclusive Measurements . . . . .	41
2.2.4	Triple-Coincidence Measurements . . . . .	43
2.2.5	Final State Interaction in SRCs . . . . .	44

		2
2.3	E08014 Experiment . . . . .	45
<b>3</b>	<b>Experiment Setup</b>	<b>47</b>
3.1	Overview . . . . .	47
3.2	Beam . . . . .	49
3.2.1	Beam Position Monitors . . . . .	50
3.2.2	Beam Charge Monitors . . . . .	50
3.2.3	Beam Energy . . . . .	51
3.3	Target System . . . . .	52
3.4	High Resolution Spectrometers . . . . .	55
3.5	Detector Packages . . . . .	56
3.5.1	Vertical Drift Chambers . . . . .	58
3.5.2	Scintillator Counters . . . . .	59
3.5.3	Gas Cherenkov Detectors . . . . .	59
3.5.4	Lead Glass Calorimeters . . . . .	61
3.6	Data Acquisition System . . . . .	62
3.7	Trigger Design . . . . .	64
<b>4</b>	<b>Calibration</b>	<b>67</b>
4.1	Overview . . . . .	67
4.2	Detector Calibration . . . . .	69
4.2.1	Gas Cherenkov Detectors . . . . .	70
4.2.2	Electromagnetic Calorimeters . . . . .	72
4.3	HRS Calibration . . . . .	75
4.3.1	Coordinator Systems . . . . .	77
4.3.2	Optics Optimization . . . . .	80
<b>5</b>	<b>Extracting Cross Sections</b>	<b>87</b>
5.1	Overview . . . . .	87

5.2	Electron Charge . . . . .	90
5.3	Dead-Time . . . . .	91
5.4	Targets . . . . .	93
5.4.1	Cryo-Target Boiling Study . . . . .	93
5.5	Detector Efficiencies . . . . .	95
5.5.1	Trigger Efficiency . . . . .	96
5.5.2	Vertical Drift Chamber Efficiency . . . . .	97
5.5.3	Particle Identification Efficiencies . . . . .	99
5.6	Monte Carlo Simulation . . . . .	104
5.7	Cross Section Model . . . . .	107
5.8	Event Selection and Corrections . . . . .	108
5.8.1	Acceptance Correction . . . . .	109
5.8.2	Central Momentum and Angle . . . . .	110
5.8.3	Binning Correction . . . . .	112
5.8.4	Cuts . . . . .	113
5.9	From Yields to Cross Sections . . . . .	115
5.10	Calculation of Errors . . . . .	116
5.10.1	Statistical Errors . . . . .	116
5.10.2	Systematic Errors . . . . .	118
<b>6</b>	<b>Results</b>	<b>120</b>
6.1	Yields . . . . .	120
6.2	Cross Sections . . . . .	120
6.3	Momentum Distribution . . . . .	121
6.4	SRC Ratio . . . . .	121
<b>A</b>	<b>Triggers in Data Analysis</b>	<b>126</b>

<b>B XEMC: A Package for Inclusive Cross Section Models</b>	<b>133</b>
B.1 Overview . . . . .	133
B.2 Code Structure . . . . .	134
B.3 Quasi-Elastic Cross Section Models . . . . .	134
B.3.1 QE-XEM . . . . .	137
B.3.2 QE-QFS . . . . .	139
B.3.3 QE-F1F209 . . . . .	139
B.4 DIS Models . . . . .	140
B.4.1 DIS-QFS . . . . .	140
B.4.2 DIS-XEM . . . . .	140
B.4.3 DIS-F1F209 . . . . .	141
B.5 Radiative Corrections . . . . .	141
B.6 Performance . . . . .	143
B.7 Examples . . . . .	144
<b>C Momentum Correction in HRS-R</b>	<b>145</b>
<b>D Non-Uniform Cryogenic Targets</b>	<b>151</b>
D.1 Boiling Study . . . . .	152
D.2 Extracting Density Distributions . . . . .	155
D.3 Absolute Density . . . . .	156
D.4 Radiative Correction . . . . .	157

# List of Figures

1.1	Two-nucleon potential distribution . . . . .	11
1.2	The nucleon energy shell structure and magic numbers . . . . .	12
1.3	Experiment measurements of spectroscopy factors . . . . .	13
1.4	Schematic of electron-scattering on a nucleus . . . . .	14
1.5	Electron energy transfer . . . . .	15
1.6	Schematic of inclusive QE electron scattering . . . . .	16
1.7	Spectral Function . . . . .	20
1.8	Final state interaction . . . . .	22
2.1	Nucleon momentum distribution . . . . .	26
2.2	Diagrams of 2N- and 3N-SRC . . . . .	27
2.3	Two types of 3N-SRC configuration . . . . .	29
2.4	Momentum distribution for proton and neutron and their ratio . . . . .	32
2.5	Isospin effect in momentum distribution . . . . .	33
2.6	Minimum momentum of the struck nucleon as function of $x_{bj}$ and $Q^2$ for Deuterium . . . . .	36
2.7	First evidence of 2N-SRC from SLAC . . . . .	37
2.8	2N-SRC and 3N-SRC results from Hall B . . . . .	39
2.9	2N-SRC and 3N-SRC results from E02-019 in Hall C . . . . .	40
2.10	Ratio of $^{56}Fe/^{2}H$ as a function of $x_{bj}$ and $\alpha_{2N}$ . . . . .	40

2.11	Proton Effective Momentum distribution in $^3He$	42
2.12	Angular correlation between nucleons in 2N-SRC	43
2.13	The fraction of $np$ pairs to $pp$ pairs in 2N-SRC	44
2.14	Kinematic Coverage of E08-014 experiment	45
3.1	The Jefferson Lab Accelerator	47
3.2	Side View of Hall-A	48
3.3	Top View of Hall-A	49
3.4	Schematic layout of beam instruments and spectrometers in HAll-A	50
3.5	Picture of cryogenic target loops	52
3.6	Target control screens	53
3.7	Schematic layout of HRS	55
3.8	HRS Detector Stack	57
3.9	Layout of VDCs	58
3.10	Design of Cerenkov Detector	60
3.11	Schematic layout of Calorimeters in HRS-L and HRS-R	62
3.12	Single arm trigger design	65
4.1	Alignment of gas Cherenkov detectors	70
4.2	Single electron peaks on both GCs	71
4.3	Calibration of calorimeters	74
4.4	Calibration performance and resolution of calorimeters	76
4.5	Hall Coordinate System (HCS)	77
4.6	Target Coordinate System (TCS)	78
4.7	Detector Coordinate System (DCS)	79
4.8	Transport Coordinate System (TRCS)	79
4.9	Focal Plane Coordinate System (FCS)	80
4.10	The Design of Sieve Slit Plates	82

4.11	$Z_{react}$ distribution before and after the optics calibration	84
4.12	Sieve slit pattern before and after the optics calibration	85
5.1	Flow-chart to extract cross section	89
5.2	Cryo-target Bumps on $z_{react}$ Distributions	94
5.3	Trigger Efficiency vs Run Number	98
5.4	Electron (blue) and pion (red) samples from the calorimeters	100
5.5	Electron and pion samples from the GC	100
5.6	Cut scan of the GCs and the calorimeters	101
5.7	PID cut on the GCs	102
5.8	PID cut on the calorimeters	104
5.9	Simulation of $^{12}C$ Target Plane Quantities	105
5.10	Simulation of $^3He$ Target Plane Quantities	106
5.11	A Sketch of Cross Section Lookup Tables	107
5.12	A demonstration of the acceptance effect	109
5.13	Central momentum deviation	111
6.1	$^2H$ Born Cross Sections	122
6.2	$^3He$ Born Cross Sections	122
6.3	$^4He$ Born Cross Sections	122
6.4	$^{12}C$ Born Cross Sections	123
6.5	$^{40}Ca$ Born Cross Sections	123
6.6	$^{48}Ca$ Born Cross Sections	123
6.7	Cross Section Ratio of $^4He$ to $^3He$	124
6.8	Cross Section Ratio of $^{12}C$ to $^3He$	124
6.9	Cross Section Ratio of $^{48}Ca$ to $^{40}Ca$	125
A.1	A scheme of events with different Trigger cuts	128
A.2	Another scheme of electrons with different Trigger cuts	131

B.1	Structure of XEMC Package	135
B.2	Input file for $^3He$ target	136
B.3	Target table for $F(y)$ parameters	138
B.4	Feynman diagrams for radiation effect	141
B.5	Comparing XEMC models and Experiment data	142
B.6	Check radiative correction using E02-019 data	143
C.1	$\delta p$ correction function fitting	149
C.2	The residual error of $\delta p$ correction function	150
C.3	$\delta p$ correction function applying on real data	150
D.1	Cryo-target density profiles from simulation	151
D.2	$^{12}C$ boiling effect fitting	152
D.3	Cryo-targets boiling effect fitting	154
D.4	Cryo-target density profiles from boiling study	158
D.5	Cryo-target boiling factor distribution	159
D.6	Cryo-target density distributions extracted from data	160
D.7	Cryo-targets relative density distribution	161

# List of Tables

3.1	Targets in E08-014 experiment . . . . .	54
3.2	Design characteristics of HRSs . . . . .	56
4.1	Spectrometer Offsets from Survey Reports . . . . .	81
4.2	Sieve Slit Plates Offsets from Survey Reports. . . . .	81
4.3	Run list of optics data. . . . .	82
5.1	Fraction of different tracks events from quasi-elastic data,w/o $\beta$ cut .	99
5.2	E' binning size and range . . . . .	113
5.3	E' binning size and range . . . . .	113
6.1	List of Kinematic settings and target measured on HRS-L . . . . .	121
6.2	List of Kinematic settings and target measured on HRS-R . . . . .	121
A.1	Triggers and their corresponding data types in data stream . . . . .	127
A.2	Events types with different Trigger cuts . . . . .	130
D.1	Cryo-targets densities . . . . .	157

# Chapter 1

## Introduction

The basic structure of an atom is understood as electrons orbiting around a dense central nucleus by attractive electromagnetic force. Modern scattering experiments discovered that the nucleus is further composed of nucleons which include protons with positive charges and electrically neutral neutrons. Understanding the structure of the nucleus remains as one of the biggest challenges in nuclear physics because of the complicated many-body interaction between nucleons. High energy electrons scattering on a nuclear target provides an essential probe to unveil the tiny structure of nuclei and nucleons. In this chapter, a brief review of nuclear structure examinations will be given, followed by a discussion of quasielastic (QE) electron scattering techniques.

### 1.1 Overview of Nuclear Structure

Compared with the general size of an atom, a nucleus is nearly  $10^6$  times smaller ( $\sim 1.2 \text{ fm}$ ), which, however, is a complicated many-body system where nucleons are bound by strong interactions. To fully understand the detailed structure of the nucleus, one needs to have the complete knowledge of each nucleons' eigen-state. For a light nucleus with only few nucleons, the wave functions can be directly calculated

using variational methods [1]. However, for medium and heavy nuclei ( $A \geq 12$ ), the explosion of degree of freedom in the Hamiltonian makes it impossible to obtain the solution.

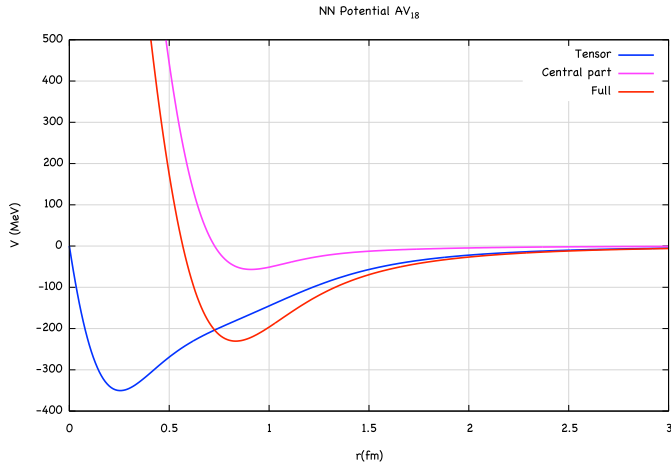


Figure 1.1: Two-nucleon potential distribution [2], where the blue line represents the tensor force which responds most of the attractive part.

Furthermore, the particular behaviour of the interaction potential between nucleons also increases the complexity of the nuclear system. As shown in Fig. 1.1, two nucleons experience weak attractive interaction at moderate distance. As they get closer, the strong attractive force, mainly caused by the tensor components of spin and isospin channels, forms a deep potential well. At much short distance, the hard-core interaction between nucleons generates strong repulsion which prevents the nucleus from further collapses. The Coulomb force between protons and potential three-body forces also play a role but they are much weaker compared with the strong force.

Despite the complexity of the nucleus, Scattering experiment observed the spectrometers of nucleons which reveal that nucleons behave more like independent particles in nuclear medium due to the collective effects of Pauli principle and the strong short-distant interactions with surrounding nucleons. Nucleons occupy different energy shells similar to the arrangement of electrons orbiting around the nucleus. Moreover, some nuclei have much stronger binding energies when they are composed of certain

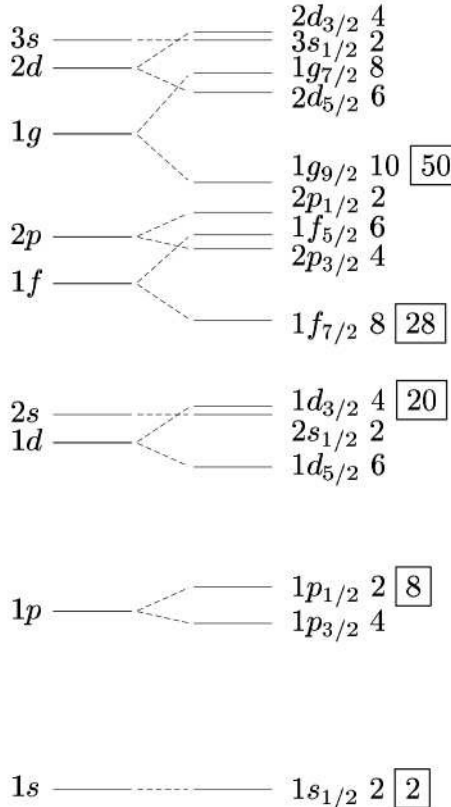


Figure 1.2: The nucleon energy shell structure and magic numbers. The fine structure of each energy shell is due to the spin-orbit coupling. The magic numbers are shown in the boxes.

numbers of nucleons, namely **magic numbers**.

The explanation of these phenomena has been successfully approached by the **independent particle shell model** (IPSM), in early circumstance also called as the **mean field theory**. In this theory, the nucleus is treated as a non-relativistic object where nucleons interact only through two-body interaction. Nucleons tend to occupy the lowest energy state first and the energy of the last occupied state is called the **Fermi energy**. The whole set of occupied energy levels is called the **Fermi sea**. The energy state of each nucleon can be individually obtained by solving the Schrödinger equation with the mean field potential. Combined with the spin-orbit coupling, IPSM successfully predicts the ground state properties, the excitation of nuclei at low energy, nuclear spins and parities, as well as the prediction of nuclear

magic numbers. However, IPSM shows its limitation in predicting the nuclear magnet moments and highly excited energy states.

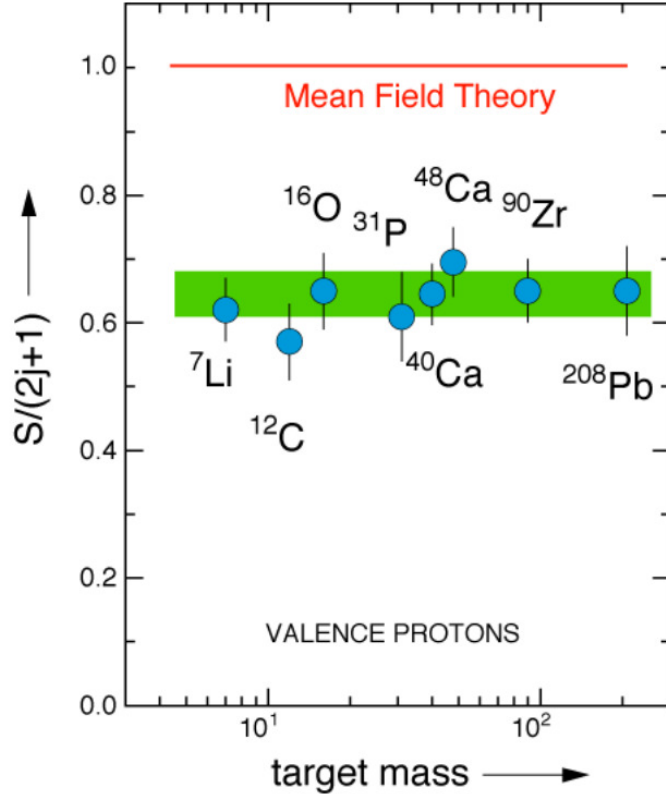


Figure 1.3: Experiment measurements of spectroscopy factors for different nuclei deviate from one, indicating the important role of correlations between nucleons.

A useful experimental observable, called **Spectroscopy Factor**, denotes the amplitudes of adding or removing one nucleon from the nucleus. In IPSM, assuming nucleons occupy  $j$  orbits in the nuclear shell, the cross section of removing one nucleon is then written as,  $\sigma_{removing} = S \cdot \sigma_{sp}$ , where  $\sigma_{sp}$  is the single-particle cross section, and the spectroscopy factor,  $S$ , should obey a sum role:

$$\frac{S}{(2j+1)} \equiv 1, \quad (1.1)$$

where the factor  $(2j+1)$  denotes the maximum energy states of the nucleon. Several measurements [3, 4] with medium-energy proton-knock experiments in early 1970s

measured the values of spectroscopy factor for heavy nuclei (Fig. 1.3) which is 30% – 40% lower than one. Even advanced Hartree-Fock calculations [5] involving long range nucleon-nucleon interaction still overestimate the nuclear strength.

An explanation of the missing strength is based on the short distance property of nucleon-nucleon strong repulsive interaction. IPSM restricts nucleons in their energy states below the Fermi momentum ( $250 \text{ MeV}/c$ ). However, when two nucleons stay close due to the attractive potential, the repulsive force starts to dominate the interaction and results in high relative momentum significantly exceeding the Fermi momentum. However, the total momentum of such two nucleons is still relatively too small to excite the nucleus so the nucleons remains in its ground state. The measurement of knocking out any such highly correlated nucleons yields the nuclear strength beyond the prediction of mean field theory. Such effect is generally called short range correlations (SRCs), which will be carefully discussed in next chapter.

## 1.2 Quasi-elastic Scattering

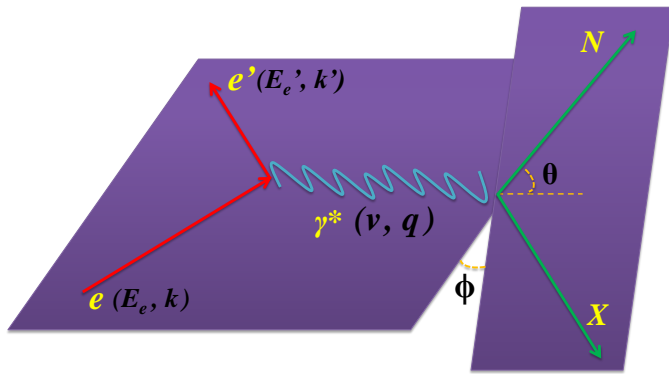


Figure 1.4: Schematic of electron-scattering on a nucleus

An electron with predefined initial energy and final energy,  $E_e$  and  $E'_e$ , interacts with a charged nucleus by exchanging a virtual photon with the energy transfer,  $\nu = E_e - E'_e$  (Fig. 1.4). By varying the amplitude of the energy transfer, one can

probe the nucleus at different scales. At low energy transfer, electrons interact with the entire nucleus and the measurement of elastic cross section is generally applied in the study of nuclei and nucleons form factors [6].

As shown in Fig. 1.5 [7], a process of quasi-elastic (QE) electron-nucleon scattering appears with larger energy transfer, and the Fermi motion of the nucleon in the nucleus results an broad distribution compared to the shape elastic peak. Nucleons are excited at even larger energy transfer and resonances start to contribute to the cross section.

Electrons directly probe the quarks properties at very large energy transfer through the process of deep inelastic scattering (DIS).

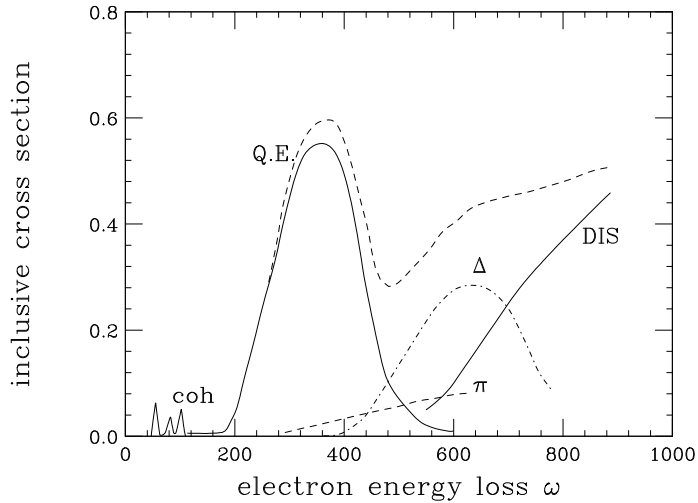


Figure 1.5: Inclusive cross section on the y-axis versus the energy loss,  $\omega = \nu = E_e - E'_e$ , on the x-axis.

A convenient parameter for identifying different processes in the scattering is the Bjorken variable,  $x_{bj} = Q^2/(2m_N\nu)$ , where  $m_N$  is the nucleon mass. The original definition of  $x_{bj}$  is the momentum fraction of the quark constituents from the nucleon during the DIS scattering. In electron-nucleon scattering, the elastic peak locates at  $x_{bj} = 1$ , while for inelastic process,  $0 < x_{bj} < 1$ . In electron-nucleus scattering,  $x_{bj}$  extends to the region of  $0 < x_{bj} < M_A/m_N$ ,  $x_{bj} = 1$  is now the location of the

quasi-elastic peak, and the elastic peak moves to  $x_{bj} = M_A/m_N$ . For convenience,  $m_N$  is usually replaced by the proton mass during the experimental data analysis, as used in the rest of this thesis:

$$x_{bj} = Q^2/(2m_p\nu). \quad (1.2)$$

During the quasi-elastic scattering, an electron knocks a nucleon out from the nucleus (Fig. 1.4), which provides a opportunity to study the property of nuclear structure. In the picture of plane-wave impulse approximation (PWIA), the exclusive electron scattering cross section is the sum of the cross sections of the individual nucleons as: [8]:

$$\frac{d^5\sigma}{dE'_e d\Omega_e d^3p'} = \sum_{nucleons} \sigma_{eN} \cdot S'_N(E_0, \vec{p}_0), \quad (1.3)$$

where  $S'_N(E_0, \vec{p}_0)$ , called the nuclear spectral function, is the probability of removing a nucleon with initial energy  $E_0$ , and momentum  $\vec{p}_0$  from the target nucleus [7], and  $\sigma_{eN}$  is the electron-nucleus cross section.

### 1.2.1 Inclusive Cross Section

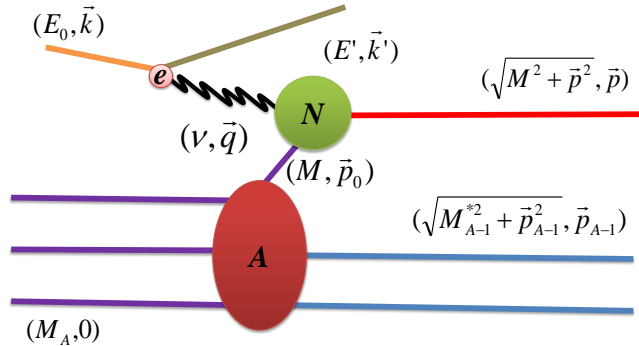


Figure 1.6: Schematic of inclusive QE electron scattering where  $\vec{p}_{A-1} = -\vec{p}_0$  for fixed targets.

As shown in Fig. 1.6, the inclusive electron scattering cross section is measured

by only detecting the scattered electrons ( $\sqrt{M^2 + \vec{p}^2}$ ,  $\vec{p}$ ), while the final state of the  $(A - 1)$  recoil system, ( $\sqrt{M_{A-1}^2 + \vec{p}_{A-1}^2}$ ,  $\vec{p}_{A-1}$ ), remains unknown. To obtain the inclusive cross section from Eq (1.3), one separates the contributions from protons and neutrons, and integrates over the final states of the nucleons:

$$\frac{d^3\sigma}{dE'd\Omega} = \int (Z\sigma_{ep}S'_p(E_0, \vec{p}_0) + N\sigma_{en}S'_n(E_0, \vec{p}_0))d^3\vec{p}, \quad (1.4)$$

where the subscripts in  $dE'_e d\Omega_e$  have been omitted since only electrons are measured.

Assuming the spectral function is spherically symmetric, and if the difference in the spectral function between protons and neutrons is ignored, the more general form  $S'(E_0, p_0)$  can be factored out from the equation. Since  $\vec{p} = \vec{p}_0 + \vec{q}$ , where  $\vec{q}$  is fixed when measuring  $E_0$  and  $E'$ , one can replace  $d^3\vec{p}$  by  $d^3\vec{p}_0$ . In the spherical coordinate,  $d^3\vec{p}_0 = p_0^2 dp_0 d(\cos\theta) d\phi$ , and the cross section becomes:

$$\frac{d^3\sigma}{dE'd\Omega} = 2\pi \int \tilde{\sigma}_0 \cdot S'(E_0, p_0) \cdot p_0^2 dp_0 d(\cos\theta) \quad (1.5)$$

where

$$\tilde{\sigma}_0 = \frac{1}{2\pi} \int_0^{2\pi} (Z\sigma_{ep} + N\sigma_{en}) d\phi. \quad (1.6)$$

Eq (1.5) can be further simplified by considering the energy conservation. From Fig. 1.6, for the fixed target,  $\vec{p}_{A-1} = -\vec{p}_0$ , which gives:

$$M_A = E_0 + \sqrt{M_{A-1}^{*2} + p_0^2}, \quad (1.7)$$

and,

$$M_A + \nu = \sqrt{M^2 + (\vec{p}_0^2 + \vec{q}^2)} + \sqrt{M_{A-1}^{*2} + \vec{p}_0^2}, \quad (1.8)$$

where  $M$ , and  $M_A$  are the mass of the ejected nucleon and the target nucleus, respectively.  $M_{A-1}^*$  is the mass of the recoiling  $(A - 1)$  system, where the superscript \*

means it could be in its excited state. Eq 1.5 becomes [8]:

$$\frac{d^3\sigma}{dE'd\Omega} = 2\pi \int \tilde{\sigma}_0 \cdot \frac{E_N}{|\vec{p}_0||\vec{q}|} \cdot S'(E_0, p_0) \cdot p_0^2 dp_0 dE_0 \quad (1.9)$$

where  $E_N = \sqrt{M^2 + \vec{p}}$  denotes the energy of the struck nucleon.

One can define the separation energy,  $E_s \equiv M_{A-1}^* + M - M_A$ . Then the spectral function becomes  $S(E_s, p_0) \equiv -S'(E_0, p_0)$ , where the Jacobian transformation factor from  $E_0$  to  $E_s$  has been absorbed into the new definition [8]. One can define  $\tilde{\sigma} = \tilde{\sigma}_0 \cdot E_N / |\vec{q}|$ , and rewrite the cross section as:

$$\frac{d^3\sigma}{dE'd\Omega} = 2\pi \int_{E_s^{min}}^{E_s^{max}} \int_{p_0^{min}}^{p_0^{max}} \tilde{\sigma} \cdot S(E_s, p_0) \cdot p_0 dp_0 dE_s, \quad (1.10)$$

where  $p_0^{min}$  and  $p_0^{max}$  are the solution of Eq (1.8) when  $\vec{p}_0$  and  $\vec{q}$  are parallel:

$$M_A + \nu = \sqrt{M^2 + y^2 + 2yq + q^2} + \sqrt{M_{A-1}^{*2} + y^2}, \quad (1.11)$$

where two solutions,  $y_1$  and  $y_2$  ( $y_1 < y_2$ ), give the values of  $p_0^{min}$  and  $p_0^{max}$ , respectively. While  $E_s^{min}$  corresponds to the minimum separation energy when the recoil nucleus is in its ground state,  $E_s^{max}$  is the maximum separation energy when the struck nucleon is at rest:

$$E_s^{max} = \sqrt{(M_A + \nu)^2 - q^2} - M_A. \quad (1.12)$$

which leads to  $p_0^{min}(E_s^{max}) = p_0^{max}(E_s^{max})$ .

### 1.2.2 Spectral Function and Momentum Distribution

In the shell model, nucleons move as independent particles in a mean field and the spectral function can be written as [7]:

$$S_{MF}(E_0, \vec{p}_0) = \sum_{n \in F} |\phi(\vec{p}_0)|^2 \delta(E_0 - E_n), \quad (1.13)$$

where  $\phi_{\vec{p}_0}$  is the wave function in momentum space for a nucleon with the eigen-state  $E_n$ , and the sum is over all occupied states.

The validity of the mean field theory can be examined by studying the distribution of the spectral function as a function of  $E_0$  through electron-nucleon and hadron-nucleon knock-out experiments.

\*(show the plot)\* The peaks in the distribution correspond to knocking out nucleons from orbits defined by shell model and any discrepancy indicates the effect of nucleon-nucleon interaction.

The full spectral function includes an extra term to take into account the effect [7]:

$$S(E_0, \vec{p}_0) = S_{MF}(E_0, \vec{p}_0) + S_{Corr}(E_0, \vec{p}_0), \quad (1.14)$$

The correlation term provides an important test of advanced interacting shell model calculations thought direct experimental measurements base on the normalization requirement:

$$\int S(E_0, \vec{p}_0) d^3 \vec{p}_0 dE_s = 1. \quad (1.15)$$

The integral of the spectral function over the separation energy leads to the momentum distribution:

$$n(p_0) = \int_{E_s^{min}}^{\infty} S(E_s, p_0) dE_s. \quad (1.16)$$

The momentum distribution is a sensitive probe to examine the effect of the nuclear medium and nucleon-nucleon interactions. At momenta above the Fermi momentum,

$k_F$ , the mean field effect vanishes and strong short range correlations of the nucleons emerge.

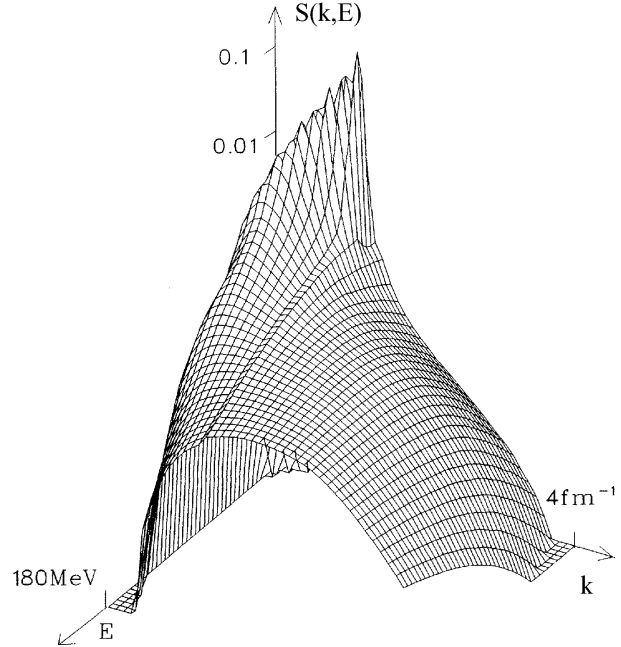


Figure 1.7: Spectral Function versus separation energy  $E_s$  and transfer momentum  $p_0$  [7].

Because the spectral function decreases rapidly by orders of magnitude toward  $E_s^{max}$  and  $p_0^{max}$ , see Fig. 1.7, the upper limits of the two integrals in Eq (1.10) can be extended to infinity. Meanwhile,  $\tilde{\sigma}$  changes very slow as a function of  $E_s$  and  $p_0$  so can be factored out from the integral and evaluated at the maximum value of the spectral function at  $E_s = E_s^0$ . Hence Eq (1.10) can be rewritten as:

$$\frac{d^3\sigma}{dE'd\Omega} = 2\pi\bar{\sigma} \int_{E_s^{min}}^{\infty} \int_{p_0^{min}}^{\infty} S(E_s, p_0) \cdot p_0 dp_0 dE_s, \quad (1.17)$$

where  $\bar{\sigma} \propto \tilde{\sigma}(E_s^0, p_0^{min})$  [9]. The model of  $\bar{\sigma}$  is usually taken from the prescription by

De Forest [10], shown as [8]:

$$\bar{\sigma} = \frac{1}{Z\sigma_p + N\sigma_n} \frac{|\vec{q}|}{\sqrt{M^2 + (y + \vec{q})^2}}. \quad (1.18)$$

### 1.2.3 y-Scaling

The spectral function is directly connected to the momentum distribution, but it is not an experimental observable. Instead, one can examine the scaling behavior [11] of inclusive quasielastic scattering cross section. The scaling function can be defined as [12, 13]:

$$F(y, q) = 2\pi \int_{E_s^{min}}^{\infty} \int_{|y|}^{\infty} S(E_s, p_0) \cdot p_0 dp_0 dE_s. \quad (1.19)$$

where the new variable,  $y$ , is defined as the minimum values of momentum in Eq (1.8),  $p_0^{min} = |y|$ , when the  $A - 1$  system is in its ground state:

$$M_A + \nu = \sqrt{M^2 + q^2 + y^2 + 2yq} + \sqrt{M_{A-1}^2 + y^2}. \quad (1.20)$$

If only the nucleonic degrees of freedom are considered, the scaling function becomes independent of  $\vec{q}$  at large momentum transfer [13]. Hence,  $F(y, q) \equiv F(y)$ . From Eq (1.17), the scaling function can be extracted from electron-nucleon scattering cross section for an off-shell nucleon:

$$F(y) = \frac{d^3\sigma}{dE'd\Omega} \frac{1}{Z\sigma_p + N\sigma_n} \frac{q}{\sqrt{M^2 + (y + q)^2}}. \quad (1.21)$$

Due to the Fermi motion, the broad quasielastic peak of the inclusive cross section is mixed with the tails of resonance and DIS components, as shown in Fig. 1.5. To extract  $F(y)$  from the experimental cross section, one needs to utilize a cross section model to remove the contribution from DIS region,  $\sigma_{QE} = \sigma_{Exp} - \sigma_{DIS}^{model}$  (See Appendix B).

By reversing the order of the integration in Eq 1.19 and based on Eq (1.16),  $F(y)$  can be rewritten as:

$$F(y) = 2\pi \int_{|y|}^{\infty} n(p_0) \cdot p_0 dp_0. \quad (1.22)$$

Hence the momentum distribution can be extracted experimentally by measuring the  $F(y)$  distribution [7]:

$$n(p_0) = \frac{-1}{2\pi p_0} \frac{dF(p_0)}{dp_0} \Big|_{p_0=|y|}, \quad (1.23)$$

where an assumption The scaling of  $F(y)$  is supposed to be valid in the limit of very large momentum transfer where the effects due to final-state interactions and the error made by extending the upper limit of Eq (1.22) to infinity can be neglected. Meanwhile, the assumption that the lower limit ( $p_0^{\min} = |y|$ ) is independent of  $E_s$  is also needed to be verified. The momentum distribution can be extracted from data in the scaling region, but the data in the region of approaching to scaling is also important to verify those assumptions.

#### 1.2.4 Final State Interaction

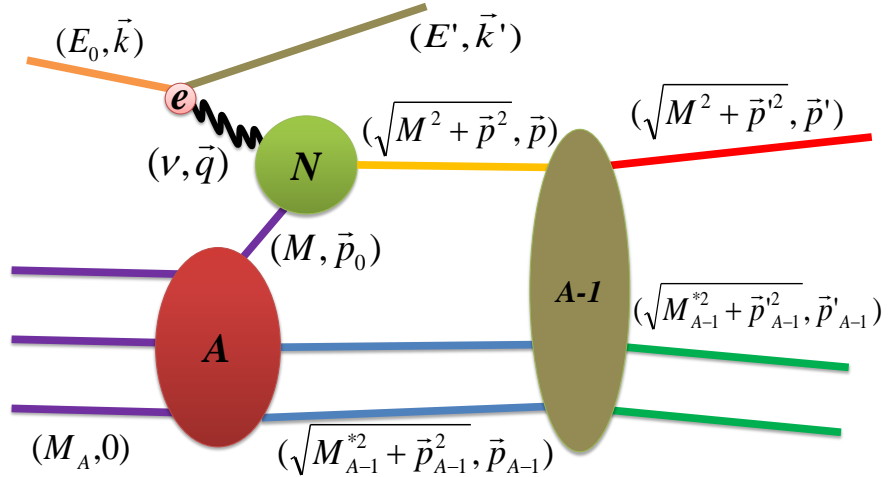


Figure 1.8: General diagram of final state interaction. The struck nucleon is re-scattered by the  $A - 1$  system and its final momentum is modified.

Final State Interaction (FSI) is the effect of the struck nucleon being re-scattered by the  $A - 1$  recoil system. In PWIA, the nucleons in the nucleus are treated as individual constituents and the space resolution of the electron probe is approximately  $1/q$ . Hence, in the inclusive cross section measurement at large  $Q^2$ , FSI is negligibly small, based on the fact that the interaction time between the virtual photon and the struck nucleon is significant smaller than the one between the struck nucleon and the recoil system.

However, comparison between the theoretical calculation and experimental results [14, 15] shows the violations of y-scaling for heavy target which indicates FSI still plays a significant role in the scattering process even at large  $Q^2$ . (MORE discussion)

## Chapter 2

# Short Range Correlations in Nuclei

The mean field theory has its great success in description of the nuclear structure as individual nucleons moving in the average mean field, and their energy and momenta are below the Fermi energy and the Fermi momentum, i.e.,  $\epsilon < \epsilon_F$  and  $k < k_F$ . However, the theory provides limited ability to study the short range properties of nucleon-nucleon (NN) interaction and fails to describe the structure of nuclear matter beyond the saturation density. Short Range Correlations (SRCs) provide an successful explanation of such discrepancy by examining the high momentum component of the nucleon momentum distribution at  $k > k_F$ . The attractive and repulsive potential between nucleons at short distance ( $\sim 1.0$  fm) excite the nucleons from their single shell and cause the significant increase of strength to the nuclear spectral function.

The existence of high energy and high luminosity electron accelerators, i.e., SLAC and JLab, provided a good opportunity to directly probe the short-distance properties of the nucleon-nucleon (NN) interaction. Early experiments in SLAC conformed the evidence of SRCs and recent experiments in JLab extended the study to map out the strength of SRCs in a wider range of nuclei and examined the isospin effect in SRCs. In this chapter, the new development of theoretical understandings of nuclear properties will be carefully explained and the experimental techniques to explore

SRCs will be briefly reviewed.

## 2.1 The Features of SRCs

To understand why the mean field theory fails to predict the nuclear strength and how SRCs attribute to the explanation of the missing nuclear strength, one needs to examine the modern nucleon momentum distributions which directly relate to the nucleon properties in the nucleus. While the prediction of mean field theory gives a rapid fail-off curve at momenta approaching  $k_F$ , shown in Fig. 2.1, experimental results [16] present the momentum tail with much slow falloff at  $k > k_F$  which is similar for all nuclei from Deuterium to nuclear matter. The results strongly argues again the mean field prediction, but can be easily understood if the high momentum tails are generated by the short-range part of NN interactions, i.e., SRCs.

From Fig. 1.1, nucleons interact at very short distance via the attractive potential which is mainly contributed by the tensor force, but their strong repulsive hard-cores prevents them to further collapse. Such dramatic processes create a correlated configuration with large relative momenta. The excitation of nucleons from these configurations significantly increase the momentum strength at  $k > k_F$  which is not predicted by the mean field theory. However, the excitations are not related to any real excited statuses of the nucleus since the total momentum of the correlated nucleons is relatively small.

In the picture of SRCs, the asymptotic form of momentum distribution can be broke down into several regions. At  $k \leq k_F$ , the strength is mainly contributed by the mean field potential. At the momentum range  $300 < k < 600$  MeV/c, the contribution of the mean field effect vanishes and the effect of two-nucleon short range correlation (2N-SRC) becomes dominant. The nucleons in this configuration carry large and back-to-back momenta, while the total momentum of the NN pair

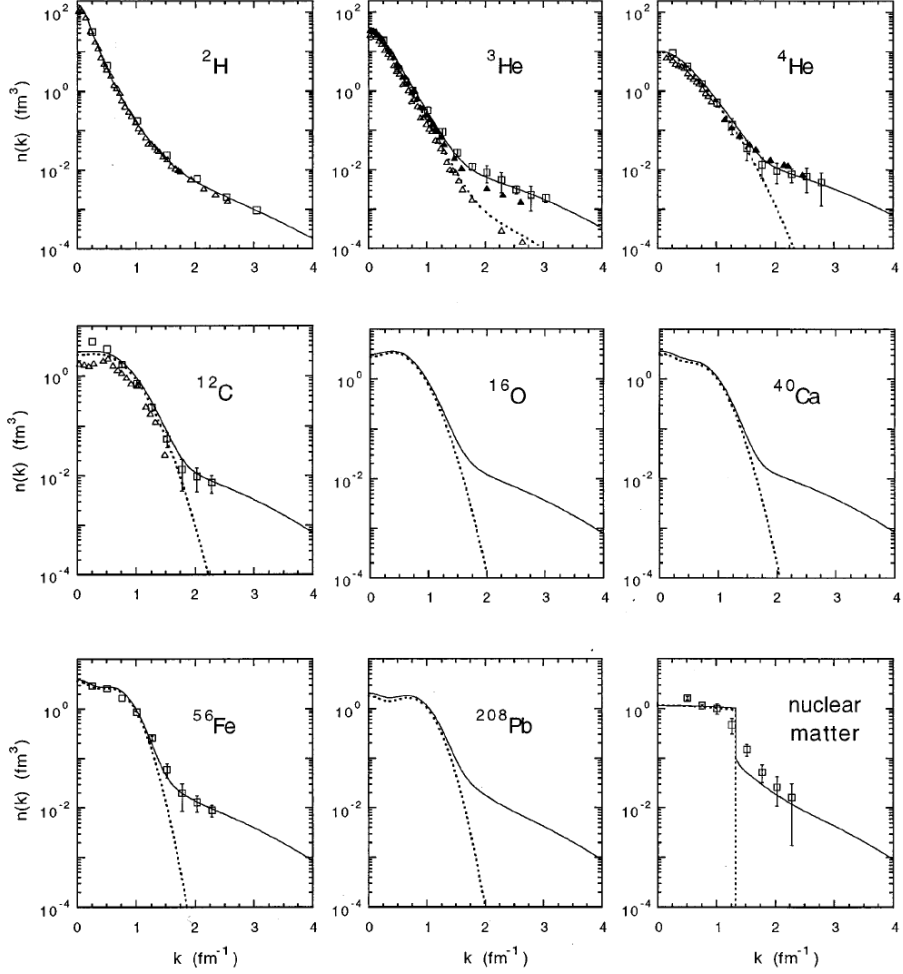


Figure 2.1: Nucleon momentum distribution for various nuclei [16], where dotted lines are from a mean field calculation, solid lines are from calculations involving SRCs. Dots are from experimental data.

is negligible. Due to the fact that the NN attraction is dominated by the tensor components which produce iso-singlet pairs, i.e.,  $(np)_{I=0}$ , one expects to see the high momentum tails of heavy nuclei to be identical to the one of deuteron, as shown in Fig. 2.1. The configuration of 2N-SRC breaks down at much higher momentum limit ( $600 \leq k \leq 800$  MeV/c) where the isospin-independent repulsive core begins to dominate, and the inclusion of three-nucleon short range correlation (3N-SRC) should be manifested [17]. However, 3N-SRC is not as significant as 2N-SRC since it is the result of the interaction of two-body interaction. At extremely high  $k$  limit

where the nucleon kinetic energy is comparable with the excitation energy of nucleons, non-nucleonic degree-of-freedom may be needed to be considered [17].

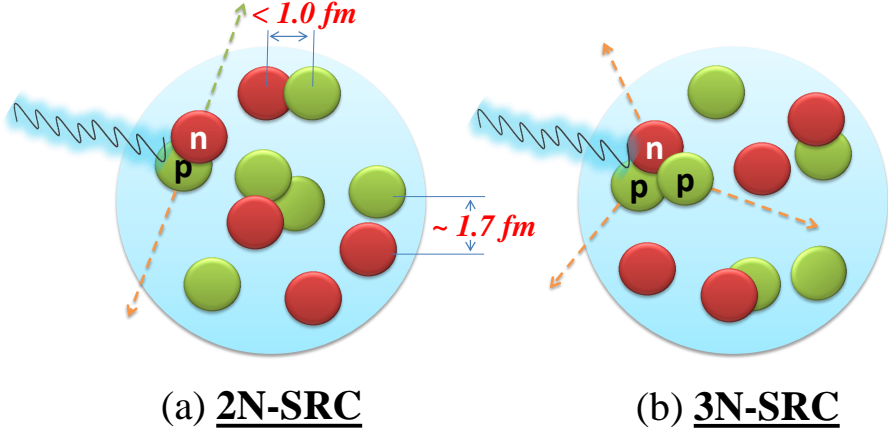


Figure 2.2: Diagram of 2N- and 3N-SRC. On the left diagram the virtual pion breaks up the 2N-SRC pair in back-to-back ejection, and on the right diagram the break-up of 3N-SRC configuration results in correlated nucleon ejecting in different direction so their total momentum remains at zero.

### 2.1.1 Two-Nucleon Correlations

The dominance of 2N-SRC in the nucleus should yield an momentum distribution proportional to the one of Deuterium at  $k > k_F$ :

$$n_A(k) = a_2(A, Z) \cdot n_D(k), \quad \text{for } k > k_F, \quad (2.1)$$

where  $n_D(k)$  denotes the momentum distribution of deuterium and  $a_2(A, Z)$  relates to the probability of finding such two-nucleon configuration in the nucleus with nuclear number  $A$  and proton number  $Z$ . One can study the scaling of  $a_2$  as the function of  $k$ , by taking ratio of momentum distribution of different nuclei to Deuterium,  $n_A(k)/n_D(k)$ .

The momentum distribution can be reconstructed from the ground state wavefunction but is not an experimental observable. Instead, one studies SRCs through

the spectral function which directly relates to the cross section of physical processes (Eq 1.3). Similar to the definition in the shell model (Eq (1.13)), one can define the spectral function as [18]:

$$S_A(E_R, p_i) = | \langle \phi_{A-1} | \delta(-p_i^2/(2m_{A-1}) + E_R - E_m) a(k) | \psi_A \rangle |^2, \quad (2.2)$$

which represents a product of the probability of finding a nucleon in the nucleus with initial momentum  $p_i$ , and the probability of the residual system carrying recoil energy  $E_R$  after the removal of this nucleon.  $a(k)$  denotes an operator to remove a nucleon from the nucleus A,  $E_m$  depends on A and represents the excitation energy of the  $A - 1$  system at rest, and  $-p_i^2/(2m_{A-1})$  is the kinetic energy of the center of mass.

When a nucleon in the 2N-SRC configuration is instantly knocked out by a high energy probe, its paired nucleon with an equal momentum is rejected in the opposite direction, while the  $A - 2$  residual nucleus remains unperturbed ( $E_m \sim 0$ ). When only the knock-out nucleon is interested, the kinetic energy of the correlated nucleon is shared by the entire  $A - 1$  system. From Eq (2.2) the average recoil energy of the  $A - 1$  system can be approximately given as:

$$\langle E_R \rangle_{2N-SRC} \sim \frac{p_i^2}{2m_N}. \quad (2.3)$$

Since  $E_R$  directly relates to the initial momentum of the nucleon in 2N-SRC, and the spectral function links to the momentum distribution (Eq. (1.16)), observation of the correlation between the spectral function and  $E_R$  enables one to examine the contribution of SRCs but however, it is not uniquely sensitive to SRCs. Indeed, any processes that involving NN interaction, such as meson exchange currents, yields the same result in Eq (2.3). One can check the dominance of the SRCs by applying additional kinematic conditions to suppress long range NN interactions, which will be discussed in next section.

### 2.1.2 Three-Nucleon Correlations

Similar to the Deuterium-like configuration of the 2N-SRC pair, The momentum distribution of a nucleon in a 3N-SRC configuration should be identical to the case in  $^3H$  (pnn) and  $^3He$  (ppn). For example,

$$n_A(k) = a_3(A, Z) \cdot n_{^3He}(k), \quad \text{for } k > 800 \text{ MeV}/c, \quad (2.4)$$

where similarly,  $n_{^3He}(k)$  is the momentum distribution of  $^3He$  and  $a_3(A, Z)$  is the probability of finding three-nucleon configuration in the nucleus  $A$ .

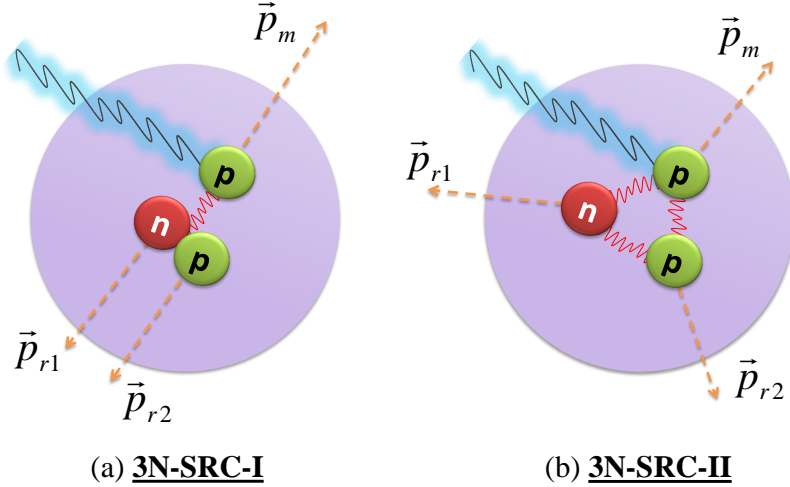


Figure 2.3: Two types of 3N-SRC configuration [18].

However, the configuration of 3N-SRC is more complicated compared with the simple back-to-back picture of 2N-SRC. In general, there are two types of 3N-SRC, as shown in Fig. 2.3. The first type, namely 3N-SRC-I, is the situation of two nucleons share the initial momentum which is equal to the struck nucleon but in the opposite direction, a configuration similar to 2N-SRC but involving three nucleons. The effect of 3N-SRC-I typically dominates at  $p_i \geq 600 \text{ MeV}/c$  with the average recoil energy of

the  $A - 2$  residual system:

$$\langle E_R \rangle_{3N-SRC-I} \sim \frac{p_i^2}{4m_N}. \quad (2.5)$$

which is approximately equal to one half of the recoil energy in 2N-SRC. This configuration gives the major contribution in the kinematic region of 3N-SRC.

The second type, 3N-SRC-II, refers to the configuration of three nucleon carrying momenta all exceeding the Fermi momentum in three different direction, and the average recoil energy of the residual system in this configuration is:

$$\langle E_R \rangle_{3N-SRC-II} \sim \frac{p_i^2}{m_N}, \quad (2.6)$$

which is larger than the average recoil energy of 3N-SRC-I, indicating the probability of 3N-SRC-II is more rare than the one of 3N-SRC-I, although the former one is easier to be observed experimentally.

Eq (2.3), Eq (2.5) and Eq (2.6) reveal that the average recoil energy of 2N-SRC is in between the two average recoil energies of 3N-SRC, and for 2N-SRC the distribution of  $E_R$  as a function of  $p_i$  is very broad, so its capability of identifying contributions from 2N-SRC and 3N-SRC to the spectral function is limited. New kinematic quantities are needed to separate these two processes, and are introduced next.

### 2.1.3 Relativistic Approach

The high energy process of knocking out short range correlated nucleons with very high momenta make one more naturally to apply the study of SRCs in the relativistic regime. A relativistic projectile moving along the z-direction probe the light-cone (LC) wave-function of the nucleus,  $\psi_A(\alpha_1, k_{1,t}, \dots, \alpha_i, k_{i,t}, \dots, \alpha_A, k_{A,t})$ , where the LC

variable is defined as [18]:

$$\alpha_i = A \left( \frac{E_i - p_{i,z}}{E_A - p_{A,z}} \right) = A \left( \frac{E_i^{lab} - p_{i,z}^{lab}}{M_A} \right), \quad (2.7)$$

where  $(E_i - p_{i,z})$  and  $(E_A - p_{A,z})$  are the initial energy and longitudinal momentum of constituent nucleons and the target nucleus,  $A$ , respectively.  $\alpha_i$  is invariant under Lorentz boosts in the z-direction. In the rest frame of the nucleus,  $E_A - p_{A,z} = M_A$ , where  $M_A$  is the nuclear mass.

Similar to the definition of  $x_{bj}$  in inelastic scattering (Eq 1.2),  $\alpha_i$  denotes the LC fraction of the nucleus momentum carried by the nucleon, hence  $\sum_i^A \alpha_i = A$ . While  $\alpha_i \leq 1$  limits the momentum fraction of the nucleon carried by the quark, to have  $\alpha_i > 1$  requires at least two nucleons involved in the scattering. Furthermore, three nucleons are required to share their momentum to have  $\alpha_i > 2$ . Consequently,  $\alpha_i$  becomes an ideal variable to distinguish between 2N-SRC and 3N-SRC. Considering the energy and momentum conservation law for the nucleon knock-out with a virtual photon from the nucleus, one can rewrite the LC variable as [17]:

$$\alpha_i = x_{bj} \left( 1 + \frac{2p_{i,z}}{\nu + |\mathbf{q}|} \right) + \frac{W_N^2 - m_i^2}{2m_i\nu}, \quad (2.8)$$

where  $\nu$  and  $\mathbf{q}$  is the energy and momentum transfer of the virtual photon, respectively, and  $W_N^2 = (\mathbf{p}_i + \mathbf{q})^2$ . For the quasi-elastic process,  $W_N \simeq m_i$  yields a simple connection between  $\alpha_i$  and  $x_{bj}$ . At sufficiently large  $Q^2$ ,  $\alpha_i$  is usually replaced by  $x_{bj}$ :

$$\alpha_i \rightarrow x_{bj}, \quad (2.9)$$

when  $Q^2 \rightarrow \infty$ . However, these two variables have distinct differences for  $Q^2$  values in few  $GeV^2$  range. One needs to examine the different scaling of SRCs as a function of  $x_{bj}$  and  $\alpha_i$  at the region of low  $Q^2$  values.

### 2.1.4 Isospin Effect

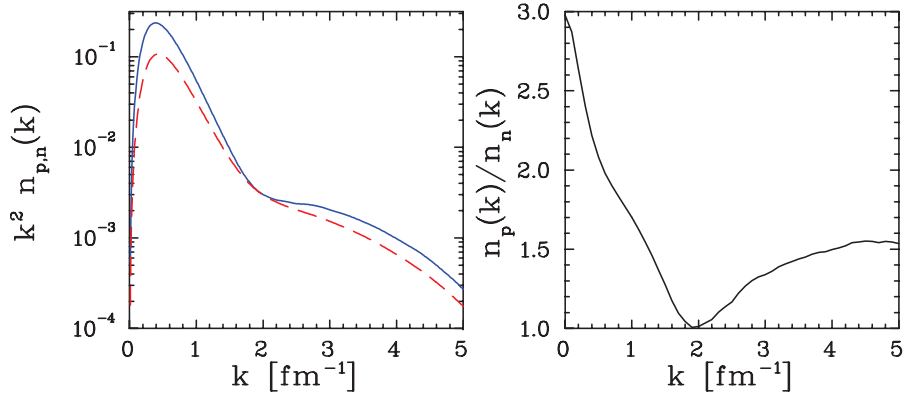


Figure 2.4: Left: Momentum distribution for proton (solid) and neutron (dashed) in  $^3He$ ; Right: Ratio of proton to neutron momentum distribution. Plots were originally from ??.

Early analysis assumed the isospin-independence of SRCs, which means that the ratio of neutrons to protons in SRCs is equal to the  $N/Z$  ratio of the nucleus. However, numerical studies [19] and experiments [20] reveal that the tensor interaction dominates the attractive potential of 2N-SRC. Accordingly, one expects that 2N-SRC pairs should be mainly in iso-singlet ( $np, T = 0$ ) states. The iso-triplet ( $pp, np$  and  $nn, T = 1$ ) pairs can be close together without interacting strongly until their repulsive forces become strong [17].

Fig. 2.4 shows a calculation of the momentum distribution for protons and neutrons and their ratio in  $^3He$  [21]. In the assumption of isospin-independence, the momentum ratio of protons to neutrons should be equal to two, but if the SRCs are isospin-dependent, the ratio becomes one when SRCs dominate at  $k > k_F$ . The left plot gives the value of the ratio at  $k > k_F$  roughly equal to 1.5, which suggests

that the isospin effect largely deviates from the assumption of isospin independence. The reason why  $np_{T=0}$  configuration does not totally dominates is that the  $T = 1$  channels are not completely suppressed, especially at very large momentum, where the configuration of 3N-SRC is more complicated. Another calculation [22] extended the study to other nuclei provides the similar results. Shown in Fig. 2.5, the momentum distribution of  $np$  pairs is much more significant than one of the  $pp$  pairs at  $300 < k < 600 \text{ MeV}/c$ .

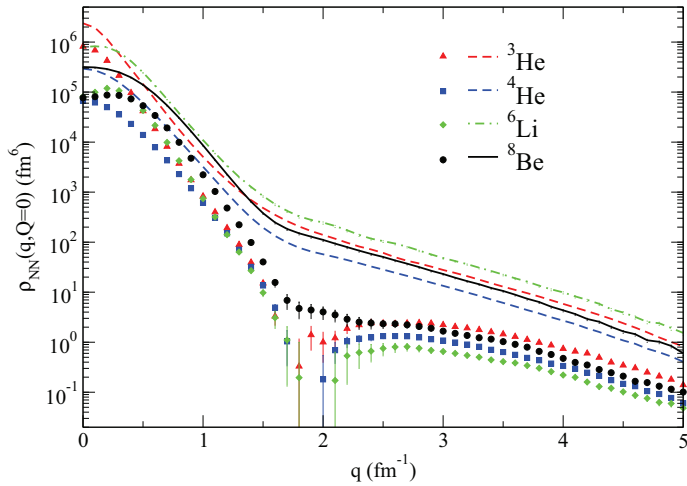


Figure 2.5: Isospin effect in momentum distribution, where lines represents the momentum distribution in  $np$  and dots represents the momentum distribution in  $pp$ . The dip in the  $pp$  momentum distribution around  $2 \text{ fm}^{-1}$  is due to the tensor correlations of protons [17, 22].

The isospin effect in 2N-SRC can be studied by triple-coincidence experiments, which not only measures the scattered electrons and the struck protons in a 2N-SRC configuration but also simultaneously detects protons and neutrons rejected in the opposite direction with equal momentum. Inclusive cross sections is also sensitive to such effect. One can examine the isospin-dependence by measuring the cross section ratio of two isotopes in the SRCs region, such as  $^{48}\text{Ca}/^{40}\text{Ca}$  [23] and  $^3\text{He}/^3\text{H}$  [24], which will be discussed in next section.

## 2.2 Probing SRCs using Electron-Nucleus Scattering

To isolate the high momentum nucleons and perform clean measurements of SRCs in nuclei, one needs to carefully select the proper kinematics settings to suppress other competing processes during scattering. By isolating the process of a high energy probe instantly removing a nucleon from SRCs, one is able to extract reliable information on the spectral function and momentum distribution from the measured observables. Meanwhile, it is essential to distinguish the struck and the spectator nucleons in the SRCs to understand the dynamical mechanism of generating SRCs in the nuclear ground state wave-function. As discussed in previous section, contributions from 2N-SRC and 3N-SRC in the spectral function can not be well separated by examining the recoil energy of the residual system. A specific reaction and a kinematic variable are required to study two processes separately.

A nucleus is a complicated system and the struck nucleon experiences different interactions both in its initial state and final state. The major problem in the experimental study of SRCs is the final state interaction (FSI) effects, where the information of the struck nucleon's momentum and energy can be largely distorted during the re-scattering processes with other spectators in the residual system. Fully understanding the role of FIS during the study of SRCs in electron-nucleon scattering from the nucleus is crucial.

### 2.2.1 Kinematics Conditions

Although there are different kinds of reactions for probing SRCs, there share the common kinematic conditions to provide a clean study. Overall, the desire to instantly remove the nucleon from the SRCs can be achieved by requiring sufficiently large energy and momentum transfer scales which significantly exceed the excitation scale

of the nucleus [18, 25]

$$\nu >> V_{NN}, \quad |\mathbf{q}| >> m_N/c, \quad (2.10)$$

where  $V_{NN}$  is the characteristic potential of the NN interaction and  $m_N$  is the nucleon mass. A reaction removing a nucleon from the nucleus under this condition allows the residual system to remain intact, where the spectral function will directly reflect the properties of SRCs [17].

The contribution of long range interactions, such as MECs, is suppressed by a factor of  $Q^{-4}$  with respect to the production of SRCs, and can be generally suppressed by requiring [26]:

$$Q^2 > 1.0 \text{ GeV}^2 >> m_{meson}^2. \quad (2.11)$$

In this condition, intermediate state resonances, such as the isobars current (IC), still have sizeable contributions. For example, for  $1 \text{ GeV}^2 < Q^2 < 4 \text{ GeV}^2$ ,  $\gamma N \rightarrow \Delta$  transition is comparable with  $\gamma N \rightarrow N$ . Those resonance states are generally within the region of  $0 < x_{bj} < 1$ , and their contributions can be suppressed by working at the region above the quasi-elastic scattering:

$$x_{bj} > 1. \quad (2.12)$$

Fig. 2.6 demonstrates that the combination of kinematic conditions (Eq (2.11) and Eq (2.12)) results in probing the nucleon from the 2N-SRC with the minimum momentum above the Fermi momentum ( $p_{min} > k_F$ ), where there is almost no contribution from the mean field part of the nucleon momentum distribution. When  $Q^2$  value is not sufficiently large ( $\sim 0.5 \text{ GeV}^2$ ), the 2N-SRC production is almost suppressed by other processes even at very higher  $x_{bj}$  ( $\sim 1.8$ ). At very high  $Q^2$  ( $\sim 10 \text{ GeV}^2$ ), the minimum momentum requirement of the struck nucleon easily achieves at relatively low  $x_{bj}$  ( $\sim 1.3$ ) due to the highly suppression of mean field effect.

Together with Eq (2.10), those kinematic conditions enable the clean measure-

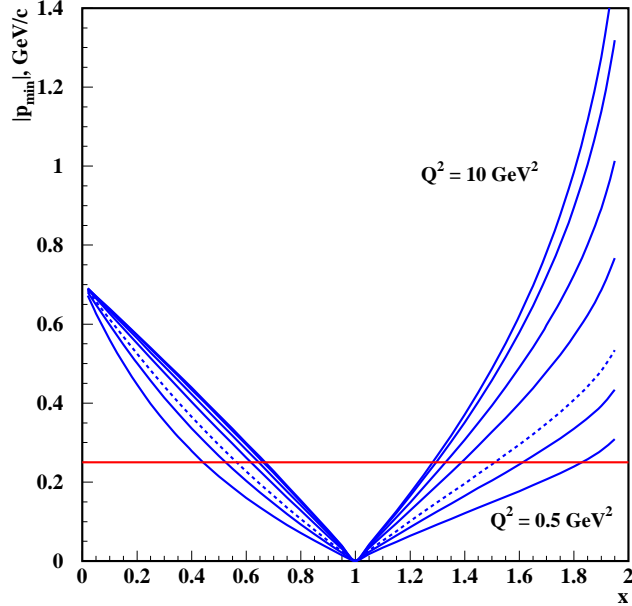


Figure 2.6: Minimum momentum of the struck nucleon as function of  $x_{bj}$  and  $Q^2$  for Deuterium, where the red line sets the value of the Fermi momentum ( $k_F$ ).

ment of high momentum nucleons from SRCs and meanwhile, largely eliminate the contribution from mean field effect, such as MECs and IC.

### 2.2.2 Inclusive Measurement

The inclusive cross section measurement of  $A(e, e')$  reaction in quasi-elastic region was first applied to isolate SRCs and currently is the only way to probe 3N-SRC. The cross section for  $x > 1.3$  and  $Q^2 > 1 \text{ GeV}^2$  is written as [27]:

$$\begin{aligned}
 \sigma_A(x_{bj}, Q^2) &= \sum_{j=2}^A \frac{A}{j} a_j(A) \sigma_j(x_{bj}, Q^2) \\
 &= \frac{A}{2} a_2(A) \sigma_2(x_{bj}, Q^2) + \frac{A}{3} a_3(A) \sigma_3(x_{bj}, Q^2) + \dots,
 \end{aligned} \tag{2.13}$$

where  $\sigma_j$  is the cross section for scattering from a  $j$ -nucleon correlation and  $a_j(A)$  denotes the probability of finding a nucleon in this correlation. First two terms

represents the contributions from 2N-SRC and 3N-SRC.

From Eq (2.1) and Eq (2.4), 2N-SRC (3N-SRC) predicts the scaling of the nucleon momentum distribution for heavy nucleus  $A$  with respect to the deuterium ( ${}^3He$ ). In the region of  $1.3 < x_{bj} < 2.0$  where 2N-SRC dominates,  $a_2(A)$  can also be given by the cross section ratio:

$$a_2(A) = \frac{2}{A} \frac{\sigma_A(x_{bj}, Q^2)}{\sigma_D(x_{bj}, Q^2)}, \quad (2.14)$$

where  $\sigma_D(x_{bj}, Q^2)$  is the cross section for scattering from the deuterium target.  $a_2(A)$  is identical to the one defined in Eq (2.1) and the formula indicates that at 2N-SRC region, the value of  $a_2$  is independent of  $x_{bj}$  and  $Q^2$ , but only relates to the nuclear number. The value of the ratio on the scaling plateau directly gives the relative number of 2N-SRC pairs in the nucleus.

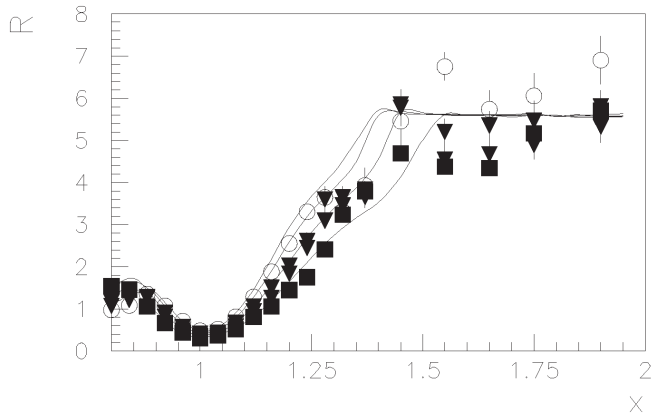


Figure 2.7: First evidence of 2N-SRC from SLAC [28]. Y-axis is the cross section ratio of  ${}^{56}Fe$  to  ${}^2H$  for  $Q^2 = 1.2 - 2.9 \text{ GeV}^2$  and x-axis is  $x_{bj}$ . The plateau of 2N-SRC clearly is clearly showed at  $x_{bj} > 1.5$  and agrees with the theoretical prediction based on the 2N-SRC model (lines).

Fig. 2.7 shows the experiment results from SLAC [28], which for the first time observed such a plateau using the cross section ratio of  ${}^{56}Fe$  to  ${}^2H$  at  $x_{bj} > 1.5$  and  $Q^2 = 1.2 - 2.9 \text{ GeV}^2$ . However, the statistic were limited and the deuterium data were taken at different kinematics, so the result was extracted with nontrivial

extrapolations. Recent Jefferson Lab results from Hall-B using Large Acceptance Spectrometer (CLAS) [29] and from E02-019 data in Hall-C [30] studied the values of  $a_2$  for various nuclei with higher statistics and with better resolution, and both results show sound agreement at the 2N-SRC region (Fig. 2.8 and Fig. 2.9).

Similarly, one can study 3N-SRC at  $2 < x_{bj} < 3$  with the cross section ratio of the heavy nucleus to  $^3He$ :

$$a_3(A) = K \cdot \frac{3}{A} \frac{\sigma_A(x_{bj}, Q^2)}{\sigma_{^3He}(x_{bj}, Q^2)}, \quad (2.15)$$

which is the same as the one in Eq (2.1) and denotes the number of  $^3He$ -like 3N-SRC configuration in the nucleus.  $K$  is a kinematic constant to correct difference of the electron-proton and electron-neutron cross sections:

$$K = \frac{\sigma_{ep} + \sigma_{en}}{Z\sigma_{ep} + (A - Z)\sigma_{en}}. \quad (2.16)$$

The CLAS data for the first time measured the kinematic region of 3N-SRC and observed the plateau raises at  $x_{bj} > 2.3$ . The E02-019 data, however, yields a different result in this region. From Fig. 2.9, the cross section ratio of  $^4He/^3He$  reaches the scaling region slightly later than the CLAS result ( $x_{bj} > 2.5$ ). And the scaling plateau can not be conformed due to the large error bars, mainly because of the large statistical subtraction to remove the contamination from target cells. A direct interpolation of the discrepancy is impossible since two experiments ran at very different  $Q^2$  range ( $Q^2 \sim 1.6 \text{ GeV}^2$  for CLAS and  $Q^2 \sim 2.7 \text{ GeV}^2$  for E02-019). It is not clear that both measurements were able to isolate the 3N-SRC contributions. The new experiment in Hall-A, E08-014, focuses on studying the scaling of 3N-SRC at  $x_{bj} > 2$  with much better accuracy, and the new preliminary results will be presented in this thesis.

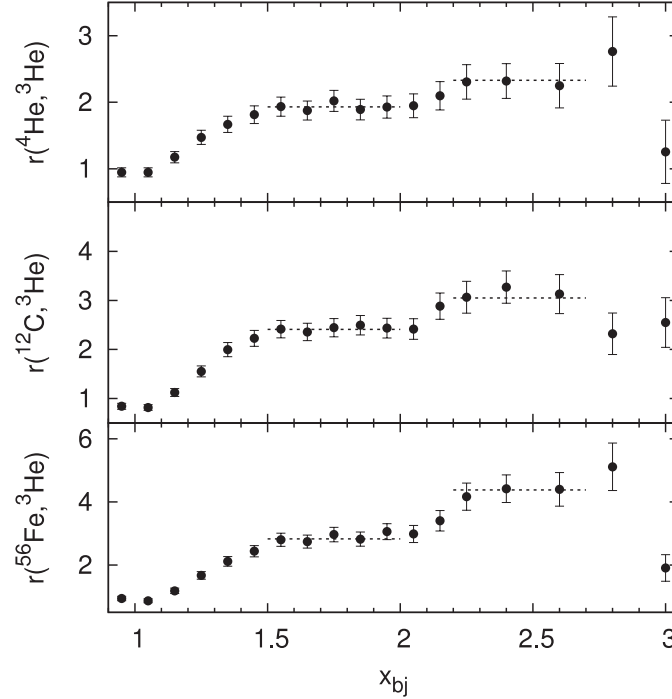


Figure 2.8: 2N-SRC and 3N-SRC results from Hall B [29]. The top, middle and bottom plots give the cross section ratios of  ${}^4He$ ,  ${}^{12}C$  and  ${}^{56}Fe$  to  ${}^3He$ , respectively. In each plot, both the 2N-SRC plateau (in  $1.5 < x_{bj} < 2$ ) and the 3N-SRC plateau (in  $x_{bj} > 2$ ) can be observed.

The other important study of SRCs in inclusive measurements is the difference of two scaling variables,  $x_{bj}$  and  $\alpha_i$ . From Eq (2.8), the LC variable  $\alpha_i$  is approximately equal to  $x_{bj}$  at large  $GeV^2$ . At low  $GeV^2$ , the approximation is not valid and the difference of the scaling behaviour in SRCs as a function of  $x_{bj}$  or  $\alpha_i$  is required to be carefully examined. Although  $\alpha_i$  can not be reconstructed in inclusive scattering, one can assume that in PWIA the virtual photon interacts with the nucleon in an 2N-SRC at rest. This assumption leads to a new expression of the LC variable specifically for 2N-SRC:

$$\alpha_{2N} = 2 - \frac{q_- + 2m}{2m} \frac{\sqrt{W^2 - 4m^2} + W}{W}, \quad (2.17)$$

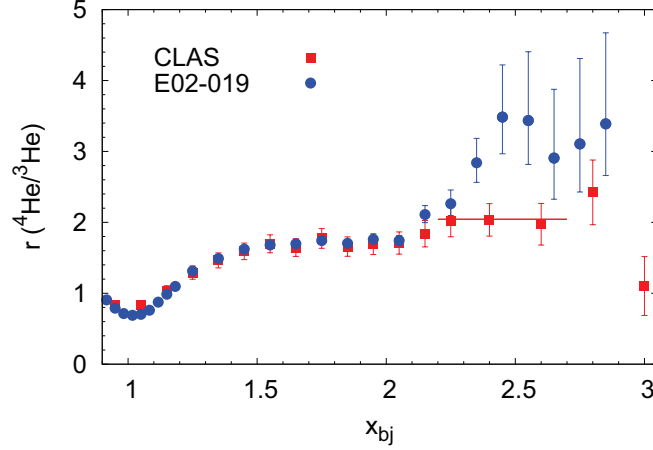


Figure 2.9: 2N-SRC and 3N-SRC results from E02-019 in Hall C [30] comparing with the result from Hall-B, where the blue dots are the E02-019 data and red dots are the CLAS data.

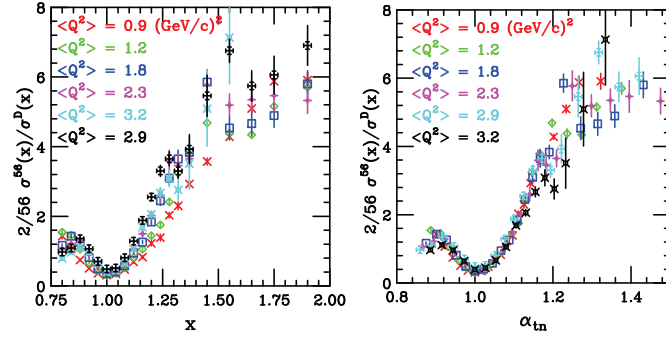


Figure 2.10: Ratio of  $^{56}\text{Fe}/2\text{H}$  as a function of  $x_{bj}$  (left) and  $\alpha_{2N}$  (right) for different  $Q^2$  values [28], which shows that the LC variable provides better scaling behaviour.

where  $q_-$  is the initial longitudinal momentum of the struck nucleon and  $W^2 = 4m_N^2 + 4m_N\nu - Q^2$ . The analysis of SLAC data [28] reveals that  $\alpha_{2N}$  can better isolate 2N-SRCs (Fig. 2.10) and allows one to examine the transition region from 2N-SRC to 3N-SRC. A more general expression for all  $\alpha_i$  in the inclusive measurement

can be obtained from [23]:

$$q_- \cdot \alpha_{jN} m_N + q_+ \cdot \left( M_A - \frac{M_r^2}{m_N(j - \alpha_{jN})} \right) = m_N^2, \quad (2.18)$$

where  $j = 2, 3, \dots$ ,  $q_+$  is the initial transverse momentum of the struck nucleon and  $M_r$  is the mass of the residual system. Taking  $j = 3$  can solve for  $\alpha_{3N}$  but the exact expression depends on the value of  $M_r$  since 3N-SRC has much more complicated configuration. As discussed in previous section, 3N-SRC-I is the dominant configuration in 3N-SRC where  $M_r = 2m_N$ , and give:

$$\alpha_{3N} = \frac{3}{2} + \frac{1}{2} [\sqrt{(3 + b_1)^2 - b_2} - b_1] \quad (2.19)$$

where,

$$b_1 = \frac{q_+ M_A}{q_- m_N} - \frac{m_N}{q_-}, \quad b_2 = 16 \frac{q_+}{q_-} \quad (2.20)$$

The value of  $M_r$  becomes higher for non-parallel configuration, such as 3N-SRC-II. Examining the scaling as a function of  $\alpha_{3N}$  and varying the value of  $M_r$  provides a sensitive probe to the detailed structure of 3N-SRC [23].

### 2.2.3 Semi-Inclusive Measurements

Proton-knock-out experiments allow the direct access of the proton's initial momentum distribution through the reconstruction of the nuclear spectral function from the exclusive cross sections. In addition to measuring the scattered electron, one can map out the effect of SRCs to the high momentum tail by detecting the struck proton. Since the correlated nucleon in 2N-SRC is ejected on the opposite direction is not detected, one generally treats the  $A(e, e'p)$  reaction as semi-inclusive process.

To evaluate the deviation of a theoretical calculation of the momentum distribution to the experimental cross section, a normalization factor is introduced in Eq (1.3)

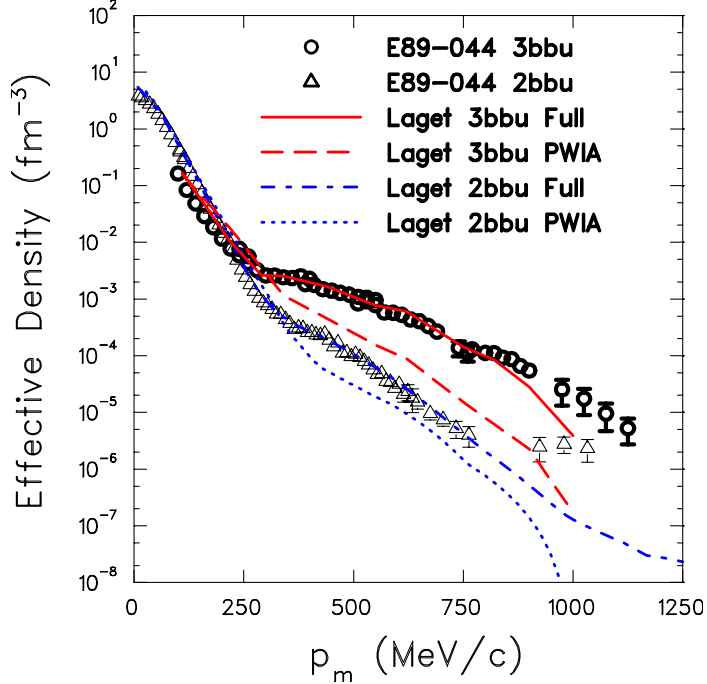


Figure 2.11: Proton Effective Momentum distribution in  ${}^3He$  [31], where circles and triangles are experimental data in  ${}^3He(e, e'p)pn$  three-body break-up and  ${}^3He(e, e'p)d$  two-body break-up, respectively. Lines are theoretical calculations from [32]. For the missing momentum above the Fermi momentum (250 MeV), the momentum distribution of three-body break-up is much stronger than the one of two-body break-up, indicating the dominance of SRCs in this region.

(for only one proton case) [33]:

$$\frac{d^6\sigma}{(dEd\Omega)_e(dEd\Omega)_p} = K\sigma_{ep}S(E_0, \mathbf{p}_0)T_A(Q^2), \quad (2.21)$$

where  $K$  is a kinematic factor and the transparency,  $T_A$  is the probability that a nucleon will be emitted from the nucleus with other effects, such as FSI. Experiments in Hall-C [34–36] measured the values of  $T_A$  for several nuclei which were found to be larger than the predictions in IPSM. Such an enhancement is mainly due to the SRCs effect [33].

Hall-A experiments [31, 37] studied the momentum distribution of  ${}^3He$  and observed that the strength greatly increases in the high momentum tail compared with the expected strength including SRCs (Fig. 2.11). This scenario is explained as the

combination of SRCs and FSI.

### 2.2.4 Triple-Coincidence Measurements

An triple-coincidence experiment,  $A(e, e' pN)$ , performs an exclusive cross section measurement which detects the scattered electron, the struck nucleon and the spectator nucleon in 2N-SRC. Such an experiment not only can directly conforms the production of 2N-SRC, but also can study the types of the nucleon pairs involved in the correlation. This experimental techniques has been proposed in the 1960's but only been carried out with the high luminosity and high energy electron beams [38–40].

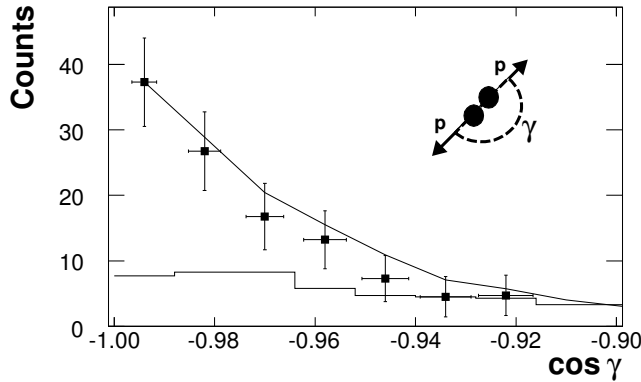


Figure 2.12: Angular correlation between nucleons in 2N-SRC, where the x-axis is the cosine of the opening angle between the struck nucleon and the spectator nucleon in the  $^{12}C(e, e' pp)$  reaction [39].

A recent experiment in Hall-A, E01-015, [39, 40], has performed such a measurement using electron scattering on carbon target. In the  $^{12}C(e, e' pp)$  reaction, the experiment studied the angular correlations between the struck proton and the spectator nucleons, and conformed that the correlated nucleons are back-to-back ejected from the nucleus (Fig. 2.12). The ratio of  $pn$  and  $pp$  in 2N-SRC can be extracted by using the measurement of  $^{12}C(e, e' pp)$  and  $^{12}C(e, e' pn)$ . Fig. 2.13 shows that the ratio of  $np/pp$  pairs is around  $18 \pm 5$ , which conforms that the 2N-SRC is dominated by the two-body tensor interaction.

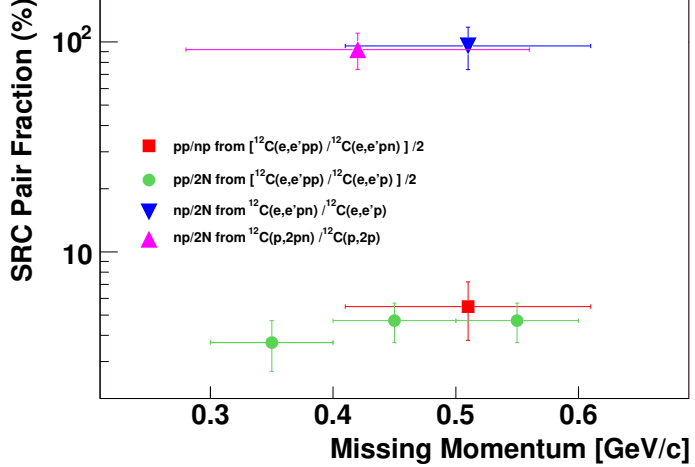


Figure 2.13: The fraction of  $np$  pairs to  $pp$  pairs in 2N-SRC in carbon from the triple-coincidence experiment in Hall-A [40].

### 2.2.5 Final State Interaction in SRCs

The effect of final state interaction (FSI) is proportional to  $1/Q^2$ . At low  $Q^2$  the contribution of FSI is large enough to break down the y-scaling feature of quasi-elastic scattering in PWIA [41]. The study of SRCs using inclusive cross section measurement requires sufficient  $Q^2$  values to eliminate the FSI contribution. The current results of inclusive data (i.e. in Fig. 2.10) indicate no dependence of  $Q^2$  for the scaling region of 2N-SRC, which proves that in the kinematic settings of SRCs study ( $Q^2 > 1 \text{ GeV}^2$ ) FSI has very small contributions.

The argument above is valid since the SRCs configurations are weakly interacting with other components in the nucleus and PWIA in the inclusive measurement is still applicable. However, the contribution of FSI within the SRC may not vanish even at very large  $Q^2$ . When the electron scattering on the nucleon in SRCs, the struck nucleon stays very close to other correlated nucleons and the probability of rescattering from the residual system is large. Despite the possible large contributions, FSI is localized in the SRCs and its contribution can be removed by taking the cross section ratio. For example, the FSI contribution in the 2N-SRC pairs in heavy nuclei

should be similar to one in  $^2H$ , and the ratio,  $\sigma_A/\sigma_{^2H}$ , should be able to cancel the FSI effect and only yields the clean contribution from 2N-SRC.

## 2.3 E08014 Experiment

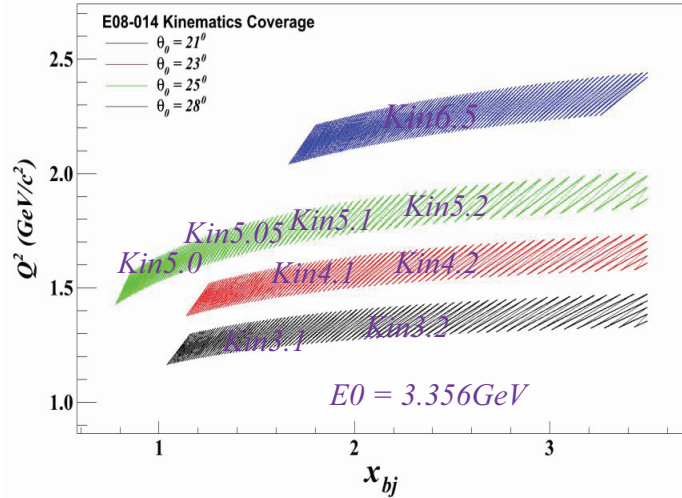


Figure 2.14: Kinematic Coverage of E08-014 experiment.

An new experiment, E08-014 [23], had been carried out in 2011 in Hall-A at Jefferson Lab, with electron beam energy of  $3.356\text{GeV}$  from the continuous electron beam accelerator facility (CEBAF). Utilizing the high resolution spectrometers in their standard configurations, as shown in Fig. 2.14, this experiment measured the inclusive cross section of  $^2H$ ,  $^3He$ ,  $^4He$ , and  $^{12}C$  at  $1.1 < Q^2 < 2.5(\text{GeV}/c)^2$ , which covers the range of  $x_{bj}$  from the quasi-elastic peak region to above 3.0. The absolute cross section results will be used to study the scaling function and momentum distribution at larger missing momentum, as well the effect of FSI. By taking the cross section ratio of heavy targets to  $^2H$  or  $^3He$ , one can examine the  $x_{bj}$  and  $Q^2$  dependence and SRCs, and measure the values of  $a_2$  and  $a_3$ . The relatively low  $Q^2$  setting allows the study of  $\alpha_{2N}$  and  $\alpha_{3N}$  in the scaling of SRCs. The Calcium isotopes,  $^{40}Ca$  and  $^{48}Ca$ , were also used to study the isospin dependence of 2N- and

3N-SRC. Detailed experiment setup and data analysis will be discussed in this thesis and preliminary results will also be presented.

# Chapter 3

## Experiment Setup

### 3.1 Overview

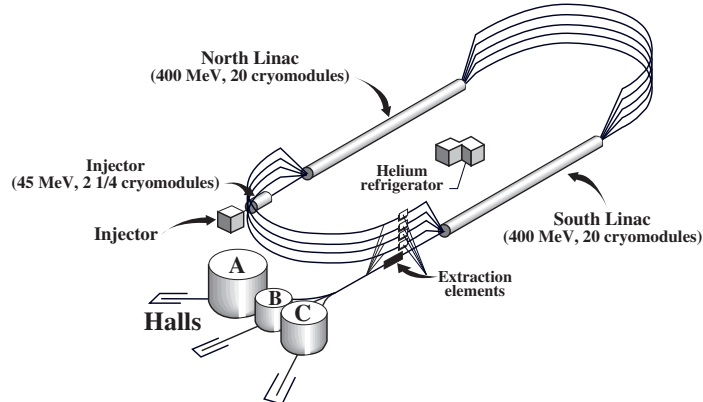


Figure 3.1: The Jefferson Lab Accelerator

Thomas Jefferson Lab (JLab) is a world's leading medium energy electron scattering laboratory, consisting of a continuous electron beam accelerator facility (CEBAF), three experimental halls (A, B and C), a free electron laser facility and several applied research centers (Fig. 3.1). An upgrade project has been proceeding to extend the beam energy from 6 GeV to 12 GeV, and a complete new experimental hall, Hall D, is currently under construction and expected to start taking data on late 2014.

CEBAF uses the radio frequency (RF) technique to deliver the polarized continuous-

wave (CW) electron beam simultaneously to all three experimental halls. An injector provides electrons with the polarization up to 85% and the maximum current of  $200 \mu A$ . The electron beam gains  $400 \sim 600$  MeV energy when passing through one of two super-conducting linear accelerators (linac), so the energy of the electron can be in the range of 0.8 GeV and 6.0 GeV within 5 maximum passes. Two arcs connect the linacs and provide  $180^\circ$  bending. The electron beam can be delivered into three halls simultaneously with different energy and current. During E08-014, the 3.356 GeV electron beam was delivered into Hall A with current up to  $150 \mu A$ . Polarization was not required.

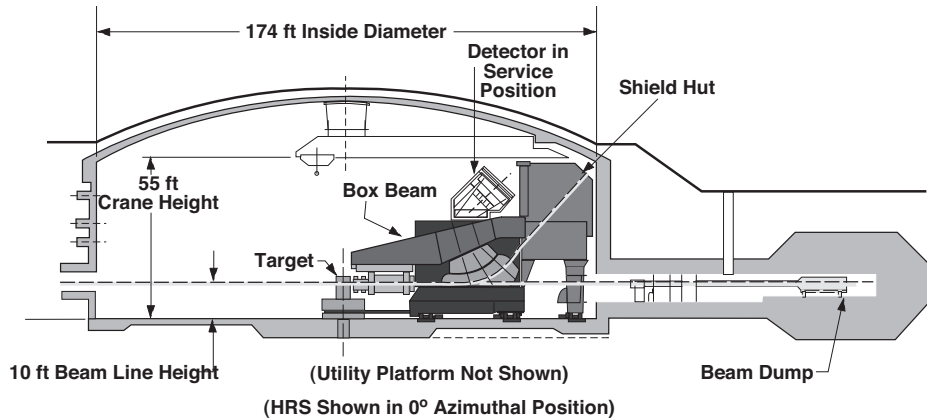


Figure 3.2: Side View of Hall-A

Hall-A is a circular bulk (Fig. 3.2) with a diameter of 53 m buried underground with concrete and earth. As shown in Fig. 3.3, the central elements in the hall include beamline components, a target system, and two identical high resolution spectrometers (HRSs). A detector package is stationed in a concrete hut which locates on top of each HRS near the Q3 exit and protects the instruments from radiation damage. The detector huts also store electronic modules to collect signal outputs from detectors and the beamline, generate triggers, and provide the front end of the CEBAF Online Data Acquisition system (CODA). A detailed discussion of the Hall-A instrumentation is presented in the reference [42].

View of Hall A Machines

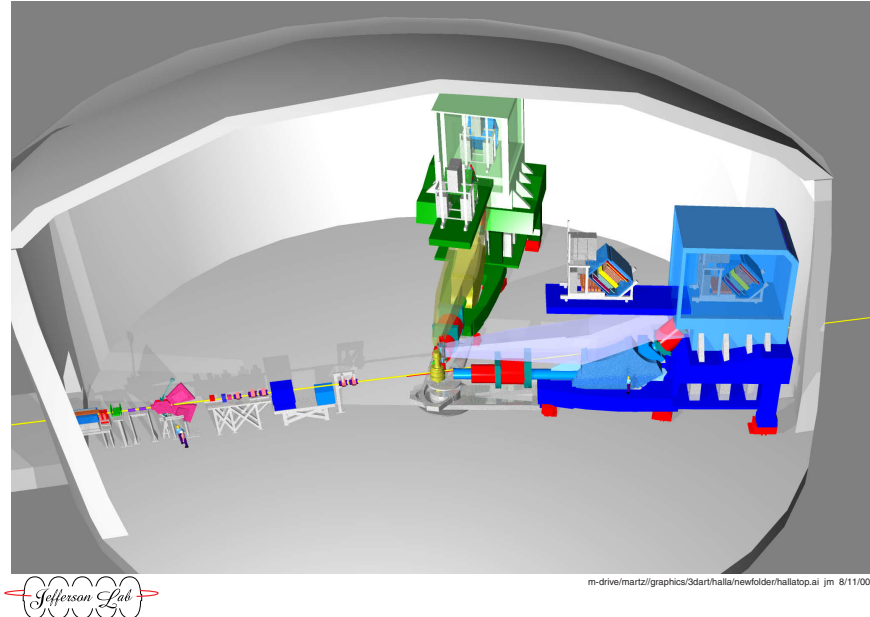


Figure 3.3: Top View of Hall-A

## 3.2 Beam

The electron beam is delivered into Hall-A through a stainless steel tube which is 10 ft above the hall floor and can hold a vacuum pressure  $\leq 10^{-6}$  Torr. The beam optics elements, including quadrupoles, sextupoles and corrector magnets, focus the beam on the target with spot sizes varying from 100 to 200  $\mu m$ . A faster raster system located at 23 cm upstream of the target position provides a larger beam spot of several mini-meters at the target. As shown in Fig. 3.4 [42], the beam running through the target is sent into the beam dump and spread out by a diffuser which consists of two 6.4 mm thick beryllium foils with water flowing between them. In addition, there are multiple beam diagnostics elements along the beamline to monitor, determine and control the relevant properties of the beam including the beam current, the electron energy and polarization, the beam position and direction, and the beam spot size at the target location.

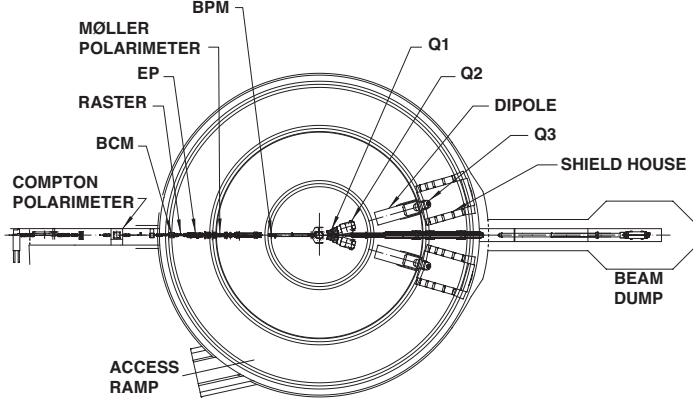


Figure 3.4: Schematic layout of beam instruments and spectrometers in HAll-A, including beamline components, beam diagnostic elements, and beam dump.

### 3.2.1 Beam Position Monitors

The beam position and direction at the target are measured by two beam position monitors (BPMs) located at 7.524 m and 1.286 m upstream of the target. Each BPM contains 4 antennas orientated in different directions inside the beam pipe. Each antenna picks up a voltage reading from the beam when the beam current is above 1  $\mu A$ , and the total four signals are used to calculate the beam position within 100  $\mu m$  of resolution. The BMPs have to be calibrated independently to obtain the absolute position of the beam. When taking the calibration data, two pre-surveyed super-harps adjacent to BMPs were used to determine the absolute beam position [43]. Event-by-event information from the BMPs are injected into the data stream, while the position average over every 0.3 s is also injected into the data stream every 3-4 s.

### 3.2.2 Beam Charge Monitors

The beam current monitor (BCM) is installed at 25 m upstream of the target location and provides a non-interfering measurement of beam current. It consists of an Unser monitor, two RF cavities, several electronic modules and an associated DAQ system [42]. Two cavities on either side of the Unser monitor are high frequency

wave-guides, the signal strength of which should be proportional to the value of beam current when they are tuned to the frequency of the beam. Before passing into RMS-to-DC converters [42], each BCM output signal is split into three copies, two of which are amplified by 3 times and 10 times, respectively. Hence there are totally six digital signals,  $U_1$ ,  $U_3$ ,  $U_{10}$ ,  $D_1$ ,  $D_3$  and  $D_{10}$ , each of which is further divided into two copies and fed separately into scalers in HRSs. To obtain total accumulated beam charge from scaler counts in one run, the BCM scalers have to be calibrated using BCM calibration data [44].

### 3.2.3 Beam Energy

The absolute energy of the beam can be determined by measuring the bend angle of the beam in the arc section of the beamline [45, 46]. The momentum of the beam is related to the field integral of the eight dipoles and the bend angle:

$$p = k \frac{\vec{B} \cdot \vec{dl}}{\theta}, \quad (3.1)$$

where  $k = 0.299792 \text{ GeV} \cdot \text{rad} \cdot T^{-1} m^{-1}/c$  and  $\theta$  is the bend angle. The magnetic field integral of the eight dipoles are measured with respect to a reference dipole, the 9th dipole. The value of the bend angle is measured with a set of wire scanners.

There is another method available to provide an secondary beam energy measurement [45, 46]. Utilizing a stand-alone device along the beamline located 17 m before the target, the eP method [42] measures the scattered electrons and protons in the  $^1H(e, e'p)$  elastic reaction, where the beam energy can be uniquely determined with known scattering angles. Both methods show good agreement within the uncertainties  $\leq 3^{-4}$ . The beam energy is monitored when taking the data and its value is stored into the data stream.

### 3.3 Target System

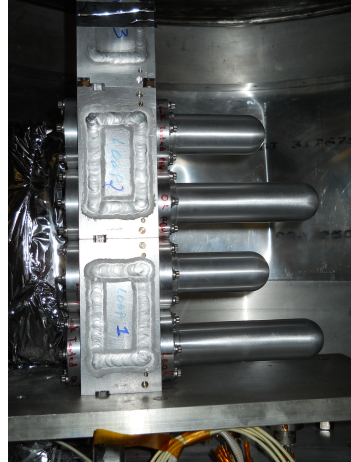
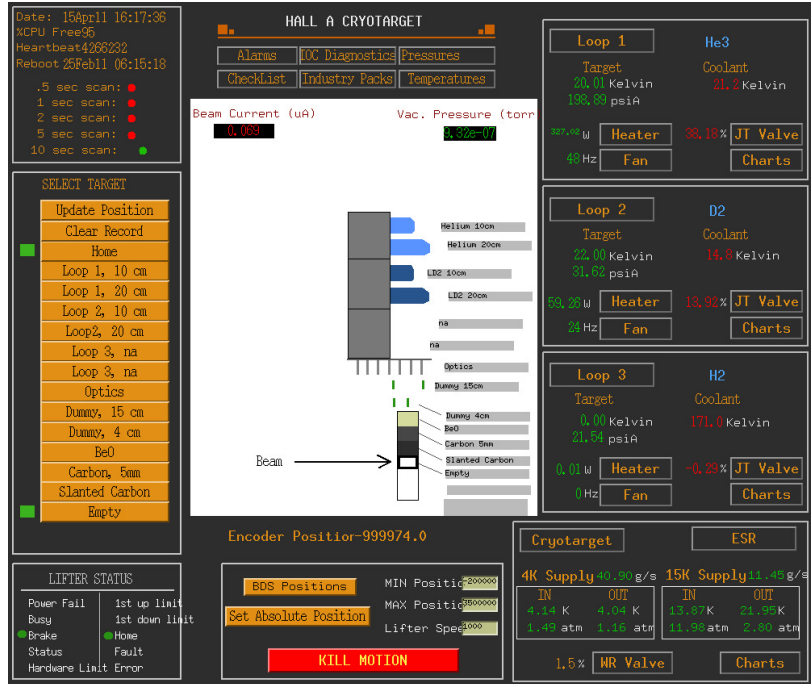


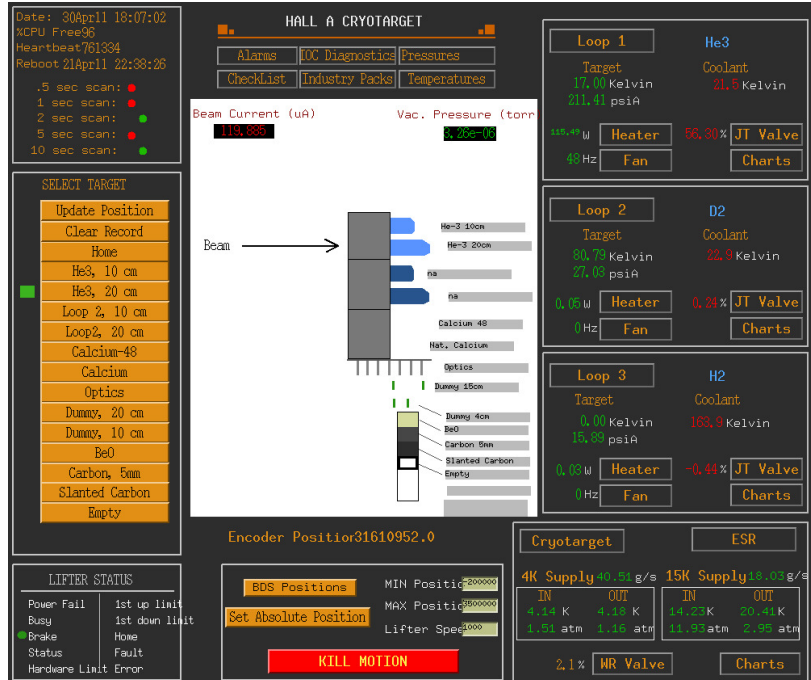
Figure 3.5: Picture of cryogenic target loops, where Loop-1 and Loop-2 include 10 cm and 20 cm aluminium cans, respectively. Loop-3 is not showed in this picture.

The targets are located in a scattering vacuum chamber, which is supported by a 607 mm diameter central pivot connected to two HRSs. The main element within the scattering chamber is a cryogenic target system, which includes three loops of cryogenic targets, a target ladder to support solid targets, sub-systems for cooling and gas handling, temperature and pressure monitors, and target control and motion systems [42]. Three target loops are called Loop-1, Loop-2 and Loop-3. Loop-1 and Loop-2 both contain two aluminium target cells with lengths of 10 cm and 20 cm, while Loop-3 has only a 20 cm cell (Fig. 3.5).

The cryogenic targets used in this experiment were the liquid deuterium ( $LD_2$ ), the gas  $^3He$  and the gas  $^4He$ . In the first run period of this experiment (from April 15th 2011 to April 19th 2011), the 20 cm cells of Loop-1 and Loop-2 were filled with  $^4He$  and  $LD_2$ , respectively.  $^4He$  was then replaced by  $^3He$  in the second run period (from April 21st 2011 to May 15th 2011), and  $LD_2$  was evacuated from Loop-2 (Fig. 3.6b). The 10 cm cell in Loop3 was used to store a  $^{48}Ca$  foil which could not be directly exposed to the air. The temperature of  $LD_2$ ,  $^3He$  and  $^4He$  were maintained at 22 K, 20 K and 20 K, respectively. The cooling power was provided by the ESR [47]



(a) First run period



(b) Second run period

Figure 3.6: Target control screen. Fig. B.5c is the targeted installed in the first run period from before April 19th 2011, while Fig. 3.6b is the targets installed in the second run period after April 20th 2011.

from the JLab cryogenic group.

Target	$\rho$ ( $g/cm^3$ )	Length (cm)	$\delta\rho$ ( $g/cm^2$ )	I ( $\mu A$ )	Comment
$LD_2$	0.1676	20.0		40	Loop2
Al can (Loop-2)	2.7	0.0272			Entrance
	2.7	0.0361			Exit
	2.7	0.0328			Wall
$^3He$	0.0296	20.0		120	Loop1
$^4He$	0.0324	20.0		90	Loop1
Al-can (Loop-1)	2.7	0.0272			Entrance
	2.7	0.0361			Exit
	2.7	0.0328			Wall
$^{12}C$	2.265	0.3937		120	
$^{40}C$	1.55	0.5735		40	
$^{48}C$	1.55	0.5284		40	
Dummy-20cm	2.7	0.1581		40	Upstream
	2.7	0.1589			Downstream
Dummy-10cm	2.7	0.1019		40	Upstream
	2.7	0.1000			Downstream

Table 3.1: Targets in E08-014 experiment, where BeO target and optics target are not listed.

Right below Loop-3 a 30 cm long optics target was installed for taking optics calibration data. The optics target contains 7 carbon foils located at -15 cm, -10 cm, -5 cm, 0 cm ,5 cm, 10 cm, and 15 cm, respectively. Two dummy targets, Dummy-20cm and Dummy-10cm, were installed below the optics target. to measure contributions from the end-cups of cryogenic target cells. Each of them contains two thick aluminium foils separated by 10 cm for Dummy-10cm and 20 cm for Dummy-20cm. There were four other targets, BeO,  $^{12}C$ ,  $^{40}Ca$  and an empty target, installed on the target ladder below Dummy-10cm.

The list of targets used in this experiment is given in Table 3.1 and a report that contains detailed information of targets and related systems can be found in [48]. The target positions must be surveyed during the experiment. However, survey reports were only available for experiments that ran before this experiment. The targets were reinstalled in the second run period but the extract position remained unknown

without a new survey. The relative positions with respect to the central foil of the optics target can be evaluated during the pointing study.

### 3.4 High Resolution Spectrometers

The essential equipments in Hall-A are two identical HRSs which provide high momentum resolution at the  $10^{-4}$  level over the range from 0.8 to 4.0  $GeV/c$ , high position and angular resolution in the scattering plane, and large angular acceptance. As shown in Fig. 3.4, the spectrometer on the left of the beam direction (to the beam dump) is called HRS-L, and the other one on the right is called HRS-R. The basic layout of a HRS is given in Fig. 3.7, where the magnet configuration of each HRS is QQQDQ, including three superconducting quadrupoles and a dipole [42]. Two quadrupoles, Q1 and Q2, are installed in front of the dipole to achieve the desired angular acceptance and maximize the resolving power for the bend angle. The dipole performs a  $45^\circ$  vertical bending of charged particles, and additionally, accommodates the extended targets and focuses the parallel beam. The third quadrupole, Q3, is behind the dipole to enhance the position and angular resolutions. Some important characteristics of HRSs are listed in Table 3.2.

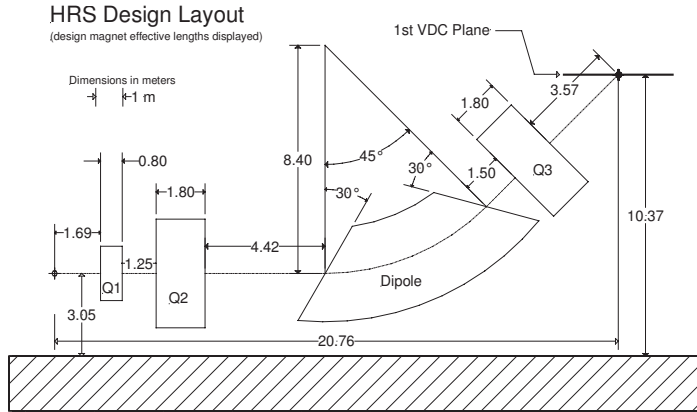


Figure 3.7: Schematic layout of HRS, which shows the sizes and locations of the dipole and three quadrupole [42].

---

Bend Angle:	$45^\circ$
Optical Length:	23.4 m
Momentum Range:	0.3-4.0 GeV/c
Momentum Acceptance:	$-4.5\% < \delta p/p < +4.5\%$
Momentum Resolution:	$1 \times 10^{-4}$
Angular Range	$12.5 - 150^\circ$ (HRS-L), $12.5 - 130^\circ$ (HRS-R)
Angular Acceptance:	$\pm 30$ mrad (Horizontal), $\pm 60$ mrad (Vertical)
Angular Resolution:	0.5 mrad (Horizontal), 1.0 mrad (Vertical)
Solid Angle:	6 msr at $\delta p/p = 0, y_0 = 0$
Transverse Length Acceptance:	$\pm 5$ cm
Transverse Position Resolution:	1 mm

---

Table 3.2: Design characteristics of HRSs, where the resolution values are for the FWHM [42].

The power supply for the Q3 on HRS-R (RQ3) was not working properly during the experiment and limited the maximum central momentum setting to 2.876 GeV/c, but the experiment was planned to reach the maximum central momentum to 3.055 GeV/c. The RQ3 field was scaled down to 87.72% of its normal value in each setting, which allowed only one optics matrix for all data on HRS-R. Accordingly, a new optics matrix was desired to match the new magnetic setting. An optics calibration procedure will be discussed in next chapter.

### 3.5 Detector Packages

As shown in Fig. 3.8, the detector package in each arm includes two vertical drift chambers (VDCs), two scintillator planes (S1 and S2m), a gas Cherenkov detector (GC), and a calorimeter. In addition to these standard detectors, a long single-bar scintillator (S0) and an Aerogel Cherenkov detector (AC) are included in each HRS, and a focal plane polarimeter (FPP) is available in HRS-L. S0, AC and FPP were not used during this experiment.

Particles coming through the HRS are fully characterized by the detector package and their signal outputs are delivered to the front-end electronics to form trigger signals and to be recorded by the data acquisition (DAQ) system.

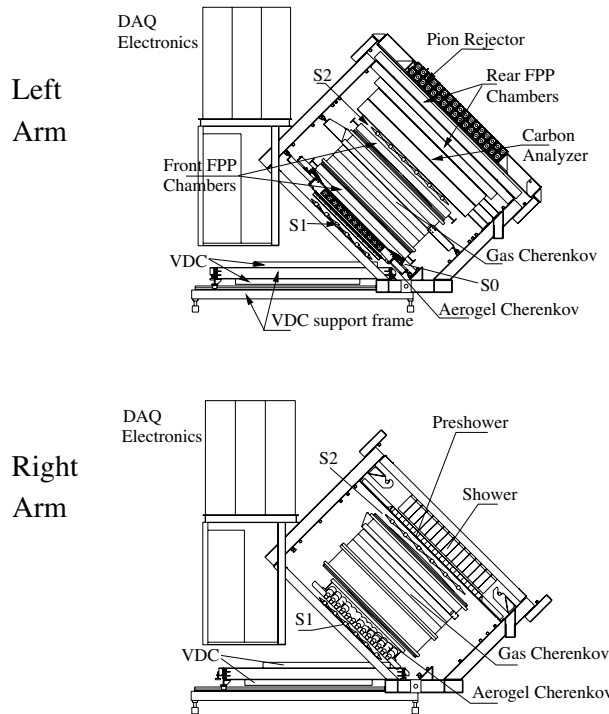


Figure 3.8: HRS Detector Stack, where all detectors available for different experiments are shown. However, only VDCs, S1, S2m, Gas Cherenkov detectors and Calorimeters were installed in E08-014.

Signals from VDCs are converted into digital types by the discriminator cards attached on the VDCs and then sent directly into the front-end of the time-to-digital converters (TDC) on the FastBus crate. For all other detectors, each analog signal from the corresponding photomultiplier tube (PMT) is split into two copies, one of which is properly delayed through a long cable before it is fed into the front-end of an analog-to-digital converter (ADC), and the other one of which, at the same time, goes through the discriminator module (DIS). If the amplitude of the analog signal is over the threshold value, a digital signal will be created and further used to form trigger signals or be recorded by the TDC front-end.

The design and performance of each detector will be discussed in the following.

### 3.5.1 Vertical Drift Chambers

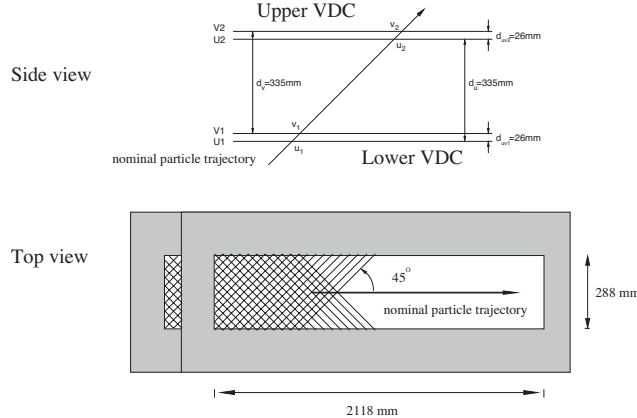


Figure 3.9: Layout of VDCs. The particle comes with a  $45^0$  from the lower chamber to the upper chamber. Each VDC is composed of two wire planes (U and V), and each plane contains 368 wires, which are oriented at  $90^0$  for one another. Two gold-plated Mylar planes below and above each wire plane are not shown here.

The trajectory of particles after the Q3 exit is tracked by two identical VDCs, which are placed vertically 335 mm apart and inclined by  $45^0$  along the normal particle trajectory [42], as shown in Fig. 3.9. There are two wire planes (U and V) in each VDC, and each plane contains 368 wires which are oriented at  $90^0$  for one another. Two gold-plated Mylar planes are placed below and above each wire plane, and a high electric field is generated by applying the high voltage with  $-4\text{ kV}$  between the wire plane and each Mylar plane. Both VDCs are filled with argon (68%) and ethane (38%) with a flow rate of 10 *liter/hr*.

When a particle goes through the VDC, the gas molecules are ionized and create a bunch of electrons and ions on the trajectory of the particle. The electrons are accelerated by the high field toward the closest wires, and the signal collected by each wire is amplified and read out by a pre-amplifier TDC card. On average, five sense wires have read-out signals when a particle passes through each wire plane. The exact location where the particle hits on the plane can be reconstructed by those TDC

signals. Four locations provided by the four wire planes are used to fit the trajectory of the particle. The position resolution in the focal plane is about  $100 \mu\text{m}$  and the angle resolution is near 100 mrad.

### 3.5.2 Scintillator Counters

Two scintillator planes, S1 and S2m, are placed after VDCs and separated by 2 m apart. S1 is composed of six overlapping thin plastic paddles, and S2m has 16 smaller paddles. When a charge particle passes through the paddle, it creates light which travels toward both ends of the paddle. A PMT attached to each end of the paddle collects the light and converts it into an analog signal. Scintillators have very fast time-response with very good resolution ( $\sim 30$  ns), so their signals are the major sources to generate triggers for the DAQ system. The traditional production trigger in Hall-A is generated by requiring both S1 and S2m to be fired within a narrow time windows. A detailed discussion of trigger system is given in Section 3.7 and Appendix A.

### 3.5.3 Gas Cherenkov Detectors

A high energy charged particle radiates Cherenkov light when it travels in a medium with its velocity faster than the speed of light. The basic mechanism of Cherenkov radiation is that atoms along the track of the particle are polarized and become dipoles, and the variation of dipole moments emits electromagnetic light [49].

The angle between the direction of Cherenkov light and the track of the charge particle is given by:

$$\cos\theta = \frac{1}{\beta n}, \quad (3.2)$$

where  $n$  is the index of reflection of the medium, and  $\beta = v/c$ . The velocity-dependence property of Cherenkov radiation provides an effective tool to discriminate

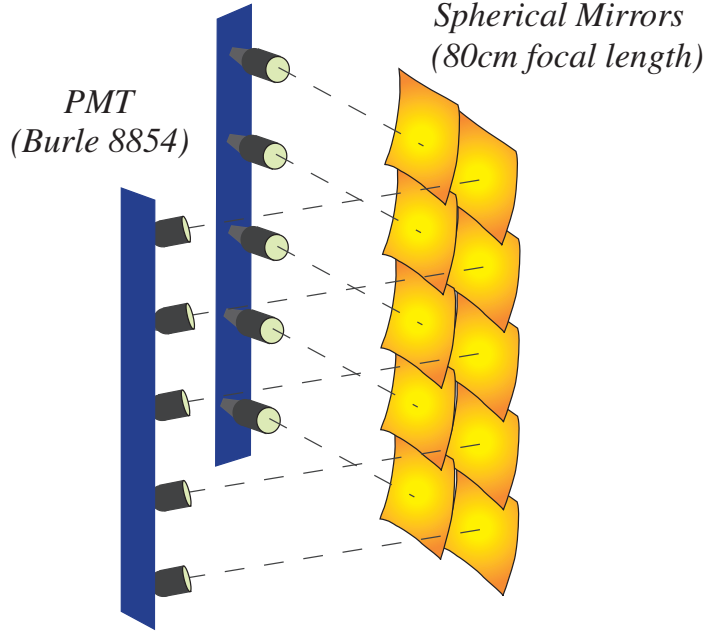


Figure 3.10: Design of Cerenkov Detector. Ten spherical mirrors were carefully arranged to collect the Cherenkov light and focus it into their corresponding PMTs.

particles with different masses, since the momentum threshold to emit Cherenkov light depends on the mass of the particle:

$$P_{threshold} = \frac{mc}{\sqrt{n^2 - 1}} \quad (3.3)$$

A gas Cherenkov detector (GC), made up of a steel box with thin entry and exit window, is mounted between S1 and S2m on each HRS. Within the box ten light-weight spherical mirrors with very small thickness ( $0.23 \text{ g} \cdot \text{cm}^{-2}$ ) are positioned in a  $2 \text{ (horizontal)} \times 5 \text{ (vertical)}$  array, as shown in Fig. 3.10. These mirrors are carefully arranged to efficiently reflect and focus the Cherenkov light on the associated ten PMTs.

The GC box is filled with atmospheric pressure  $CO_2$ , which gives the index of refraction to be 1.00041. The momentum threshold for electrons to radiate Cherenkov light in this detector is about 18 MeV/c, while the threshold for pions is as high as 4.9 GeV/c. Since the momentum coverage of HRS is from 0.5 GeV/c to 4.0 GeV/c,

only electrons can emit Cherenkov light in the detectors. Pions may still be able to produce signals in the GC when they interact the gas and create low-energy electrons (i.e.,  $\delta$ -electrons). However, the probability of such process is relatively low and the amplitude of the signal is comparable to the background signal. The path length of the GC on HRS-L is 80 cm which yields an average of 7 photon-electrons, while on HRS-R, the path length for the GC is 130 cm, leading to 12 photon-electron on average [42]. The design of GCs provides excellent electron identification (99%).

The signal from each PMT is amplified 10 times by an amplifier and divided into two copies. One copy is directly sent to the front-end ADC for offline analysis. The other copy is further split into two pieces, one of which is converted into a digital signal and sent to the TDC, while the other of which is added together with the similar signals from other 9 PMTs. The sum of the ten signals is then converted into a digital signal which is used for the design of online triggers, such as the efficiency triggers. During E08-014, GCs were also included in the production triggers to suppress pion events during the data recording.

### 3.5.4 Lead Glass Calorimeters

In each HRS, a calorimeter is placed behind S2m for the energy measurement of charge particles. Each calorimeter is composed of two layers of lead glass blocks and associated PMTs (Fig. 3.11). The gaps between blocks in the first layer is covered by the blocks in the second layer. The two layers of the calorimeter in HRS-L are called Pion-Rejector-1 (PRL1) and Pion-Rejector-2 (PRL2), respectively, and each layer consists of two columns of 17 lead glass blocks. In HRS-R, the first layer of the calorimeter, also named as PreShower (PS), is formed by two column of 24 lead glass blocks, while the second layer, called Shower (SH), includes two columns of 16 lead glass blocks.

When propagating through the dense material, a high energy charged particle loses

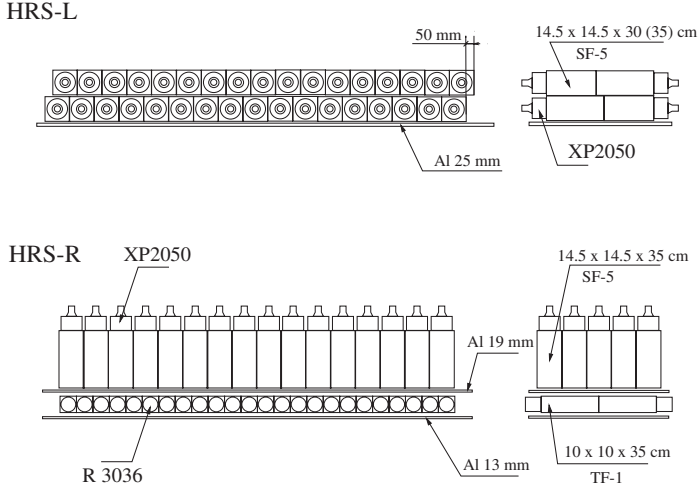


Figure 3.11: Schematic layout of Calorimeters in HRS-L and HRS-R. The calorimeter on HRS-L contains two overlapped layers, Pion-Rejector-1 and Pion-Rejector-2, and the calorimeter on HRS-R is also composed of two layers, Pre-Shower and Shower.

its energy exclusively through the Bremsstrahlung radiation. The emitted photons sequentially create electron-positron pairs which generate secondary Bremsstrahlung radiation. Along the long path length in the material, an electromagnetic cascade is developed along the direction of incident particle. At the GeV energy scale, only electrons are able to develop such a cascade in the HRS calorimeter. Since heavier particles require a much longer path length, the calorimeter provides a useful substantial particle identification in addition to the GC. PS and SH together form a total absorber since they use much thicker lead glass blocks which can absorb the entire electromagnetic shower produced by the incident electrons. PRL1 and PRL2, even though they don't form a total absorber, still provide powerful capability of electron identification.

## 3.6 Data Acquisition System

The data-acquisition (DAQ) system in Hall-A is composed of the CEBAF online data acquisition system (CODA) developed by the JLab CODA group, and the associated

hardware components. CODA is a tool-kit of software components, including read-out controllers (ROCs), the event builder (EB), the event recorder (ER) and the event-transfer (ET). The other major component is the RunControl (RC) which is a graphical user interface to choose experimental configurations, to start and stop runs, and to monitor and reset CODA components [42]. The hardware elements are basically composed of front-end Fastbus crates, VME devices (ADCs, TDCs and scalers), VME-Fastbus interfaces, single-board VME computers, trigger supervisors (TS) and network components. CODA is operated on a Linux based workstation which stores the recorded data (called raw data) in the local hard-drive. The data is subsequently transferred to a mass storage tape silo (MSS) for long term storage. Data in the local hard-drive will be deleted when the hard-drive runs out of space.

E08-014 ran consecutively with four other experiments during the spring of 2011. Besides the HRSs, the BigBite spectrometer and a neutron detector were installed in the hall for double-coincidence and triple-coincidence experiments. Triggers from four devices were sent to the same TS located in the electronic hut on the floor. When a trigger was accepted by the TS, a Level-One-Accept (L1A) signal was generated and sent back to each spectrometer. The leading-edge of the L1A signal was then adjusted by the strobe signal in a retiming-module (RT) installed in the local front-end crate. The signal from RT was fed to the Transition Module (TM) [50], where an ADC gate, a TDC Start/Stop signal and control signals were generated and distributed to the front-end electronics on Fastbus crates and VME crates where ADCs, TDCs and scalers start to record data when these signals arrive. An event number associated with this trigger was registered in the DAQ system and all signals associated with this events were recorded.

Limited by the dead-time and data size, not all triggers were accepted by the TS. A pre-scale factor was assigned to each trigger type to control the total event rate before CODA starts taking data. For example, a pre-scale factor "3" represents only

the first one is accepted for every three consecutive events from the trigger, and a pre-scale factor "0" means that no event from the trigger will be recorded. Each time when CODA starts to take data, an unique run number is given to the raw data file which stores all events coming after the start of the run. To control the total size of the data file and to prevent the data file from being damaged by any errors during the data taking, CODA will be stopped when each run reaches a pre-defined length of time or a certain number of events, and then a new run will be started with a new run number.

Scaler events are read every 1-4 seconds and stored in the data stream. Meanwhile, data from the Experimental Physics and Industrial Control System (EPICS), such as the beam energy, the BPM and BCM readings, the temperature and pressure of the target system, the angles and magnet fields spectrometers, etc., are also inserted into the data stream for every few seconds.

### 3.7 Trigger Design

During E08-014 the scattered electrons were measured by both HRSs simultaneously. The BigBite and the neutron detector were turned off and their triggers were ignored. Both HRSs share the similar design of the trigger system which is illustrated in Fig. 3.12. Three detector planes, S1, S2m and GC were included in the trigger design. A logic signal was created when one or more scintillator bar in S1 or S2m was fired. The logic signal of the GC was the digital signal converted from the sum of ten PMT signals. The coincidence of logic signals from S1, S2m and GC creates T1 (T3) trigger in HRS-R (HRS-L), which is the production trigger in this experiment. T2 (T4) was formed in HRS-R (HRS-L) by the coincident signal of the GC logic signal and only one of the S1 or S2m logic signal. T2 (T4) was designed to evaluate the trigger efficiency of T1 (T3). For some other experiments, T3 and T4 were designed

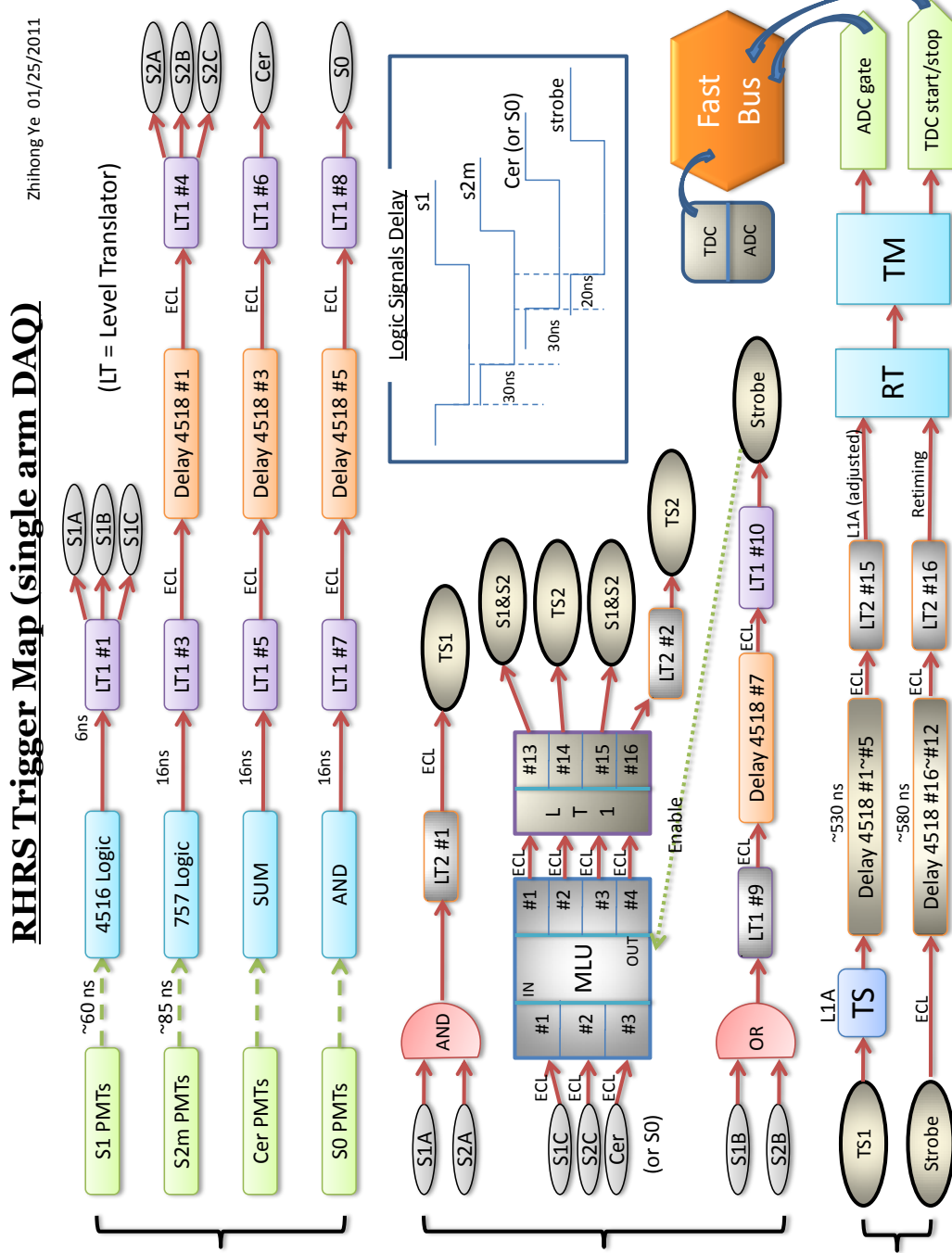


Figure 3.12: Single arm trigger design on HRS-R. The HRS-L trigger has the similar layout except some electronic modules were different.

by replacing the GC with S0. T6 (T7) is generated from the overlapped signal of S1 and S2m, and is the traditional HRS main trigger. Events from T6 and T7 were used for particle identification study since pions were also recorded. T5 is the coincident signal of T1 and T3, and was disabled in this experiment. A discussion of triggers during the data analysis is given in Appendix A.

# Chapter 4

## Calibration

### 4.1 Overview

Experimental raw data collected by the DAQ system is stored in individual data files. Each file is associated with an unique run number and hence is also called "a run". The raw data contains plentiful information of each event, including the experimental settings during the run and all the signal readouts from experimental instruments. However, those information can not be directly read out for offline analysis. The Hall A C++ Analyzer [51], an object-oriented framework on top of ROOT [52] and developed by the Hall A software group, is used to replay the raw data, extract and calculate importance quantities, and store these quantities in ROOT files which can then be directly accessed through the ROOT interface or C/C++ subroutines. Each ROOT file contains several subdirectories which are called "trees". The event-by-event detector readouts, including both the uncalibrated and calibrated signals are stored in the **T** tree. The EPCS readings are put in the **E** tree, and the **RIGHT** tree and **LEFT** tree store signal readouts from scalers in HRS-R and HRS-L, respectively.

During the data replay, each quantity must be correctly linked to the corresponding readout-signal with an up-to-date map which contains the front-end crate number,

the model of the electronic module and the slot ID in the FastBus crate, and the channel number which the signal cable connects to. Such a map is given in an individual file associated with the instrument. The Analyzer's data base (DB) stores these files for all Hall-A instruments. The parameters to convert the raw signals into calibrated quantities are also stored in the DB.

The first step of the data analysis is to calibrate the parameters for each instrument using calibration data, which will be discussed in this chapter. After these parameters are updated, the raw data will be replayed again and the new ROOT files can be used to extract useful physics quantities, for example, extracting cross sections, given in next chapter.

In this experiment, the calibration is composed of three major parts: beam instruments, detector packages and optic matrices of HRSs.

The calibration of beam instruments aims to obtain the parameters of the beam position monitors (BPMs) and the raster system which determine the event-by event beam position, and calibrate the beam charge monitors (BCMs) for the accumulated beam charge. The beam position calibration has been proceeded during the experiment by using the Harp scan data [53]. The detailed calibration procedure of the BPMs and the raster system can be found in the reference [43]. The result of BCM calibration is given in this report [44], and the calculation of beam charge will be presented in Section 5.2.

Each detector in the HRS can be individually calibrated, while the calibration of HRS optics requires a good determination of the beam position and an updated reference time ( $T_0$ ) for each VDC wire.  $T_0$  can be changed each time when the parameters of the TDC signals from S1 and S2m are updated. In this experiment, S1 and S2m was unable to be calibrated because of several bad TDC channels, and the values of  $T_0$  were calculated with old S1 and S2m parameters. The detailed calibration of the gas Cherenkov detectors, calorimeters and the HRS optics will be given in next

two sections.

## 4.2 Detector Calibration

The gas Cherenkov detector (GC) in each HRS contains 10 PMTs. The calorimeter in HRS-L contains two layers, Pion-Rejector-1 (PRL1) and Pion-Rejector-2 (PRL2), each of which has 34 PMTs. The calorimeter in HRS-R has 48 and 32 PMTs in Pre-Shower (PS) and Shower (SH), respectively. These PMTs collect the signals created by an particle passing through the detectors. The read-out signal from each PMT is split into two copies which are then recorded in the TDC and the ADC front-ends, respectively.

For the common-stop TDC module, the channel number in the TDC spectrum represents the time difference between when the event triggers and when the STOP signal arrives. The channel number in the ADC spectrum, on the other hand, is directly related to the strength of the PMT signal. However, the PMT signal not only is proportional to the photon energy, but also depends on the high voltage applied on the PMT as well as the amplitude of the background signal. Hence when collecting the signal with the same strength, different PMTs in the same detector may give different channel numbers in their ADC spectra. In the DB, each detector associates with a group of parameters, or called gain factors, which can convert the channel number of each ADC spectrum into a common unit. These gain factors have to be calibrated each time when the detector configuration is modified during the experiment or for different experiments. After updating the gain factors in the DB and performing the new data replay, the calibrated ADC spectra can be added up together to obtain the total signal released by the particle in the detector.

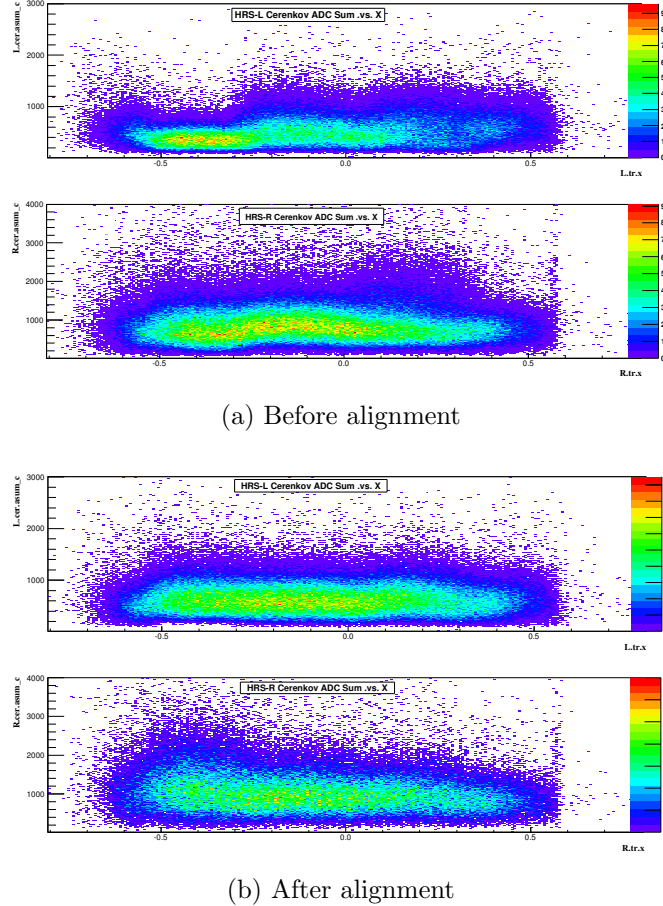


Figure 4.1: Alignment of gas Cherenkov detectors. Each 2-D histogram give the distribution of the sum of the GC ADC spectra along the detector plane. Plots in (a), top for HRS-L and bottom for HRS-R, show that the ADC peaks are off by certain channels before the calibration. Plots in (b) demonstrate that those peaks are nearly at the same channel number after the alignment.

#### 4.2.1 Gas Cherenkov Detectors

The energy of a single photon which causes the emission of the single photo-electron (SPE) is only determined by the photocathode material of the PMT. If the PMTs in the detector are from the same model, the SPE peaks in their ADC spectra should denote the same photon energy. A calibration procedure of the GC aims to align the single photon electron (SPE) peak in each ADC spectrum to 100 channels. The gain

factor for the *i*th PMT are defined as:

$$C_i = \frac{100}{M_i^{SPE} - M_i^{ped}} \quad (4.1)$$

where  $M_i^{SPE}$  and  $M_i^{ped}$  are the mean values of the SPE peak and the pedestal peak in the *i*th ADC spectrum.

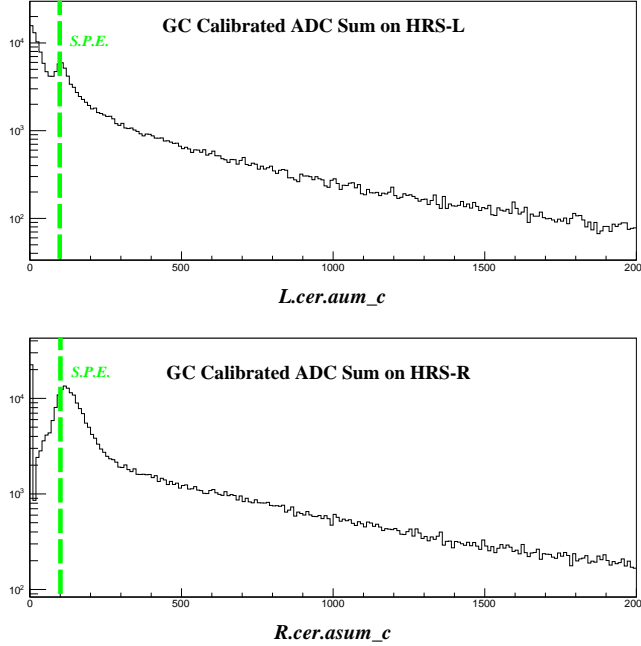


Figure 4.2: Single photon electron peaks (SPE) in the sum of the GC ADC spectra. Top for HRS-L and Bottom for HRS-R. The green lines indicate that the SPE peaks have been properly aligned at 100 ADC channels on each GC.

The ADC spectra don't show SPE peaks when plotting events from the main production triggers (T1 for HRS-R and T3 for HRS-L). These triggers include the GCs of which the thresholds have excluded most of weak signals including SPEs. The calibration was performed using events from the T6 trigger for HRS-R and the T7 trigger for HRS-L which don't include the GCs. The raw ADC spectrum of each PMT was plotted and the channel numbers of the pedestal peak and the SPE peak were identified and recorded. The gain factors for all ten PMTs in the GC were calculated

with Eq. (4.1) and their values were updated in the DB. The new data replay used these new parameter to calculate the calibrated ADC spectra which should have the same energy scale to each ADC channel.

Fig. 4.1 shows that the calibrated ADC spectra were well aligned. The sum of ten calibrated ADC spectra clearly shows the SPE peak located at 100 channel (Fig. 4.2), and can be directly applied on the particle identification.

### 4.2.2 Electromagnetic Calorimeters

The Hall-A calorimeters, composed of two layers of lead glass blocks for each, are able to measure the energy of few GeV electrons deposited exclusively in the detectors. The performance of energy measurement is limited by the design of calorimeters, as well as the energy range and the type of charge particles. In general, the energy resolution of a calorimeter can be represented by [49]:

$$\frac{\sigma(E)}{E} = a \oplus \frac{b}{\sqrt{E}}, \quad (4.2)$$

where  $\oplus$  represents two terms added in quadrature. The first term is mainly contributed by systematic errors, such as intrinsic shower fluctuations, which should be small for homogeneous calorimeters, such as total absorbers. The value of second term is determined by the uniformity of calorimeters as well as uncertainty of detector calibration. It is typically  $5\%/\sqrt{E}$  for lead glass calorimeters.

The electron creates a track during the cascade and the lead glass blocks along the track collect these photon signals. During the data replay, these blocks can be identified by using the VDC tracking information, and in the same layer the group of these blocks is called a cluster. The sum of their ADC spectra after the calibration denotes the energy deposited in this cluster, and should be distinguished from the sum of the calibrated ADC spectra of all blocks in this layer, although they are equal

when all energy are completely deposited in the cluster and the background signals are small.

Once the individual ADC spectrum is calibrated, the sum of the energy deposited in both layer should be equal to the energy (or equivalently the momentum) of scattered electrons. A new variable,  $E/P$ , is defined as the ratio of the energy sum of two clusters to the electron's momentum, and should be centered at one if the gain factors are properly calibrated. Different procedures were applied on each calorimeter.

A minimization method was used to calibrate the calorimeter on HRS-R, the two layers of which are called Pre-Shower (PS) and Shower (SH) [54]. The Chi-Square is defined as:

$$\chi^2 = \sum_{i=1}^N \left[ \sum_{j \in M_{ps}^i} C_j \cdot (ADC_j^i - Ped_j) + \sum_{k \in M_{sh}^i} C_k \cdot (ADC_k^i - Ped_k) - P_{kin}^i \right]^2, \quad (4.3)$$

where  $i$  is the  $i$ th event;  $j$  is the  $j$ th PS block;  $k$  is the  $k$ th SH block;  $M_{ps}^i$  and  $M_{sh}^i$  are sets of PS and SH blocks included in the reconstructed cluster for the  $i$ th event;  $ADC_{j/k}^i$  and  $Ped_{j/k}$  represent the ADC channel number of the event and mean pedestal value in the ADC spectrum, respectively;  $P_{kin}^i$  is the particle momentum of the  $i$ th event; and  $C_{j/k}$  is the gain factor of the ADC spectrum used as a fitting parameter during the minimization.

To obtain the best fitting result, electron samples were selected from data taken with the kinematics setting at the QE tail where scattered electrons were uniformly distributed among all lead glass blocks. A Fumili minimization package [55] was called to minimize  $\chi^2$ , and the gain factors obtained from the fitting parameters were stored in the database.

Similar to the idea of the GC calibration, the calorimeter on HRS-L, composed of the layers of Pion-Rejector-1 (PRL1) and Pion-Rejector-2 (PRL2), was calibrated by aligning the minimum ionization peak of each ADC spectrum to a common channel

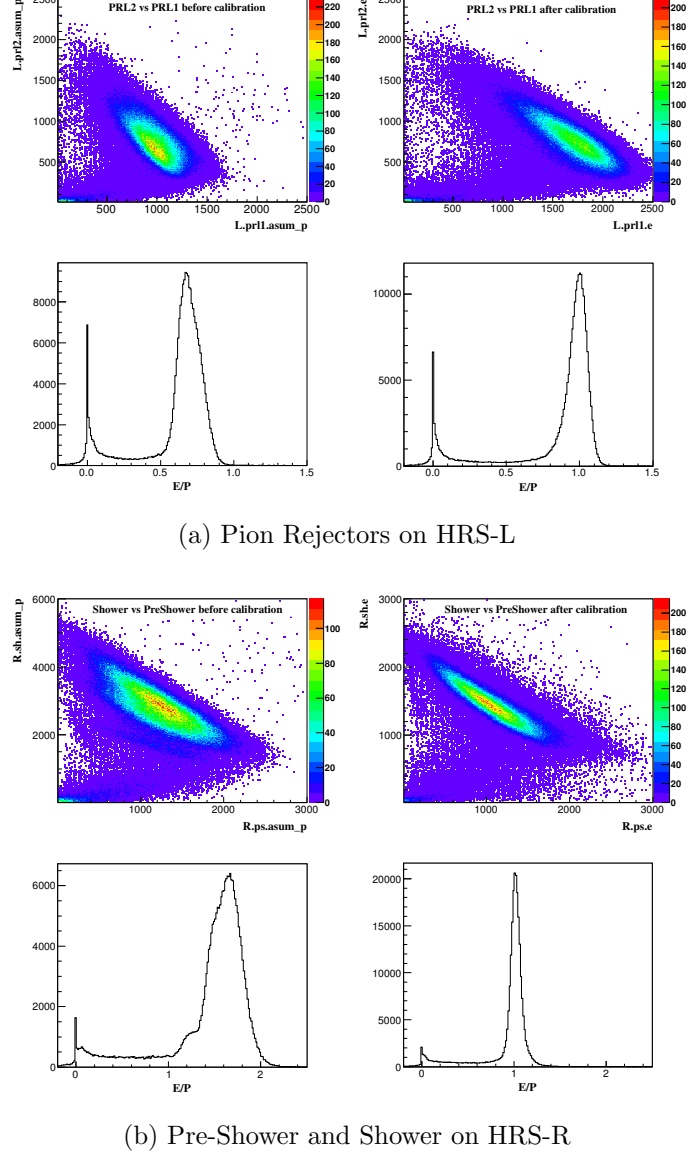


Figure 4.3: Calibration of calorimeters. In each figure, the top two plots are the 2-D histograms of the PRL1 (PS) ADC sum versus the PRL2 (SH) ADC sum before and after the calibration. The electron band is clearly isolated after the calibration. The bottom two 1-D histograms are the distributions of E/P before and after the calibration. The peak becomes sharp and locates at one with new gain factors.

number. The cosmic ray events were used during the calibration since they were uniformly distributed along the entire blocks. Furthermore, the particles in cosmic ray are mostly muons which have small energy spread. The pedestal peak ( $ADC_i^{ped}$ ) and muon peak ( $ADC_i^{muon}$ ) in the ADC spectrum of the  $i$ th PMT were located and

their distance were aligned to 100, by applying a gain factor defined as:

$$C_i = \frac{100}{ADC_i^{muon} - ADC_i^{ped}}. \quad (4.4)$$

The gain factors for all PMTs in PRL1 and PRL2 were calculated similarly. The E/P was calculated during the new data replay with these updated gain factors in the data base. To shift the peak of the E/P distribution to one, the gain factors were further adjusted:

$$C_i^{real} = C_i \times \frac{1}{M_{E/P}}, \quad (4.5)$$

where  $M_{E/P}$  represents the mean value of the E/P peak before the adjustment. The adjusted gain factors were then updated in the data base and the data was replayed again.

The calibration results of both calorimeters are shown in Fig. 4.3b and Fig. 4.3a, where electrons are better separated from backgrounds and E/P is well centered at one. The locations of E/P peaks at different momentum settings were shown in Fig. 4.4, where the energy resolutions of calorimeters were also given by fitting the spread of  $E/P$  peaks as functions of the momentum values. The total resolution of PS and SH is 2.53% per GeV. The resolution of Pion Rejectors is 3.21% per GeV which is slightly worse because they are not total absorbers.

### 4.3 HRS Calibration

After coming out from the target chamber, a charged particle travels a long distance within the HRS, and its trajectory after the Q3 exit is tracked by two VDCs which specify its position and direction at the focal plane. By using the focal plane quantities, an optics matrix reconstructs the particle's position and direction at the target plane where the electron interacts with the target.

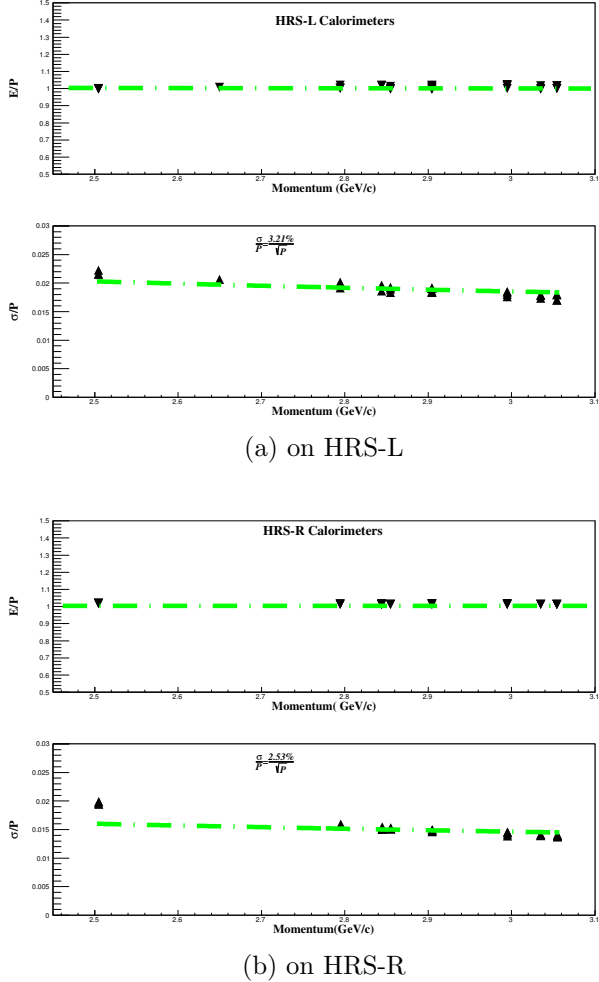


Figure 4.4: Calibration performance and resolution of calorimeters. The top plot in each figure reveals the performance of calibration at different momentum setting. The two bottom plots give the resolution of calorimeters, which are 3.21% on HRS-L and 2.53% on HRS-R.

The standard HRS optics matrices have already been extracted in previous Hall-A experiments. However, the absolute positions of the target, the HRS and detectors change from time to time, and these offsets should be taken into account in the optics matrices. Furthermore, during E08-014 experiment, the magnet field of the third Quadrupole in HRS-R (RQ3) was limited to 2.8273 GeV/c due to a power supply issue, while our maximum momentum setting was 3.055 GeV/c. The RQ3 field had to be scaled down to 87.72% of the dipole field for each setting, so the old HRS-R optics matrix was not applicable. In this section, a calibration procedure to obtain

new optics matrices for this experiment will be introduced.

### 4.3.1 Coordinator Systems

Coordinates used during data analysis are briefly presented here. A more detailed description of Hall A coordinate systems and the transportation between coordinates is given in reference [56]. Notes that angles defined in all coordinates are actually the tangent of their values.

- **Hall Coordinate System (HCS)**

The center of the HCS is defined as the intersection of the beam and the vertical axis of the target system.  $\hat{z}$  is along the direction of the beam,  $\hat{x}$  is to the left of  $\hat{z}$  and  $\hat{y}$  is vertically up (Fig.4.5).

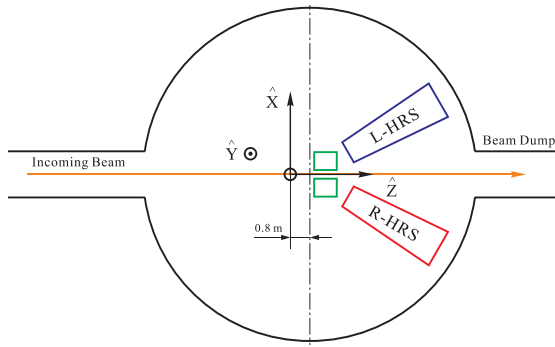


Figure 4.5: Hall Coordinate System (HCS), which defines the beam position and the target location with respect to the hall center which is given as the intersection of the beam and the vertical axis of the target system.  $\hat{x}$  is to the left of the beam direction,  $\hat{z}$ , and  $\hat{y}$  is vertically up.

- **Target Coordinate System (TCS)**

As shown in Fig.4.6,  $\hat{z}_{tg}$  is the direction from the target system perpendicularly going through the center hole of the sieve slit plane on each spectrometer. The origin of TCS is given by the intersection of  $\hat{z}_{tg}$  and the vertical axis of the target system, and  $L$  is a constant length from the origin of TCS to the sieve

slit plane.  $\hat{x}_{tg}$  is parallel to the sieve slit plane and vertically down, and  $\hat{y}_{tg}$  is to the left of  $\hat{z}_{tg}$ .  $\hat{\theta}_{tg}$  (the out-of-plane angle) and  $\hat{\phi}_{tg}$  (the in-plane angle) are taken to be  $dx_{sieve}/L$  and  $dy_{sieve}/L$ . The origins of HCS and TCS are not necessarily overlapped and the value of  $D$ , the offset between two position, changes when moving HRSs to different angles. Surveys is required during the experiment running to obtain the offset value.

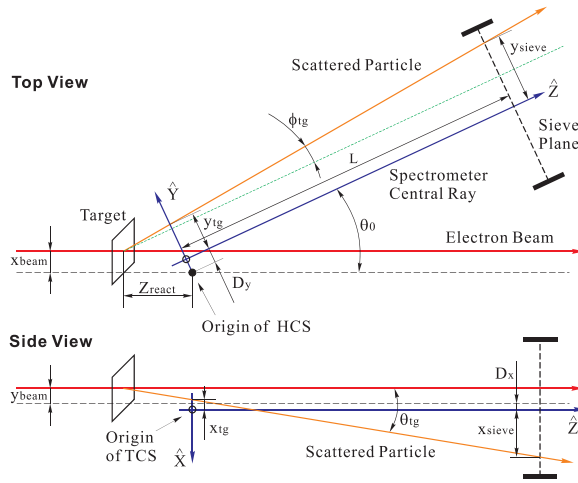


Figure 4.6: Target Coordinate System (TCS).  $\hat{z}$  goes from the target system perpendicularly to the center hole of the sieve slit plane attached on the Q1 entrance of each HRS. The intersection of  $\hat{z}$  and the vertical axis of the target system defines the origin, hence there is a potential offset between the hall center and the origin of TCS.  $\hat{x}$  is normal to  $\hat{z}$  and points down, and  $\hat{y}$  is to the left of  $\hat{z}$ .

- **Detector Coordinate System (DCS)**

The origin of DCS can be defined as the intersection point of the wire 184 of U1 plane and the wire 184 of V1 plane on the first VDC (VDC1).  $\hat{z}_{det}$  is perpendicular to the VDC planes away from HRS,  $\hat{x}_{det}$  is horizontally along the long symmetry axis of VDC1 pointing away from the hall center, and  $\hat{y}_{det}$  is vertically up toward  $\hat{z}_{det}$  (Fig. 4.7).

- **Transport Coordinate System (TRCS)**

The TRCS is generated by rotating the DCS clockwise around  $\hat{y}_{det}$  by  $45^0$  (Fig. 4.8).

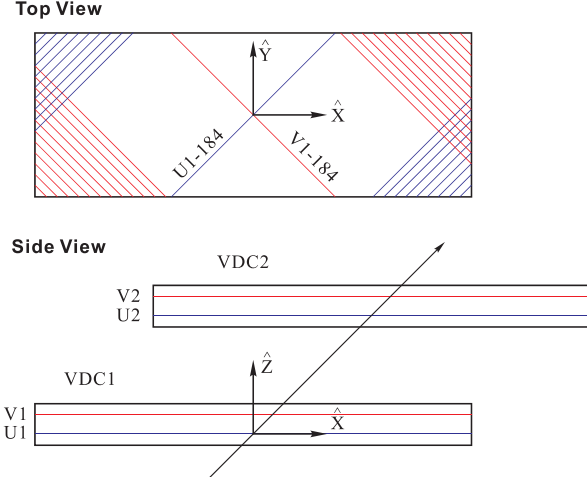


Figure 4.7: Detector Coordinate System (DCS). Its origin is given by the cross point of the wire 184 of U1 and the wire 184 of V1.  $\hat{z}$  is perpendicular to the VDCs,  $\hat{x}$  is horizontally along the long edge of the VDC and points away from the hall center, and  $\hat{y}$  is along the short edge of the VDC and vertically up.

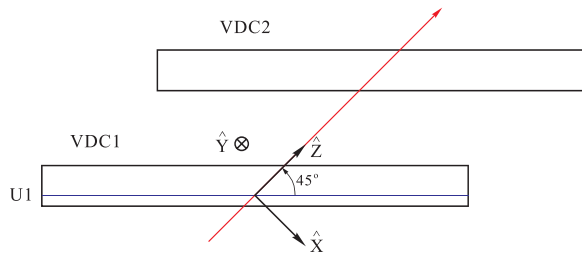


Figure 4.8: Transport Coordinate System (TRCS), which is generated by rotating the DCS clockwise around  $\hat{y}_{det}$  by  $45^0$ .

- **Focal Plane Coordinate System (FCS)**

The FCS is obtained by rotating DCS around its  $\hat{y}_{det}$  axis by an angle  $\rho$ , which is the angle between  $\hat{z}_{det}$  axis and the local central ray with  $\hat{\theta}_{tg}=\hat{\phi}_{tg}=0$  for the corresponding relative momentum  $\delta p = (p - p_0)/p_0$  (Fig.4.9).

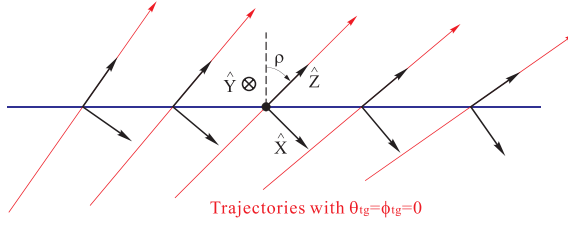


Figure 4.9: Focal Plane Coordinate System (FCS), obtained from rotating DCS around its  $\hat{y}$  by an angle  $\rho$  so  $\hat{z}$  is parallel to the central ray with  $\hat{\theta}_{tg}=\hat{\phi}_{tg}=0$  and  $\delta p = (p - p_0)/p_0$ .

### 4.3.2 Optics Optimization

The optics calibration basically follows the procedure described in the reference [56]. A optics matrix for HRS is a set of polynomial transportation functions to calculate the target plane quantities,  $\delta p$ ,  $y_{tg}$ ,  $\theta_{tg}$  and  $\phi_{tg}$ , by using the focal plane quantities,  $x_{fp}$ ,  $y_{fp}$ ,  $\theta_{fp}$  and  $\phi_{fp}$ . The functions are given as:

$$\delta p = \sum_{i,j,k,l} C_{ijkl}^D x_{fp}^i \theta_{fp}^j y_{fp}^k \phi_{fp}^l, \quad (4.6)$$

$$y_{tg} = \sum_{i,j,k,l} C_{ijkl}^Y x_{fp}^i \theta_{fp}^j y_{fp}^k \phi_{fp}^l, \quad (4.7)$$

$$\theta_{tg} = \sum_{i,j,k,l} C_{ijkl}^T x_{fp}^i \theta_{fp}^j y_{fp}^k \phi_{fp}^l, \quad (4.8)$$

$$\phi_{tg} = \sum_{i,j,k,l} C_{ijkl}^P x_{fp}^i \theta_{fp}^j y_{fp}^k \phi_{fp}^l, \quad (4.9)$$

where D-terms ( $C_{jkl}^D$ ), Y-terms ( $C_{jkl}^Y$ ), T-terms ( $C_{jkl}^T$ ), and P-terms ( $C_{jkl}^P$ ) represent the matrix elements of  $\delta p$ ,  $y_{tg}$ ,  $\theta_{tg}$  and  $\phi_{tg}$ , respectively. An optics calibration procedure is set to determine the matrix elements by using the optics data taken during the experiment.

There are three new variables in HCS which are more practical for long targets

	Angle	$D_x$ (mm)	$D_y$ (mm)	$D_z$ (mm)	Survey Report
HRS-L	21.480	1.78	1.25	-0.70	DVCS [57]
HRS-R	-20.022	-2.91	0.73	-1.06	PVDIS [58]

Table 4.1: Spectrometer offsets for survey reports, where  $D$ , the offset between the origins of HCS and TCS, is given in term of three components in HCS.

	L (mm)	$x_{sieve}$ (mm)	$y_{sieve}$ (mm)	Survey Report
HRS-L	1182.3	-1.05	0.20	DVCS [57]
HRS-R	1175.9	1.04	0.05	A1n [59]

Table 4.2: Sieve slit plates offsets from survey reports. The values were measured in HCS.

and foil targets with known offsets from the hall center:

$$z_{react} = -(y_{tg} + D) \frac{\cos\phi_{tg}}{\sin(\Theta_0 + \phi_{tg})} + x_{beam}\cot(\Theta_0 + \phi_{tg}), \quad (4.10)$$

$$y_{sieve} = y_{tg} + L \cdot \tan\phi_{tg}, \quad (4.11)$$

$$x_{sieve} = x_{tg} + L \cdot \tan\theta_{tg}, \quad (4.12)$$

where  $x_{beam}$  is the horizontal position of the beam,  $\theta_0$  is the central angle of the spectrometer, and  $L$  and  $D$  are defined in TCS.  $z_{react}$  is the reaction location along the beam direction and also provides the target position in HCS.  $x_{sieve}$  and  $y_{sieve}$  represent the vertical and horizontal positions at the sieve slit plane. During the experiment, the beam position was locked at (-2.668 mm, 3.022 mm). Table 4.1 and Table 4.2 give the values of  $D$ ,  $x_{sieve}$  and  $y_{sieve}$  from survey reports.

As given in table 4.3, a group of optics data has been taken during the experiment with the optics target which was used to calibrate  $y_{tg}$ . When taking angular calibration data, a sieve slit plate (Fig. 4.10) was attached on the entrance of Q1 for each HRS. The data was taken at QE region to ensure each hole on the sieve slit plate was covered with enough statistics.

The optics matrices used to replay optics calibration data were from previous experiments which shared similar spectrometer settings as this experiment. The initial

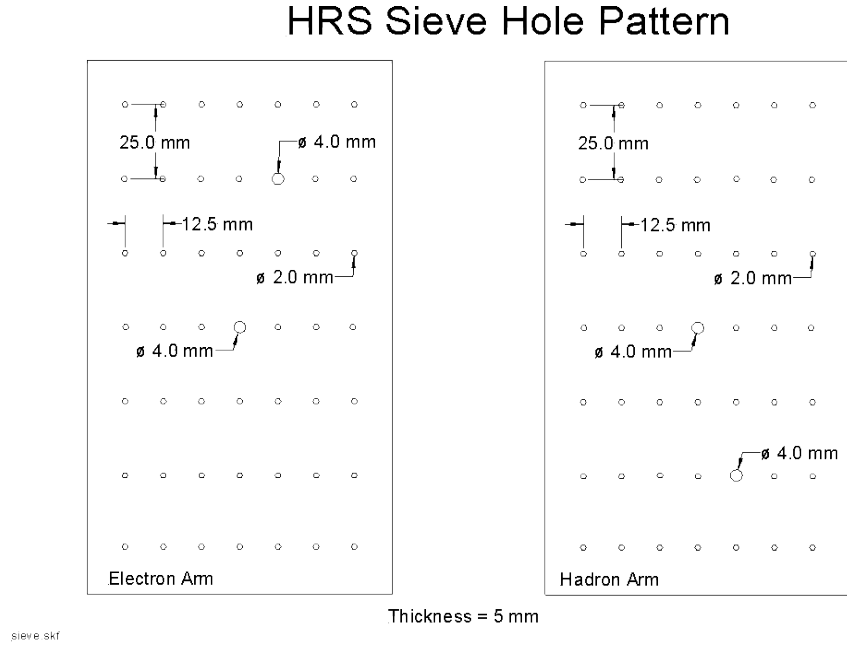


Figure 4.10: The design of sieve slit plates. Both arm have the identical plates but different mounting system. The graphic is taken from Hall A web-page.

Run Number	Target	Angle	$P_0/P_0^{RQ3}$ (GeV/c)	Raster	Sieve	Comment
3695	Dummy4cm	$23^0$	2.678/2.3492	Off	Out	$\delta p +3\%$
3698	Dummy4cm	$23^0$	2.600/2.2808	Off	Out	$\delta p 0\%$
3704	Dummy4cm	$23^0$	2.522/2.2124	Off	Out	$\delta p -3\%$
3700	Multi-C	$23^0$	2.600/2.2808	Off	Out	
3701	Multi-C	$23^0$	2.600/2.2808	On	Out	
4201-4205	Multi-C	$25^0$	2.505/2.1975	Off	In	

Table 4.3: Run list of optics data, where Dummy4cm means two dummy foils separated by 4 cm, and Multi-C means the optics target with seven carbon foils. Two HRSs took data simultaneously with the same settings.

HRS-L matrix taken from E05-102 [60] was proved to be able to reconstruct the target plane quantities with good accuracy. The matrix was refitted by using the calibration data and the updated offsets from survey reports. The HRS-R optics matrix used by previous experiments, however, performed poor reconstruction of the target plane quantities because of the mis-tuning RQ3 field, as shown in Fig. 4.11a and Fig. 4.12a. The detailed procedure to calibrate the new HRS-R optics matrix will be discussed

below.

On top of the old matrix elements, additional matrix elements were added in the optics terms to form a complete set of polynomials upto the 5th-order, but the values of new elements were all set to zero. After the calibration data being replayed with this optics matrix, events selection on the focal plane was performed to select event from main trigger (T1). One-track cut on VDCs and PID cuts on the GC and calorimeters were applied to select good scattered electrons. Events at the edge of HRS acceptance were eliminated by cutting the flat regions of the focal plane quantities.

Events from Run-3700 was used to calibrate the matrix elements in Y-terms (Eq (4.9)). When one plots the 2-D histogram of  $z_{react}$  versus  $\phi_{tg}$  (Fig. 4.11a), events scattered from a specific foil formed a strip, both ends of which were smeared due to the defocusing effect from RQ3. The first iteration was to select events near the center of each strip (within the red boxes in Fig. 4.11a), and events in the overlap regions were discarded. The real value of  $z_{react}$  for each event was assigned with the position of the foil where the event belongs to. After the offsets in Table 4.1 and Table 4.2 being updated in the calibration, the matrix elements in Y-terms were fitted by an optics optimizer based on the Minuit minimization method [61]. The high order elements in Y-terms were generally removed before the minimization starts to fluctuate. The data was replayed with the new matrix elements updated in the database and the big improvement of  $z_{react}$  distribution is demonstrated in Fig. 4.11b.

The procedure of calibrating T-terms and P-terms was similar but used calibration data taken with a sieve slit plate (Run-4201~4205). The data were firstly replayed with new elements of Y-terms. The sieve slit patterns shown in a 2-D plot of target plane quantities  $\theta_{tg}$  and  $\phi_{tg}$  were compared with the design of the sieve slit plate in Fig. 4.10. In the left plots of Fig. 4.10, each spot corresponds to the one sieve slit hole. For an event which could be clearly identified from a spot, the coordinate of this event on the sieve slit plane,  $(x_{ss}, y_{ss})$ , was given as at the center of the hole since

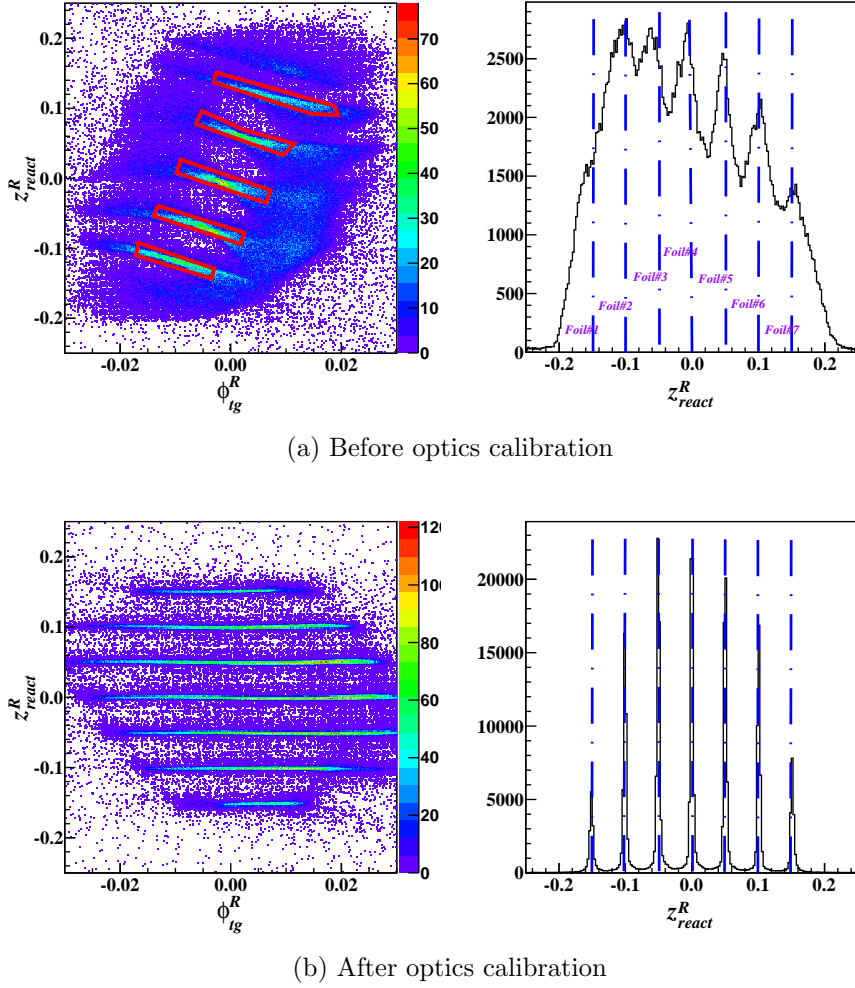


Figure 4.11:  $Z_{react}$  distribution before and after the optics calibration. The 2-D plots reveal that each strip represents electrons scattered from the corresponding foil indicated in the 1-D plots. The red boxes in the first 2-D plot represent graphic cuts applied to selected good electron samples during the first iteration of the Y-terms calibration.

the diameter of the hole is tiny. The values of  $\theta_{tg}$  and  $\phi_{tg}$  can be directly calculated from the values  $x_{ss}$  and  $y_{ss}$ .

The matrix elements of T-terms and P-terms were fitted separately with the same optimizer and unnecessary matrix elements were carefully checked and removed. Fig. 4.12b shows that the sieve slit holes were well aligned after the calibration of angular terms.

With updated Y-terms, T-terms and P-terms in the data base, the calibration runs

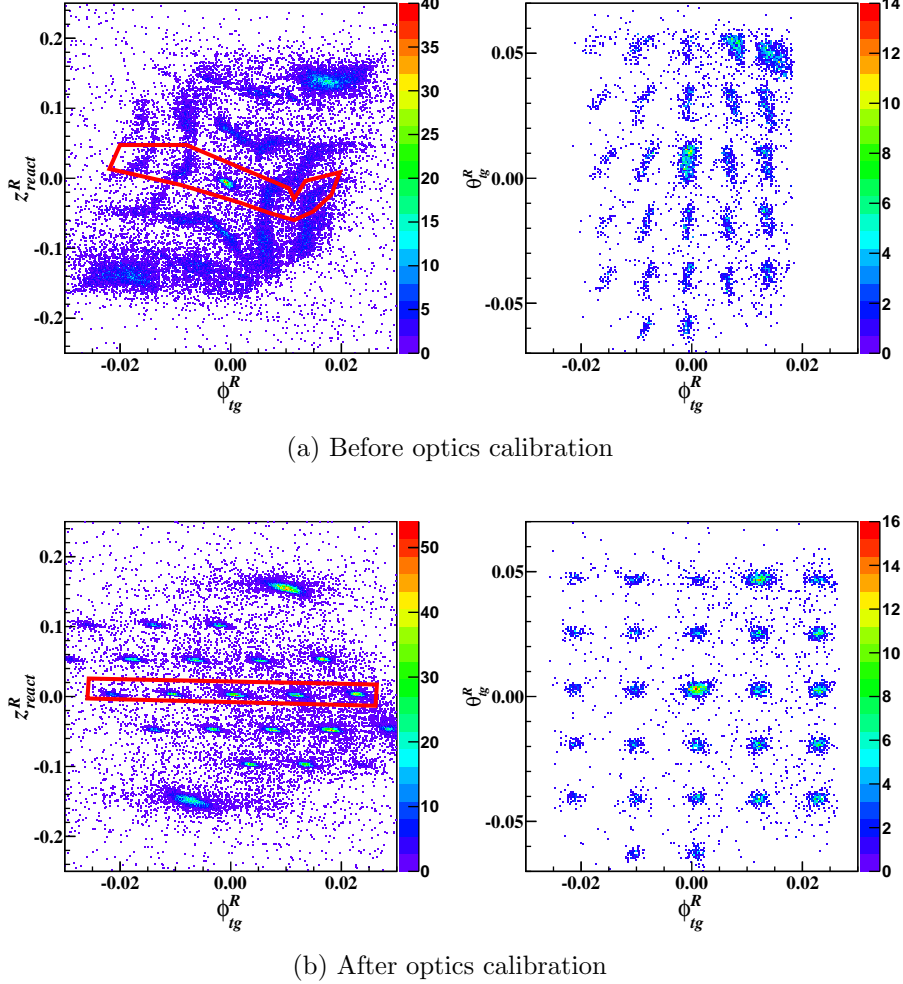


Figure 4.12:  $Z_{react}$  Sieve slit pattern before and after the optics calibration. Cutting on a single foil (the red box) is required to see the clear sieve slit pattern. Events from each hole are individually extracted and assigned with the values of  $\theta_{tg}$  and  $\phi_{tg}$  at the center of the hole.

were replayed again, and the second iteration was proceeded with more good events included since the reconstruction of target plane quantities became much better. The calibration was completed when the fluctuation of the minimization began after several iterations.

The calibration of D-terms requires the calibration data taken when the central momentum was intentionally shifted by small values, for example, off by  $\pm 3\%$ . However, the experiment was running at QE region and the peak of the momentum distribution was too broad to be sensitive to the small offsets. Without the elastic data, the D-

terms was unable to calibrated. In Appendix C, a different method was discussed to obtain the correct  $\delta p$  reconstruction.

# Chapter 5

## Extracting Cross Sections

### 5.1 Overview

Assuming the data is binned in the energy of scattered electrons,  $E'$ , the experimental raw cross section is usually written as:

$$\frac{d\sigma_{EX}^{raw}}{dE'd\Omega}(E_0, E'_i, \theta_0) = \frac{N_{EX}^i \cdot \epsilon_{e-\pi}}{N_e \cdot N_{tg} \cdot \epsilon_{eff} \cdot (\Delta E'_{EX} \Delta \Omega_{EX})} \quad (5.1)$$

where the superscript  $i$  denotes the  $i$ th bin.  $E_0$  is the initial energy which is fixed to 3.356 GeV in E08-014,  $E'_i$  is the scattered energy at the center of the bin, and  $\theta_0$  is the central scattering angle.  $\Delta E'$  and  $\Delta\Omega = \Delta\theta_{tg} \cdot \Delta\phi_{tg}$  are the momentum acceptance and the solid angle acceptance of the spectrometer;  $N_{EX}^i$  is the number of scattered electron events in this bin;  $N_{tg}$  is the total number of scattering centers;  $N_e$  is the accumulated electron charge from the beam; and  $\epsilon_{eff}$  is the total efficiency of all detectors combined, including the detection efficiency and the cut efficiency.  $\epsilon_{e-\pi}$  denotes the percentage of electrons in  $N_{EX}$  when there is still certain amount of pions contaminated in the data after the PID cuts. In the rest of this chapter, the differential form of the cross section,  $\frac{d\sigma}{dE'd\Omega}(E_0, E'_i, \theta_0)$ , is abbreviated to  $\sigma(E'_i, \theta_0)$ .

The raw cross section in Eq (5.1) requires additional corrections to remove the

effects from the spectrometer acceptance. Because  $E_0$  and  $E'_i$  are altered when the electron goes into and comes out from the target, the experimental cross section is usually called the radiated cross section and has to be further corrected by the radiative corrections. The final cross section is the born cross section, which can be directly compared with the theoretical calculations.

The basic procedure of extracting cross sections from experimental data is demonstrated in Fig. 5.1. First of all, the signals from detectors and electronics were stored in the raw data in the form of TDC channels, ADC channels and scaler counts. These signals have to be properly calibrated and converted into applicable quantities. The calibrated HRS optics matrix reconstructs the scattered electron's momentum, scattering angle and reaction point at the target plane. The full set of raw data was replayed with updated parameters in the data base. The calibration of detectors and the HRS optics matrices have been introduced in previous chapter.

Secondly, results of the beam charge monitor (BCM) calibration convert the BCM scaler counts into electron beam charge. The dead-time caused by the DAQ system is needed to be evaluated.  $N_{tg}$  is determined by the target thickness after the boiling study. Good electrons are identified by applying cuts on calibrated detector signals, and the efficiencies of the event selection can be individually evaluated. By binning the data with the kinematic variable, e.g.  $E'$ , in its proper acceptance range, one can extract the experiment yield in each bin. These procedures will be given in this chapter.

Meanwhile, the single arm Monte Carlo simulation (SAMC) generates simulation events with the same kinematic setting but with wider acceptance range to correct the acceptance effect of HRS. After weighting the simulation events with the cross sections calculated from models (e.g. XEMC in this experiment), the simulation yields were extracted with the same acceptance cuts and binning method. The Monte Carlo simulation and cross section models will also be discussed in this chapter.

## The flow-chart to extract inclusive cross sections

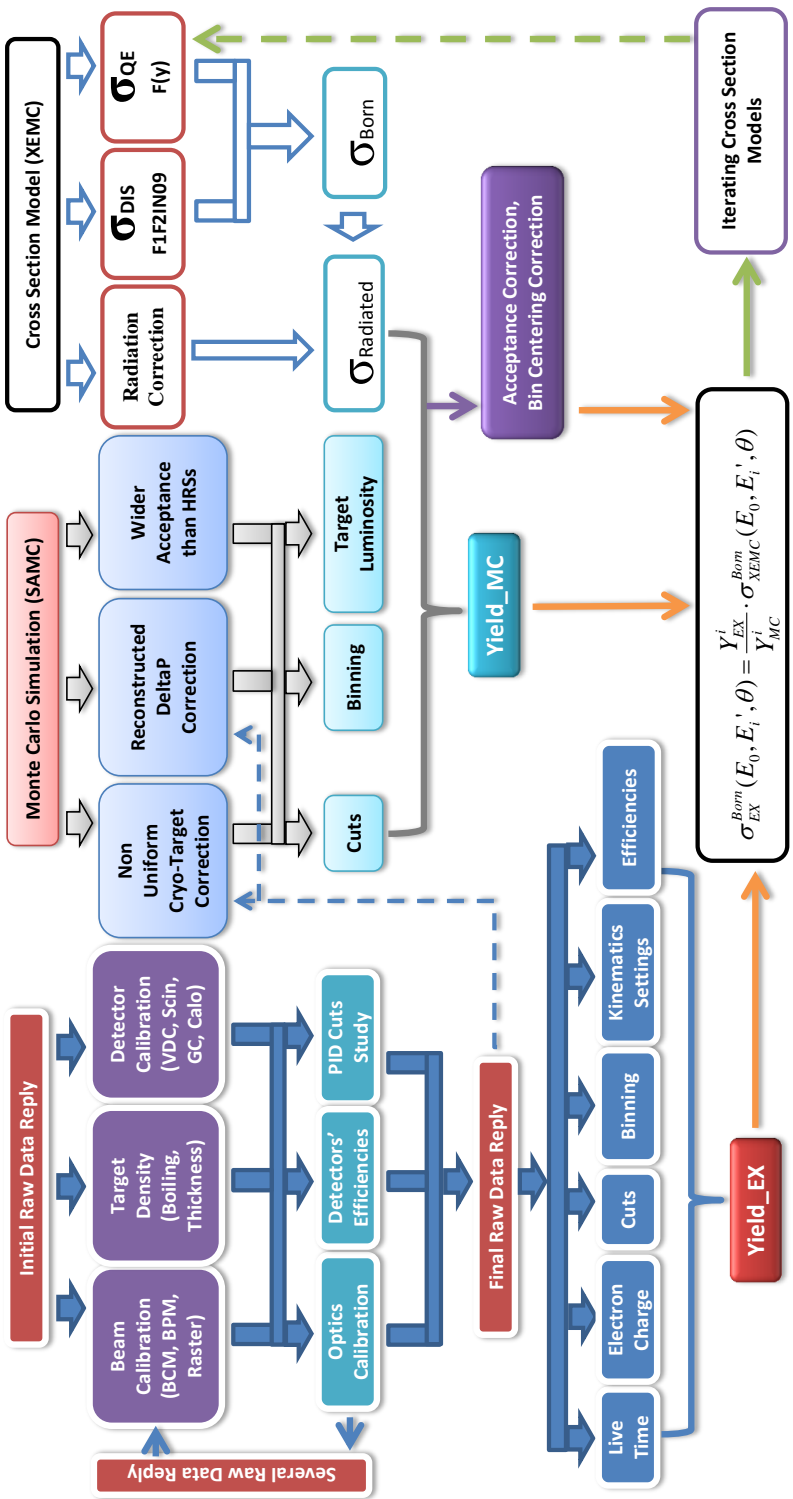


Figure 5.1: Flow-chart to extract cross section

Finally, the yield ratio method used to extract the cross sections will be introduced, followed by a discussion of errors.

## 5.2 Electron Charge

The accumulated electron charge from the beam was monitored by BCMs, the signals of which were recorded in scalers. The scalers signals, in term of number of counts, have been calibrated [44] to correctly reflect the accumulated electron charge. When the beam is stable during one run, the total electron charge is simply the product of the beam current and the total run time, and should be directly proportional to the total number of scaler counts. However, events taken during the beam trips are removed when the beam becomes unstable, hence the electron charge should be evaluated differently.

The average electron beam current in between two consecutive scaler events, called the real-time current, is calculated from the total electron charge collected between these events divided by the time gap. For example, between the  $i$ th and the  $i + 1$ th event, the real-time current measured by the upstream BCM scaler,  $U_1$ , is given by:

$$I_i^{U_1} = \Delta C_i^{U_1} / \Delta T_i, \quad (5.2)$$

where  $\Delta C_i^{U_1} = C_{i+1}^{U_1} - C_i^{U_1}$  gives the charge accumulated between two scaler events with the time gap,  $\Delta T_i = T_{i+1} - T_i$ . Similarly, the real-time current measured by the downstream BCM scaler,  $D_1$ , is also calculated. There are other BCM scaler signals,  $U_3$  and  $U_{10}$  ( $D_3$  and  $D_{10}$ ), which basically measure the same charge signal as  $U_1$  ( $D_1$ ) but with 3 times and 10 times amplification, respectively. These signals were not involved in the calculation since the experiment used very high currents. The beam

trip cut is applied on the average of the four real-time current values:

$$\frac{1}{2}(I_{i^*}^{U_1} + I_{i^*}^{D_1}) > I_{beam\_trip\_cut}. \quad (5.3)$$

where the cut value can be any value in between zero (when beam is tripped) and the value slightly below the maximum current. In this analysis, the beam trip cut is chose to be 50% of the normal beam current.

The total electron charge after the beam trip cut is given as:

$$N_e = \frac{1}{2} \sum_{i^*} (\Delta C_{i^*}^{U_1} + \Delta C_{i^*}^{D_1}), \quad (5.4)$$

where  $i^*$  means summing over scalar events with beam current  $I_{i^*}$  higher than the cut.

After the data replay, scalar events are stored in the scalar trees, **RIGHT** for HRS-R and **LEFT** for HRS-L, respectively, and they are synchronized with trigger events in the **T** tree. There are certain number of trigger events recorded between two consecutive scalar events, and these events are assigned with the same beam current value when the real-time current between these two scalar events is evaluated. Consequentially, a beam trip cut removes all trigger events in between two scalar events if the real-time current is lower than the cut.

During this experiment, BCM scalers on HRS-L did not work properly. Due to the fact that the scalers on both HRSs record the same BCM signals, the real-time current for data taken in HRS-L is calculated using scalar events in HRS-R.

### 5.3 Dead-Time

Dead-time includes the electronic dead-time and the computer dead-time. The former refers to the situation when the coming trigger events are discarded when the front-

end electronics of the DAQ system are processing the current trigger, and the later is due to the limitation of the computer speed which causes the lose of new events when the computer is writing the current event into the hard disk. Unless the computer is overloaded by processes other than the DAQ system, the computer dead-time is negligible due to the usage of fast hard-drives.

One evaluates the dead-time as the percentage of the trigger events being discarded to the total trigger events provided by detectors in a certain amount of time. The value of the dead-time directly depends on the performance of electronics and computers, but is also highly related to the the total trigger rates. Other than increasing the performance of hardware, one typical method to reduce the dead-time is to control the total trigger rates below reasonable values by assigning a pre-scale factor to each trigger.

During data taking dead-time is monitored by using the electron dead-time monitor module (EDTM) which mixes pulse signals with fixed frequency into TDC signals from detectors. Since within a certain amount of time the total number of the pulse signals is known, the online dead-time value can be given by calculating the percentage of the pulse signals which are not recorded by the DAQ system. The value was usually controlled under 30% by changing the pre-scale factors before the start of the each run.

During the offline analysis, the average values of Dead-Time for the main production triggers were calculated individually for each run. The total number of events recorded by the DAQ system were scaled by the pre-scale factor but scalers count all events from each trigger. Hence the average dead-time value for the *i*th trigger is given by:

$$DT_{T_i} = 1 - \frac{PS_{T_i} \cdot N_{T_i}^{DAQ}}{N_{T_i}^{Scaler}}, \quad (5.5)$$

where  $N_{T_i}^{Scaler}$  and  $N_{T_i}^{DAQ}$  are the total number of scaler counts (in **RIGHT** for  $i = 1$  or **LEFT** tree for  $i = 3$ ) and trigger events (in **T** tree) in one run, respectively.  $PS_{T_i}$

is the pre-scale factor of the trigger. Events taken during the beam trip were removed since their rates were much lower than the normal rates.

A different quantity, live-time ( $LT_{T_i} = 1 - DT_{T_i}$ ), is more commonly used in the data analysis. The total number of good events selected for data analysis should be corrected by the live-time for each run:

$$N_{EX}^r = PS^r \cdot \frac{N_{recorded}^r}{LT^r}, \quad (5.6)$$

where  $PS = PS1$  for HRS-R and  $PS = PS3$  for HRS-L;  $r$  denotes the run number;  $N_{EX}^r$  and  $N_{recorded}^r$  are the number of selected events which create triggers and the number of those events which are recorded by the DAQ system after pre-scaling, respectively. Note that without event selection, e.g., PID cuts,  $N_{recorded}^r = N^{r,DAQ}$ .

In this experiment, since only events from  $T_1$  ( $T_3$ ) were used for data analysis on HRS-R (HRS-L), the subscript,  $T_i$ , is omitted from any future discussion.

## 5.4 Targets

The total scattering center in Eq (5.1), or sometimes called the target luminosity, is calculated with known target thickness:

$$N_{tg} = \frac{\rho \cdot l \cdot N_a}{A}, \quad (5.7)$$

where  $\rho$  is the density of the target material in  $g/cm^3$ ,  $l$  is the effective target length in  $cm$ ,  $N_a$  is the Avogadro's number and  $A$  is the nuclear number of the target.

### 5.4.1 Cryo-Target Boiling Study

When the electron beam is delivered to the target, the local temperature fluctuates and can cause the target density to vary with the beam current. Such a phenomena is

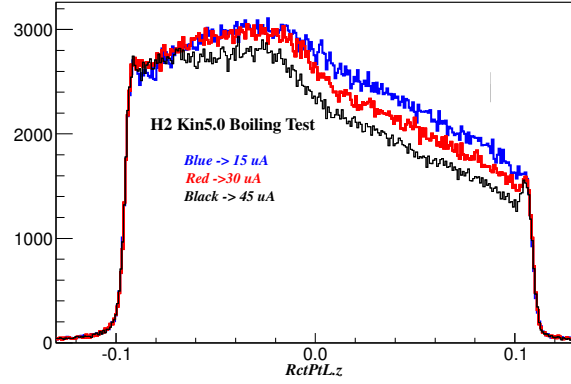
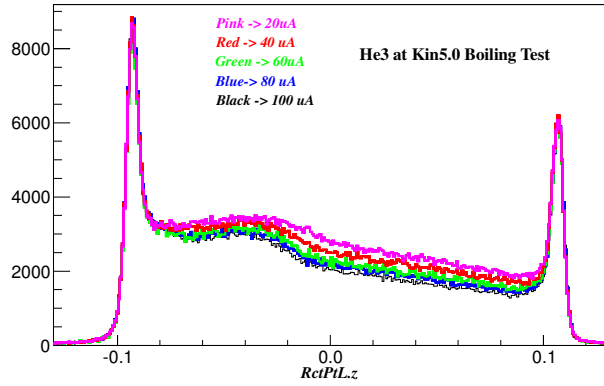
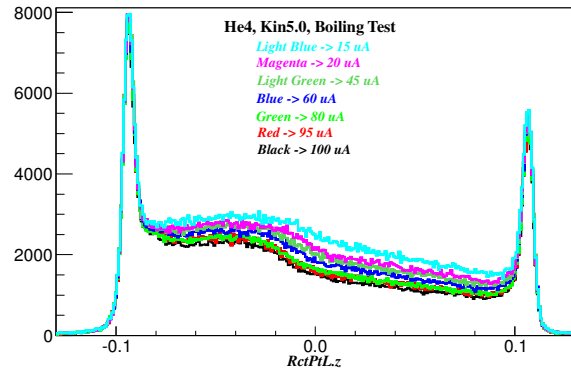
(a)  $^2H$ (b)  $^3He$ (c)  $^4He$ 

Figure 5.2: Cryo-target bumps on  $z_{react}$  distributions due to the non-uniform density of long target. Three plots show the bump changing with beam current.

called the boiling effect. While the density variation of solid targets is usually small, liquid and gas targets have significant boiling effects and their densities correlate to

the beam current:

$$\rho_{cor} = \rho \cdot (1.0 - B \cdot I/100), \quad (5.8)$$

where  $I$  and  $B$  are the values of the beam current and the boiling factor for the target, respectively.

In E08-014, three cryogenic targets (cryo-targets),  $^2\text{H}$ ,  $^3\text{He}$  and  $^4\text{He}$ , were stored in 20 cm long aluminium cells. The design of the target flow resulted in a target density non-uniformly distributing along the target cell. When the beam is on, the boiling effect varied at different parts of the cell because the cooling flowed horizontally from upstream to downstream along the target. Fig. 5.2 shows the irregular density distribution and strong correlation between the density and the beam current. The luminosities of these cryo-targets can not be simply calculated from Eq (5.7).

A detailed treatment of these cryo-targets is discussed in Appendix D. A Monte Carlo simulation of the cryogenic target system demonstrated that the non-uniform distributions did not result from beam hitting other components in the target system. The boiling study was performed by dividing each target into several sections along the cell, where the boiling effect was individually evaluated. The relative density distribution of each target was extracted from the  $z_{react}$  distribution of the experimental data by using simulation data to remove the acceptance effect and the cross section effect. Since the target pressure and temperature were well maintained during the experiment, the absolute density should not deviate from the initial value in the installation report [48], and the small change was normalized by comparing the experimental yields to the simulation yields.

## 5.5 Detector Efficiencies

Every detector is designed to be sensitive to certain types of particles within the known energy ranges. However, due to the limitation of its performance, the detector is not

necessarily able to measure all of such particles which pass through it. The percentage of particles being detected is called the detection efficiency ( $\epsilon_{det}$ ). Additionally, a certain number of good events are discarded during the data analysis by applying cuts on the detector's quantities. The percentage of good events remained after these cuts is usually named the cut efficiency ( $\epsilon_{cut}$ ). In other words, the detection efficiency and the cut efficiency denote the survival rate of particles at the hardware level and at the software level, respectively. In this section, the efficiencies of the HRS detectors will be individually evaluated.

### 5.5.1 Trigger Efficiency

The traditional HRS production trigger is generated by the coincidence of logic signals from two scintillator planes (S1 and S2m), so the trigger efficiency is equal to the total detection efficiency of these two scintillators. The inefficiency rises when either S1 or S2m does not fire when a particle passes through. As discussed in Section 3.7, T2 (T4) is the trigger generated when only one of S1 and S2m signals coincide with the gas Cherenkov (GC) signal on HRS-R(-L). With the events from T2 (T4), one can calculate the trigger efficiency of T1 (T3), or equivalently T6 (T7) in E08-014, as follow:

$$\epsilon_{trig} = \frac{PS1(3) \cdot N_{T1(3)}}{PS1(3) \cdot N_{T1(3)} + PS2(4) \cdot N_{T2(4)}}, \quad (5.9)$$

where  $N_{T1(2,3,4)}$  is number of events triggered by T1(2,3,4) and PS1(2,3,4) is the prescale factor of the trigger.

Note that Eq. (5.9) is only valid when the GC has 100% detection efficiency. Particles creating T1 (T3) Events ( $N_{T1(3)}$ ) may not necessarily fire the GC, but events from T2 (T4) are recorded when the GC is fired, so  $N_{T2(4)}$  has to be corrected by the

detection efficiency of the GC. The trigger efficiency should be given by:

$$\epsilon_{trig} = \frac{PS1(3) \cdot N_{T1(3)}}{PS1(3) \cdot N_{T1(3)} + PS2(4) \cdot N_{T2(4)} / \epsilon_{det}^{GC}}, \quad (5.10)$$

where  $\epsilon_{det}^{GC}$  is the detection efficiency of the GC. The HRS GCs usually have very high efficiency on detecting electrons so Eq. (5.9) is still valid. However, when the inefficiency of the GC rises the trigger efficiency has to be corrected by independently evaluating the detection efficiency of the GC.

Since the design of T1 and T3 in E08-014 involves S1, S2m and the GC, events from T1 (T3) and T2(T4) are all triggered by requesting logic signals from the GC. The trigger efficiency does not depend on the detection efficiencies of the GC, which has been cancelled in Eq (5.9):

$$\begin{aligned} \epsilon_{trig} &= \frac{PS1(3) \cdot N_{T1(3)} / \epsilon_{det}^{GC}}{PS1(3) \cdot N_{T1(3)} / \epsilon_{det}^{GC} + PS2(4) \cdot N_{T2(4)} / \epsilon_{det}^{GC}} \\ &= \frac{PS1(3) \cdot N_{T1(3)}}{PS1(3) \cdot N_{T1(3)} + PS2(4) \cdot N_{T2(4)}}. \end{aligned} \quad (5.11)$$

In a word, the assumption that the trigger efficiency and the detection efficiency of S1 and S2m are equivalent is only valid when both T1 (T3) and T2 (T4) involve the logic signal from the GC.

The trigger efficiencies of T1 and T3 were calculated individually for each run, shown in Fig. 5.3. The results show that the triggers have very high efficiencies.

### 5.5.2 Vertical Drift Chamber Efficiency

The detection efficiency of vertical drift chambers (VDCs) is usually very high and any inefficiency is mainly caused by the mis-reconstruction of particle tracks given by the tracking algorithm. Only events with one track are kept for data analysis, and other events with zero-track and multi-tracks are discarded by applying a one-track-

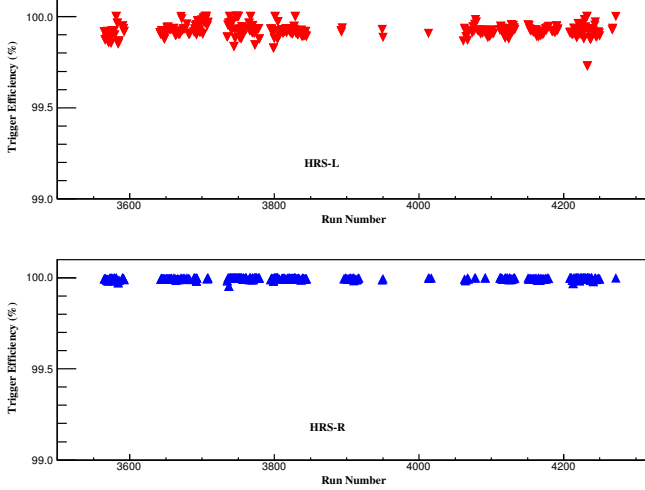


Figure 5.3: Trigger Efficiency vs Run Number, where the top plot is for T3 trigger on HRS-L and the bottom plot is for T1 trigger on HRS-R.

cut. The cut efficiency is generally called the one-track-cut efficiency, which is defined as:

$$\epsilon_{vdc} = \frac{N_{Track=1}}{N_{0 \leq Tracks \leq 4}}, \quad (5.12)$$

where  $N_{Track=1}$  is the number of events with only one track and  $N_{0 \leq Tracks \leq 4}$  is the number of events with tracks less than 4. Events with tracks more than 4 are extremely rare for HRS VDCs.

To correctly evaluate  $\epsilon_{vdc}$ , good electrons were sampled by applying cuts on detector quantities. Any quantity that requires tracking information were avoided when selecting electrons, such as the quantities derived from VDCs, the acceptance cuts on the focal plane and the target plane quantities, and the energy sum of the calorimeter which requires the tracking information during the cluster reconstruction. Electrons can be alternately identified by cutting the calibrated ADC sum of the calorimeter and the GC's calibrated ADC sum. Events with multi-tracks can also be caused by multiple particles coming in one trigger window, and such events can be eliminated by requiring only one hit in each scintillator plane. Note that because paddles in S1 are overlapped, many good events coming through the overlapped region are discarded

by applying such a cut, which should be avoided for any other part of data analysis.

Cosmic ray events usually come into the VDC with large angles and give bad tracking reconstruction, and they can be eliminated by cutting on the time-of-fly velocity ( $\beta_{TOF}$ ) which is calculated from the timing quantities of S1 and S2m. However, these timing quantities were not able to be calibrated in this experiment due to the bad TDC signals, so cosmic ray events were not removed. To reduce the effect from the cosmic ray background, data with high trigger rates, such as the carbon target data taken at the kinematic setting on the QE peak, were used to calculate the one-track-cut efficiency. From Table 5.1, the fraction of one-track and multi-track events are listed, where the one-track efficiency is mostly above 99%. The detection efficiency is the essential property of the detector and should not depend on the kinematic setting, hence one can conclude that the real value of the one-track-cut efficiency can be equal to the values calculated with data taken at high rates.

Number of tracks	0	1	2	3	4
HRS-L	0.0298%	99.1750%	0.7430%	0.0452%	0.0048%
HRS-R	0.0482%	99.3600%	0.5446%	0.0388%	0.0073%

Table 5.1: Fraction of different tracks events from quasi-elastic data,w/o  $\beta$  cut

### 5.5.3 Particle Identification Efficiencies

Electrons are identified by the GC and the calorimeter on each HRS. The GC gives high detection efficiency, since the energy threshold for electrons to create Cherenkov radiation is only 18 MeV while pions and other heavy particles must have their energy above 4 GeV to fire the detectors. The efficiency is mainly related to the performance of mirrors in the detector to collect and focus the Cherenkov light.

The detection efficiencies of the calorimeters are expected to be lower than the GCs. Each calorimeter is composed of many lead glass blocks, so the inefficiency arises when particles go through gaps in between blocks or hit the edges of the detector

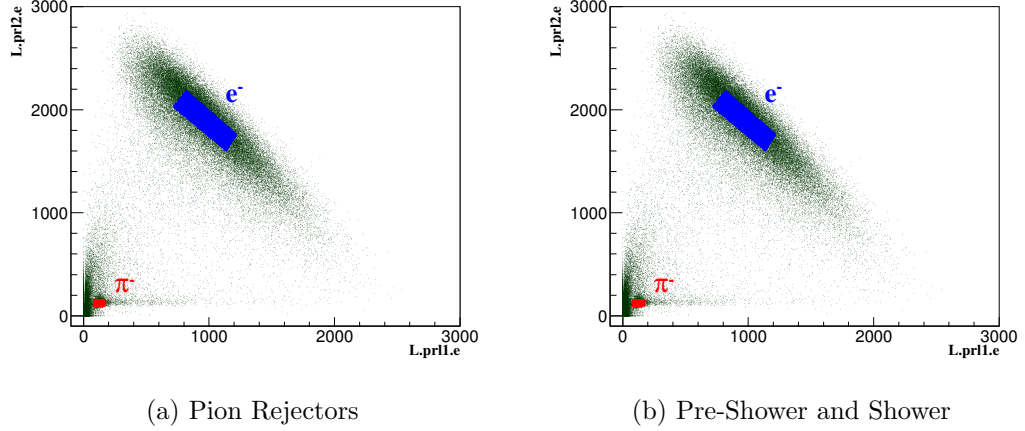


Figure 5.4: Electron (blue) and pion (red) samples from the calorimeters. In each plot, the x-axis and the y-axis are the total energies collected by the first layer and the second layer of the calorimeter, respectively. Electrons create large signals either in the first or the second layer during the cascade while the signals created by pions are relatively small in each layer. Graphic cuts were applied on these color regions to select the electrons and pions.

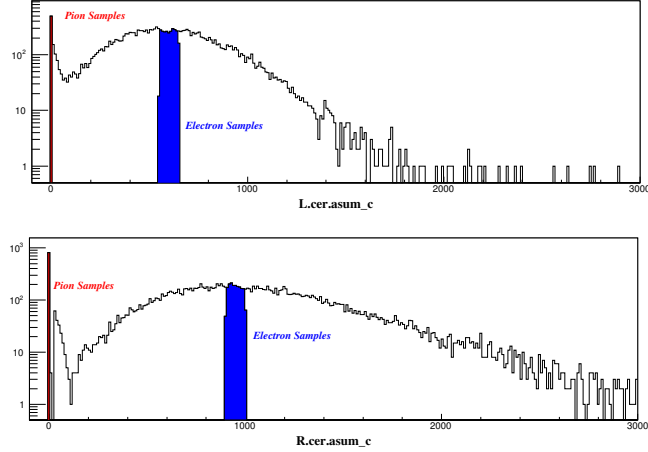


Figure 5.5: Electron and pion samples from the GC. Electrons were selected by applying cut on the main peak of the ten Cherenkov PMTs' ADC sum. Pions can not directly create Cherenkov light and they were selected by cutting on low ADC values since they leave very weak signals in the detector.

before it creates a shower.

During the offline analysis, the particle identification (PID) of electrons was performed by applying cuts on the calibrated quantities of the GC and the calorimeter. The cuts can reject most of unwanted particles, i.e., pions, and on the other hand,

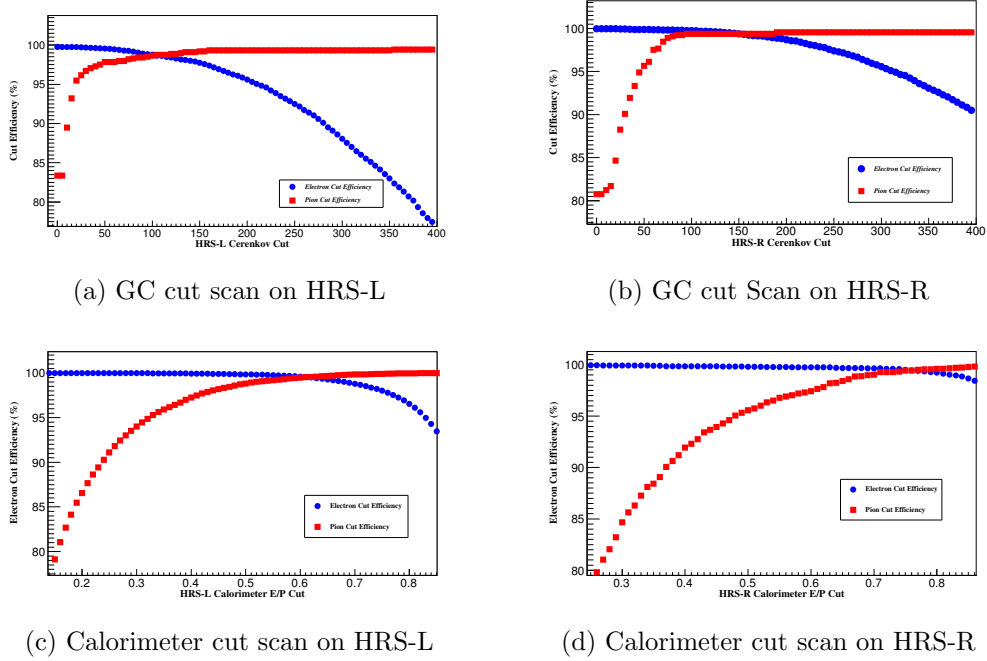


Figure 5.6: Cut scan of the GCs and the calorimeters on HRS-L (left) and HRS-R (right). The cut efficiencies of pion (red boxes) and electrons (blue dishes) were calculated with Eq. (5.13) and Eq. (5.9) by varying the cut on the GC or the calorimeter.

they may also accidentally discard good electrons. The PID study aims to obtain the optimized PID cuts on the GC and the calorimeter which can nearly eliminate pions while keeping as many electrons as possible. The cut efficiencies of the GC and the calorimeter have to be individually evaluated to correct the percentage of electrons lost during the cuts.

During the analysis of the GCs and the calorimeters, the detection efficiencies are usually evaluated together with the cut efficiencies based on the fact that one studies the detector with events which have already been detected.

In general, for experiments with a large pion background, evaluating the percentage of residual pions mixed into the electron events ( $\epsilon_\pi = 1 - \epsilon_{e-\pi}$ ) is also very crucial. However, the pion production rate during E08-014 was very low compared with the electron rate in the QE region, and additionally, the new trigger design had already removed most of pions during online data taking by introducing the GC in the trigger

system. Hence the value of  $\epsilon_\pi$  is expected to be very small.

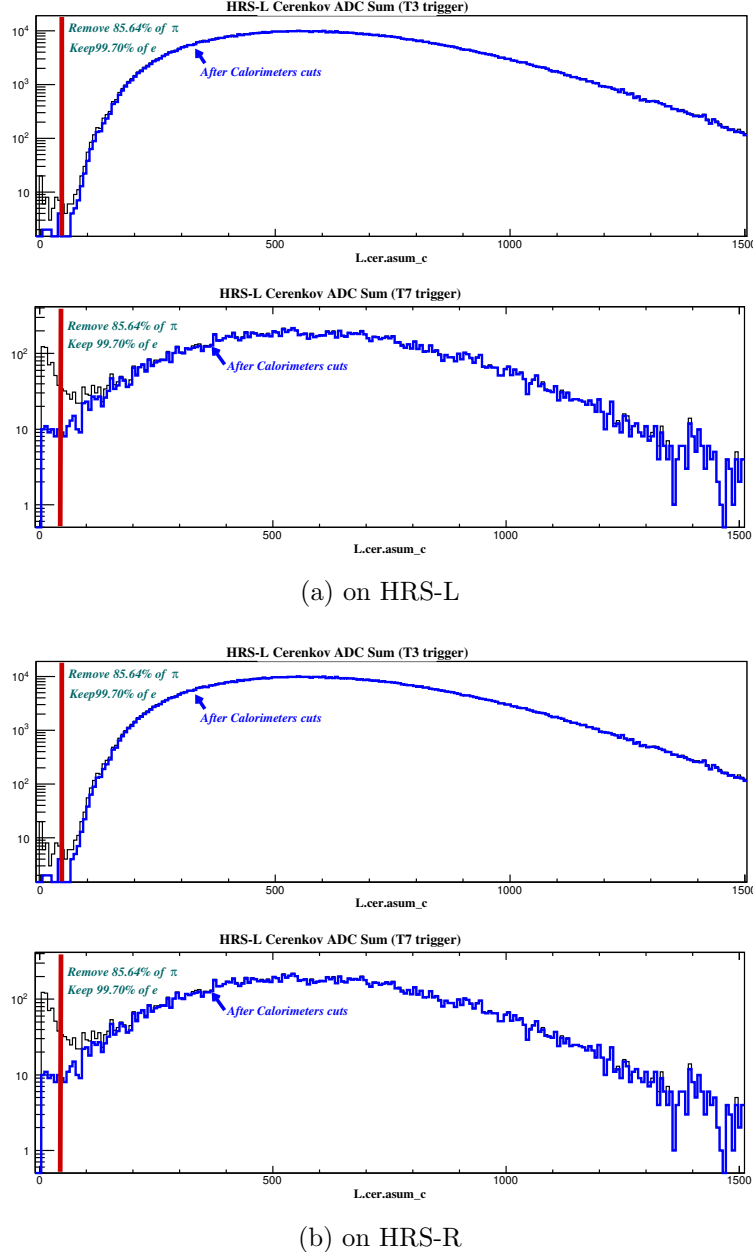


Figure 5.7: PID cut on the GCs. In each panel, the top and bottom histograms plot the calibrated ADC sum of events triggered by T1 (T3) and T6 (T7) from HRS-R (HRS-L), respectively. Most of pions have already be rejected in events from T1 and T3 during data taking, so a minimum cut on the GC's ADC spectrum ( $\geq 50$ ) can further remove rest of pions.

Events from the T6 and T7 triggers were used to study the PID cut efficiencies since they contain the most pions. The VDC one-track-cut and the acceptance cuts

were applied to select good events. Then pure pion samples and pure electrons samples were chosen from the calorimeter (GC) when studying the cut efficiency of the GC (calorimeter). The pion rejection efficiency was defined as the percentages of pions removed by applying the PID cuts:

$$\epsilon_{\pi\_rej}^{GC(cal)} = \frac{N_{\pi}^{GC(cal)}}{N_{\pi\_samples}^{calo(GC)}}, \quad (5.13)$$

and the electron cut efficiency can be calculated from:

$$\epsilon_{e\_cut}^{GC(cal)} = \frac{N_e^{GC(cal)}}{N_{e\_samples}^{calo(GC)}}, \quad (5.14)$$

where  $N_{\pi\_samples}^{calo(GC)}$  ( $N_{e\_samples}^{calo(GC)}$ ) is the pion (electron) samples from the calorimeter (GC) (Fig. 5.4 and Fig. 5.5).  $N_{\pi}^{GC(cal)}$  is the number of pions rejected and  $N_e^{GC(cal)}$  is the number of electrons left over after cutting on the GC (calorimeter), respectively.

As shown in Fig. 5.6, a cut scan was performed to study the distributions of the pion rejection efficiencies and the electron cut efficiencies by varying the cuts on the GCs and the calorimeters. Fig. 5.7a and Fig. 5.7b show that for the GC, the cut at the low value of the calibrated ADC sum, e.g.,  $L.cer.asum\_c \geq 50$  for HRS-L or  $R.cer.asum\_c \geq 50$  for HRS-R, can already remove most of pions while keep more than 99% of electrons. The combined cuts on the calorimeter,  $E/P \geq 0.5$  and  $L.prl2.e \geq 100$  ( $R.sh.e \geq 200$ ), can further remove more than 90% of pions while there is still more than 99% of electrons remaining ( see Fig. 5.8a and Fig. 5.8b). In total, on HRS-L (HRS-R), 99.85% (99.62%) of pions are eliminated with these combined PID cuts, while 99.58% (99.86%) of electrons survives after the cuts. Considering the high electrons rates and low pion production for this experiment, one is not required to specially correct the pion contamination and the value of  $\epsilon_{e-\pi}$  in Eq. (5.1) was set to one during the calculation.

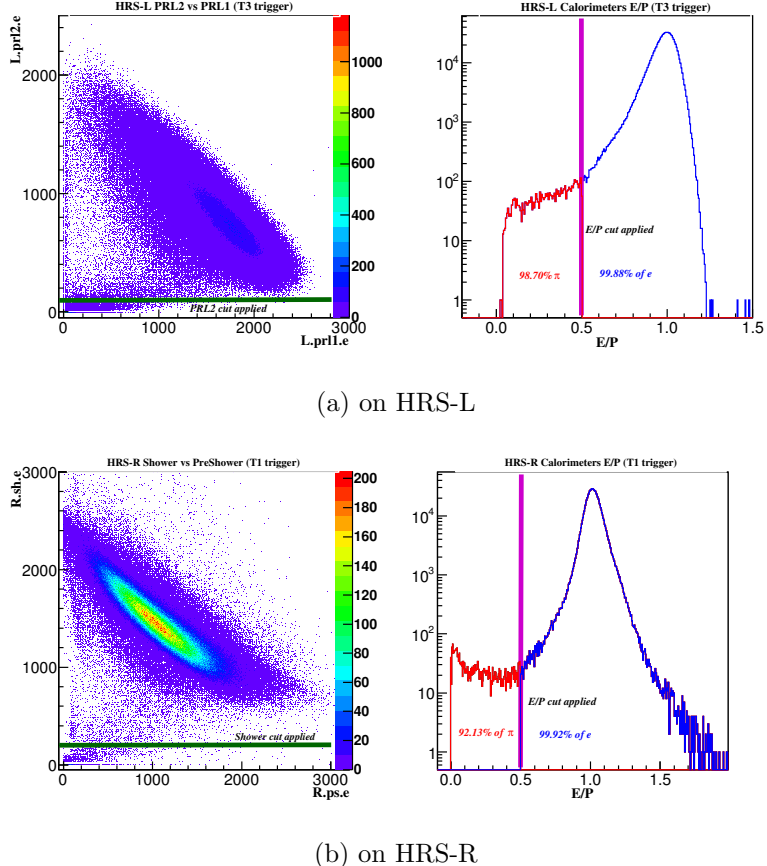


Figure 5.8: PID cut on the calorimeters. Most of pions can be removed by the  $E/P \geq 0.5$  and the cut on the second layer's ADC spectrum ( $PRL2 \geq 100$  or  $SH \geq 200$ ).

## 5.6 Monte Carlo Simulation

The Hall-A Single Arm Monte Carlo simulation tool (SAMC) is designed to simulate the transportation of particles from the target plane to the focal plane. SAMC was originally developed in FORTRAN [62] and then converted into C++ [63]. The electron beam position, the spectrometer settings, and the information of the target system can be specified in the code to match the experimental setting. A simulated event has its specified values of the incoming energy, the scattered momentum and the scattering angle, which are defined in the target coordinate system and called the target plane quantities. These quantities are randomly generated with uniform distributions, and with these quantities as inputs, each focal plane quantity is calcu-

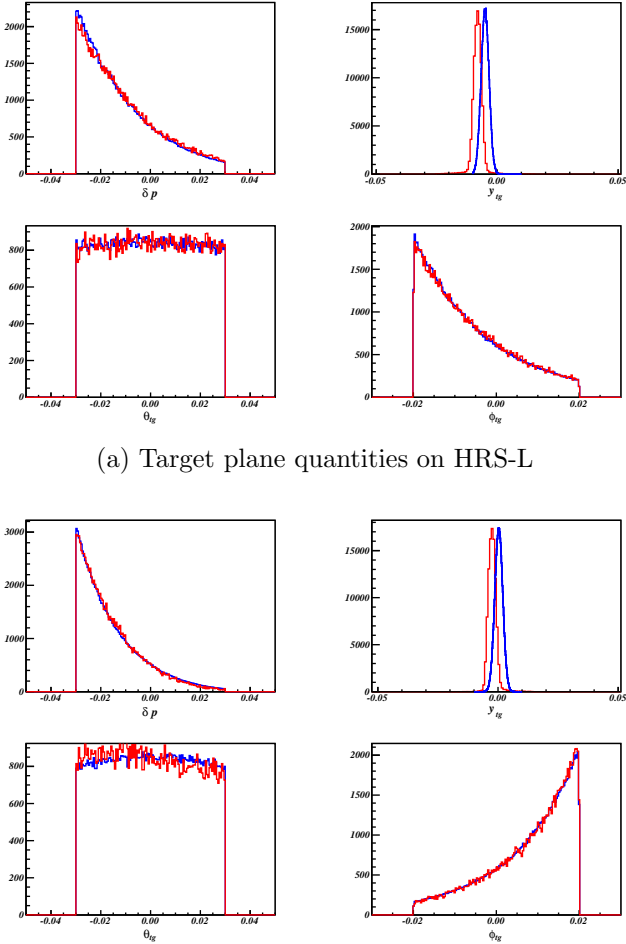
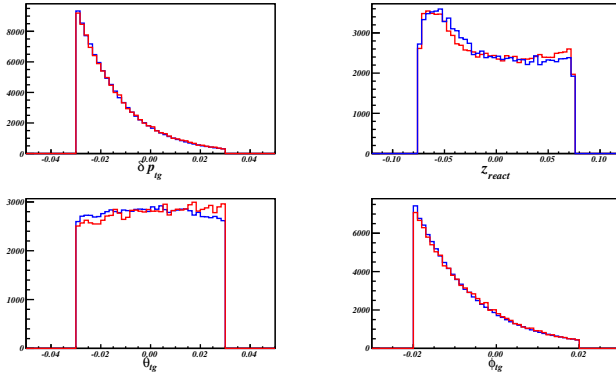
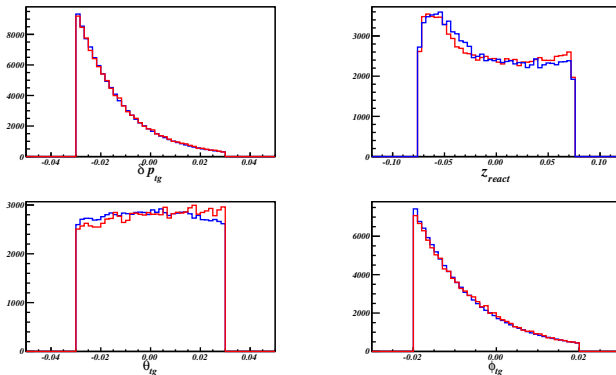


Figure 5.9: Simulation of  $^{12}C$  target plane quantities, where red lines are simulation data from SAMC and blue lines are E08-014 data. The offset of  $y_{tg}$  between two data is a known issue of SAMC but the offset was too small to affect the acceptance.

lated by a set of forward transportation functions which are generated by the SNAKE model [64]. After the focal plane quantities are smeared with the resolution of VDCs, a set of backward transportation functions is used to reconstruct the target plane quantities. During these two processes, events inside and outside the HRS acceptance can be individually identified. Before compared with the experimental data, the distributions of the target plane quantities are weighted by the radiated cross section values of these simulated events which can be calculated using cross section models embedded in the code. In this analysis, a new cross section model and a



(a) Target plane quantities on HRS-L



(b) Target plane quantities on HRS-R

Figure 5.10: Simulation of  ${}^3\text{He}$  target plane quantities, where red lines are simulated data from SAMC and blue lines are the experimental data. The  $z_{\text{react}}$  distribution is given instead of  $y_{\text{tg}}$  to compare the real density distribution which was simulated using the function fitted from data (Appendix D).

special treatment to simulate the no-uniform cryogenic targets have been added in SAMC.

There were 20 million events generated for each target in each kinematic setting. Fig. 5.9 and Fig. 5.10 compare the distribution of reconstructed target plane quantities between simulated data and experimental data for  ${}^{12}\text{C}$  and  ${}^3\text{He}$ , where the histograms for simulation data were weighted by the cross sections calculated by XEMC. The distribution of the same quantity from these two data sets agree nicely with each other. The distribution of  $z_{\text{react}}$  for the cryogenic target was simulated using the relative density distribution function extracted with the method discussed in Appendix D.

## 5.7 Cross Section Model

The inclusive electron scattering cross sections model used in this data analysis is XEMC, a C++ package to compute Born cross sections and radiated cross sections. A brief discussion of the cross section models and radiative correction is given in Appendix B.

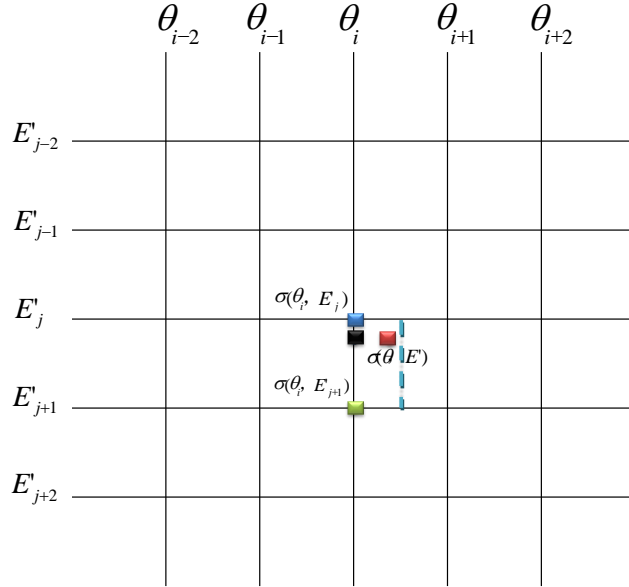


Figure 5.11: A sketch of cross section lookup tables. If  $\theta_i \geq \theta < (\theta_i + \theta_{i+1})/2$ , one sets  $\sigma(\theta, E') \equiv \sigma(\theta_i, E')$ , and vice versa. For  $E'_j < E' < E'_{j+1}$ , the cross section is calculated with the linear relationship given in Eq (5.15).

Calculating radiated cross section using XEMC takes several minutes for each event. To generate millions of simulated events, cross section look-up tables were generated for each target in each kinematic setting. When generating each table, the ranges of scattering angle,  $\Delta\theta$ , and the scattered energy,  $\Delta E'$ , were slightly wider than the real HRS acceptance. Then  $\Delta\theta$  was divided into 200 bins and  $\Delta E'$  was also split into bins of 5 MeV. As shown in Fig. 5.11, the kinematic space for each setting is given as a 2-dimensional lattice where the born cross section and the radiated

cross section for each grid,  $(\theta_i, E'_j)$ , are simultaneously calculated. Since the bin sizes are very fine, for fixed momentum, the cross sections at different angle settings are considered to be equal within one  $\theta$  bin, while for fixed angle, the cross section values are assumed to be proportional to the momentum values inside one  $E'$  bin. As illustrated in Fig. 5.11, for an given event,  $(\theta, E')$ , the value of  $\theta$  is replaced by the closest angle bin, for example,  $\theta_i$ , and then two momentum bins are specified so  $E'_j < E' < E'_{j+1}$ , so the cross section value for this event can be calculated using the linear relationship:

$$\sigma(E', \theta) = \sigma(E'_j, \theta^i) - \frac{E' - E'_j}{E'_{j+1} - E'_j} (\sigma(E'_j, \theta^i) - \sigma(E'_{j+1}, \theta^i)) \quad (5.15)$$

For the same event, the difference between the cross section obtained from the look-up table and the cross section directly calculated from XEMC is less than 0.1%, which indicates that the look-up tables works well. This method can dramatically reduce the computation time when generating simulation events. Tables were re-generated each time when the model is change or the experimental conditions were updated, such as the target thickness.

## 5.8 Event Selection and Corrections

Events are distributed in the entire kinematic space within the acceptance of the HRSSs. However, due to the statistical limitation, the kinematic space is divided by binning one or more kinematic variables, and the cross section is evaluated at the center of each bin with events belong to this bin. The way to choose the acceptance range and the binning method require additional corrections on the cross section. The electron events also have to be correctly selected by applying different cuts.

### 5.8.1 Acceptance Correction

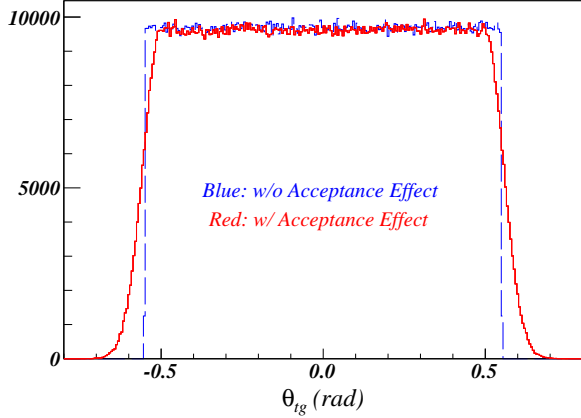


Figure 5.12: A demonstration of the acceptance effect, where the distribution of  $\theta_{tg}$  is generated by assuming no any cross section weighting effect. The blue line shows that the acceptance is flat when the HRS acceptance is perfect, while the red line demonstrates the slowly fall-off of the acceptance edges. Such an effect is mainly due to the geometry of the HRS magnets and also contributed by the resolutions of the VDC tracking and the optics reconstruction. Green lines show the cuts to select the flat acceptance region.

The HRS acceptance includes both the range of momentum dispersion ( $\Delta\delta p$ ) and the total solid angle which is composed of the out-of-plane angle ( $\theta_{tg}$ ) and the in-plane-angle ( $\phi_{tg}$ ). For an extended target, the optics reconstructed reaction point along the beam direction ( $z_{react}$ ) is also affected by the HRS acceptance. These four quantities, called the target plane quantities, are essential to reconstruct the reaction of the electron-scattering at the target. Due to the geometry of the HRS magnets, the event distributions of these quantities are not cut off immediately at the edge of the acceptance but instead, fall off relatively slowly with a gauss tail, as demonstrated in Fig. 5.12. Besides, the resolution of VDC tracking and the accuracy of the optics reconstruction can also smear the distributions of these quantities.

Choosing the right acceptance range of the target plane quantities is crucial in order to obtain the correct cross section results. Tight cuts on the target plane quantities were used to select events at the central region of the HRS acceptance, and the loose cuts on the edges of the focal plane variables can also remove these events

which may have been multi-scattered inside the spectrometer. The acceptance cuts can be generally enlarged to increase the statistics of events in one bin, until the cross section results start to deviate from the results calculated using tighter cuts.

However, good events can be incorrectly discarded when one applies the combination cuts of the four target plane quantities to define a valid acceptance region. Such an effect can be corrected by the HRS simulation for each bin:

$$A(E_0, E_i, \theta_0) = \frac{N_{MC}^{gen}}{\Delta E'_{MC} \Delta \Omega_{MC}} / \frac{N_{MC}^i}{\Delta E'_{bin} \Delta \Omega_{EX}}, \quad (5.16)$$

where  $\Delta E'_{bin}$  is the bin size of  $E'$  and is fixed in both the simulated data and experimental data, and  $\Delta \Omega_{EX}$  is the selected angular acceptance range for the experimental data.  $N_{MC}^i$  is the number of simulation events in the  $i$ th bin, and it has to be applied with the same acceptance cuts as ones on the experimental events ( $N_{EX}^i$ ) in this bin.  $N_{MC}^{gen}$  is the total number of simulated events without any cuts which has been specified when generating these events.  $\Delta E'_{MC}$  and  $\Delta \Omega_{MC}$  define the full momentum and angular acceptance in the simulation, respectively, and they are slightly larger than the HRS acceptance. Overall,  $\frac{N_{MC}^{gen}}{\Delta E'_{MC} \Delta \Omega_{MC}}$  denotes the average number of events in the unit kinematic space which is limited by the HRS geometry, while the other term,  $\frac{N_{MC}^i}{\Delta E'_{bin} \Delta \Omega_{EX}}$ , gives the average number of events in the unit kinematic space without any spectrometer limitations. Eq (5.16) usually refers to the acceptance correction.

### 5.8.2 Central Momentum and Angle

The kinematic space is determined not only by the acceptance of the HRS, but also by the central scattered momentum and the central scattering angle. The central momentum was given by the field values of the HRS magnets which were locked at the setting values by the HRS NMR system during the experiment. The off-line calculation gives the absolute value of the central momentum using the magnetic field

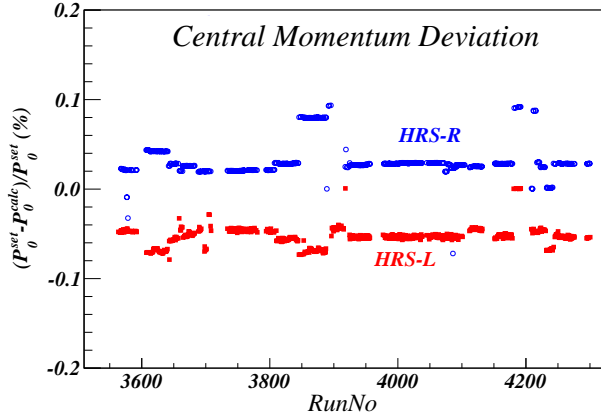


Figure 5.13: Central momentum deviation, where the blue circles and the red boxes are the deviation of the central momentum on HRS-R and HRS-L, respectively. The x-axis is the run number and the y-axis is the deviation in percentage.

of the dipole [42]:

$$P_0 = \sum_{i=0}^4 \gamma_i \cdot (10 \cdot B_{dipole}^{NMR})^i, \quad (5.17)$$

where  $\gamma_{1,2,3,4} = (0, 270.2, 0, -0.0016)$  for HRS-L and  $\gamma_{1,2,3,4} = (0, 269.8, 0, -0.0016)$  for HRS-R.  $B_{dipole}^{NMR}$  is the field reading from the NMR monitor. Fig. 5.13 shows that the actually central momentum values were mostly off by  $\pm 3\%$  while few of them were off by upto  $\pm 10\%$ . During the cross section extraction, the central momenta were assigned to the calculated values instead of the set values.

The central scattering angle was specified during the experiment by moving the HRS to point at the angle marked on the floor. These floor marks were drew with respect to the hall center and may not accurately reflect the true angle values. Moreover, the offsets between the spectrometer center and the hall center are different when the spectrometer points at different angles, which cause the deviation of the actual angles differ at different set angles. For some extreme cases, when the spectrometer is moved away from one angle and later moved back to the same value, the true angles may be different in these two period.

To obtain the actual central scattering angle each time when the spectrometer was

moved, a survey was required to correct the errors of the floor marks and to measure the offset between two centers. Unfortunately, the survey was not proceeded during this experiment and one had to use the survey reports from early experiments which had similar settings. Since the optics target was surveyed at the beginning of this experiment when the HRSs were set at  $25^\circ$ , the actual values of other angle settings were corrected by identifying the difference between the optics target's central foil positions at  $25^\circ$  and at the other angle setting,  $\Delta z_{react}$ , as follow:

$$\theta_{tg} = \frac{D_x + x_{sieve} - y_{beam}}{L - x_{beam} \cdot \sin\theta_0^{set} - \Delta z_{react} \cdot \cos\theta_0^{set}}, \quad (5.18)$$

$$\phi_{tg} = \frac{D_y + y_{sieve} - x_{beam} \cdot \cos\theta_0^{set} + \Delta z_{react} \cdot \sin\theta_0^{set}}{L - x_{beam} \cdot \sin\theta_0^{set} - \Delta z_{react} \cdot \cos\theta_0^{set}}, \quad (5.19)$$

$$\theta_0^{true} = \arccos \left( \frac{\cos\theta_0^{set} - \phi_{tg} \sin\theta_0^{set}}{\sqrt{1 + \theta_{tg}^2 + \phi_{tg}^2}} \right), \quad (5.20)$$

where  $D_x$ ,  $D_y$ ,  $x_{sieve}$ ,  $y_{sieve}$  and  $L$  are given in Table 4.1 and Table 4.2. The beam position ( $x_{beam}$ ,  $y_{beam}$ ) was locked at (-2.668 mm, 3.022 mm) during the experiment.  $\theta_0^{set}$  is the central scattering reading from the floor marks and  $\theta_0^{true}$  is the actual central scattering angle after the correction. As shown in Table ??, the calculation showed that the maximum offset between  $\theta_0^{true}$  and  $\theta_0^{set}$  was not larger than  $0.04^\circ$ . The value of  $\theta_0^{true}$  was calculated for runs taken at each run period when the spectrometer was moved to different positions. The cross sections were calculated with these updated values.

### 5.8.3 Binning Correction

The cross section results are calculated by binning the data on  $E'$ . The range and step size of binning is given in the following table:

From Eq (5.1), when binning on  $E'$ , the cross section in each bin is given as a function of the central scattering angle ( $\theta_0$ ) and the momentum value at the center

RunNo	$\theta_0^{set}(L)$	$\theta_0^{true}(L)$	$\theta_0^{set}(R)$	$\theta_0^{true}(R)$
3565~3656	25.00	25.00	25.00	25.00
3657~3683	21.00	21.03	21.00	21.04
3684~3708	23.00	23.00	23.00	23.01
3735~3891	25.00	24.99	25.00	25.00
3892~3916	—	—	21.00	21.03
3917~4071	28.00	27.98	28.00	27.99
4073~4103	21.00	21.04	28.00	27.99
4112~4179	23.00	23.00	23.00	23.04
4181~4241	25.00	24.98	25.00	25.00
4242~4250	21.00	21.02	21.00	21.03
4251~4299	28.00	27.98	28.00	27.99

Table 5.2:  $E'$  binning size and range

Kin	3.1	3.2	4.1	4.2	5.0	5.05	5.1	5.2	6.5
$E'^{Min}$	2.76	2.90	2.71	2.88	2.38	2.52	2.66	2.85	2.70
$E'^{Max}$	3.05	3.21	3.00	3.19	2.63	2.78	2.94	3.14	2.99
$\Delta E'$	0.01	0.01	0.01	0.01	0.01	0.01	0.01	0.01	0.01

Table 5.3:  $E'$  binning size and range

of the bin ( $E'_i$ ). However, events in each bin carry different momenta varying from  $E'_i - \frac{1}{2}\Delta E'$  to  $E'_i + \frac{1}{2}\Delta E'$ , while their central scattering angles can deviate from  $\theta_0$  within the solid angle,  $\Delta\Omega_{EX}$ . To correct the effect, a **bin-centering correction** is calculated using the simulation data and the cross section model:

$$B(E_0, E_i, \theta_0) = \frac{\sigma_{XEMC}^{rad}(E_0, E'_i, \theta_0)}{\sum_{j \in i} \sigma_{XEMC}^{rad}(E_0, E'_j, \theta_j)}, \quad (5.21)$$

where  $\sum_{j \in i}$  means summation over the radiated cross section values,  $\sigma(E'_j, \theta_j)$ , of all Monte Carlo events in the  $i$ th  $x_{bj}$  bin.  $\sigma_{XEMC}^{rad}(E'_i, \theta_0)$  and  $\sigma_{XEMC}^{rad}(E'_j, \theta_j)$  are calculated from the XEMC model.

#### 5.8.4 Cuts

In addition to cutting on the binning variable, there are several other cuts which were applied to select good scattered electron events/ For example, in HRS-L:

1. Cut on production trigger events (see Appendix A),  $DBB.evtypebits >> 3 \& 1$  (”3” is replaced by ”1” for HRS-R);
2. Remove pulser events generated by EDTM modules,  $DBB.edptl[0] == 0$ ;
3. Beam trip cut,  $left\_current >= I_{trip}$ ;
4. Select events with only one track in VDCs,  $L.tr.n == 1$ ;
5. Cuts on the focal plane acceptance,  $|x_{fp}| <= 0.75 \&\& |y_{fp}| <= 0.55 \&\& |\theta_{fp}| <= 0.15 \&\& |\phi_{fp}| <= 0.045$ ;
6. Cuts on the target plane acceptance,  $|\delta p_{tg}| <= 0.03 \&\& |ReactPointZ| <= 0.07 \&\& |\theta_{tg}| <= 0.03 \&\& |\phi_{tg}| <= 0.02$ ;
7. PID cuts on the GC and the calorimeter,  $L.cer.asum\_c >= 50 \&\& epL <= 0.5 \&\& L.prL2.e <= 100$ , where  $epL$  denotes the energy sum of the calorimeter divided by the central momentum (E/P).

For a list of runs, the total number of events after the cuts defined above is given by:

$$N_{EX}^i = \sum_r \frac{PS1(3)^r \cdot N_{T_{1(3)}}^r}{LT_{T_{1(3)}}^r}, \quad (5.22)$$

where  $r$  represents one of runs in the list and  $N_{T_{1(3)}}^r$  is the total number of events from  $T_1$  on HRS-R ( $T_3$  on HRS-L) and recorded by DAQ after cutting out beam trip. Notes that events from each run are individually corrected by the Live-Time ( $LT_{T_{1(3)}}^r$ ) before they are added together.

## 5.9 From Yields to Cross Sections

The experimental Born cross section can be calculated from Eq (5.1) after applying the acceptance correction (Eq (5.16)) and the bin-centering correction (Eq (5.21)):

$$\sigma_{EX}^{Born}(E'_i, \theta_0) = A(E'_i, \theta_0) \cdot B(E'_i, \theta_0) \cdot \sigma_{EX}^{rad}(E'_i, \theta_0) \cdot RC(E'_i, \theta_0) \quad (5.23)$$

Note that the initial electron energy,  $E_0$ , is fixed at 3.356 GeV during this experiment so it is omitted from the equation. The last term is the radiation correction factor:

$$RC(E'_i, \theta_0) = \frac{\sigma_{XEMC}^{Born}(E'_i, \theta_0)}{\sigma_{XEMC}^{rad}(E'_i, \theta_0)}. \quad (5.24)$$

Extraction of cross sections from Eq 5.23 largely relies on the performance of the simulation and the cross section model, which, however, can not be directly examined from the cross section results. Two useful quantities, the experimental yield and the Monte Carlo (MC) yield, can be extracted to directly compare their difference. The experimental yield can be written as:

$$Y_{EX}^i = \frac{N_{EX}^i}{N_e \cdot \epsilon_{eff}}, \quad (5.25)$$

where  $\epsilon_{eff} = \epsilon_{trig} \cdot \epsilon_{vdc} \cdot \epsilon_{e\_cut}^{GC} \cdot \epsilon_{e\_cut}^{calo}$  which are given in Eq. (5.11), Eq. (5.12) and , respectively. The MC yield is given by:

$$Y_{MC}^i = N_{tg} \cdot \sum_{j \in i} \sigma_{model}^{rad}(E'_j, \theta_j) \cdot \frac{\Delta\Omega_{MC} \Delta E'_{MC}}{N_{MC}^{gen}}. \quad (5.26)$$

The ratio of the experimental yield to the MC yield should be close to one if the performance of the HRS can be well simulated by the MC data and the XEMC model produces cross sections relatively close to the real results. The experimental

Born cross section from Eq 5.23 can be rewritten as:

$$\sigma_{EX}^{Born}(E'_i, \theta_0) = \frac{Y_{EX}^i}{Y_{MC}^i} \cdot \sigma_{XEMC}^{Born}(E'_i, \theta_0), \quad (5.27)$$

The yield ratio method can largely reduce the bias caused by the choice of different cross section models. While the experimental yield is completely extracted from the data and remains unchanged, one can iterate the cross section model and apply necessary corrections only on the MC yield until the the yield ratio becomes close to one for different  $E'$  bins. Furthermore, the acceptance cuts on the HRS can also be studied by varying the cuts and checking the distribution of the yield ratio as a function of the binning variable. Most of other potential issues, such as bad data, incorrect input parameters and so on, can also be examined in the yield ratio method.

## 5.10 Calculation of Errors

One of most important tasks to extract experimental cross sections is to calculate the errors which includes both systematic errors and the statistical errors. Systematic errors are introduced by the experimental instrumentation, the simulation tool and the cross section model, etc. Statistical errors relate to the number of measurements on one quantity during the experiment. It is very important to properly propagate the errors when extracting new quantities from the existing quantities and any mistakes such as mis-counting or multi-counting should be avoided during the cross section extraction. The detailed explanation of the error calculation and propagation is given as follows.

### 5.10.1 Statistical Errors

The detail propagation of Statistical Errors is discussed bellow:

1.  $N_e$ : From Eq.5.4, since the charge is obtained from the average of two BCM monitor outputs ( $U_1$  and  $D_1$ ), the error is also averaged:

$$\delta N_e^r = \sqrt{\frac{(\delta N_e^{r,D_1})^2 + (\delta N_e^{r,U_1})^2}{2}} = \sqrt{\frac{N_e^{r,D_1} + N_e^{r,U_1}}{2}} = \sqrt{\frac{N_e^r}{2}}, \quad (5.28)$$

where,  $r$  means the run number. Hence,

$$\delta N_e = \sqrt{\sum_r (\delta N_e^r)^2} = \sqrt{\frac{\sum_r N_e^r}{2}} = \sqrt{\frac{N_e}{2}}. \quad (5.29)$$

2. **Live-Time**: Form Eq.5.6, when  $PS^r = 1$ :

$$\delta LT^r = LT^r \cdot \sqrt{\frac{1}{N_{r,Scaler}} + \frac{1}{N_{r,DAQ}}}, \quad (5.30)$$

where  $PS = PS1$  for HRS-R and  $PS = PS3$  for HRS-L. When  $PS^r > 1$ , the calculation of  $\delta LT^r$  is given differently [65]:

$$\delta LT^r = LT^r \cdot \sqrt{\frac{1}{N_{r,Scaler}} - \frac{1}{N_{r,DAQ}}}. \quad (5.31)$$

3.  $N_{EX}$ : From Eq.5.22 and  $N_{EX} = \sum_r N_{EX}^r$  for all runs, we have:

$$\delta N_{EX}^r = N_{EX}^r \cdot \sqrt{\frac{1}{N_{recorded}^r} + \left(\frac{\delta LT^r}{LT^r}\right)^2}, \quad \delta N_{EX} = \sqrt{\sum_r (\delta N_{EX}^r)^2}, \quad (5.32)$$

where  $N_{recorded}^r$  is defined in Eq (5.6).

4.  $Y_{EX}$ : From Eq.5.25,

$$\delta Y_{EX} = Y_{EX} \cdot \sqrt{\left(\frac{\delta N_{EX}}{N_{EX}}\right)^2 + \left(\frac{\delta N_e}{N_e}\right)^2 + \left(\frac{\delta \epsilon_{eff}}{\epsilon_{eff}}\right)^2}, \quad (5.33)$$

where  $\epsilon_{eff}$  is set to one and its statistic error and systematic error are set to zero and 1%, respectively.

5.  $Y_{MC}$  : From Eq.5.26,

$$\delta Y_{MC} = Y_{MC} \cdot \sqrt{\left(\frac{\delta \sum_{j \in i}}{\sum_{j \in i}}\right)^2 + \left(\frac{\delta N_{MC}^{gen}}{N_{MC}^{gen}}\right)^2}, \quad (5.34)$$

where  $\delta \sum_{j \in i} = \sum_{j \in i} \cdot \frac{1}{\sqrt{N_{MC}^i}}$ , since it is summarizing the cross section values of MC events ( $N_{MC}^i$ ) in one bin.

6.  $\sigma_{EX}^{Born}$  : From Eq.5.27,

$$\delta \sigma_{EX}^{Born} = \sigma_{EX}^{Born} \cdot \sqrt{\left(\frac{\delta Y_{EX}}{Y_{EX}}\right)^2 + \left(\frac{\delta Y_{MC}}{Y_{MC}}\right)^2} \quad (5.35)$$

### 5.10.2 Systematic Errors

The entire list of systematic errors has not been determined in this thesis. Few items are given as follows:

1.  $N_{tg}$ : Form Eq (5.7) and Eq (5.8), there are three terms that can introduce errors: beam current measurement and calculation ( $\delta I$ ), accuracy of Boiling Factors ( $\delta B$ ), and the accuracy of target thickness measurement ( $\delta \rho$ ). First two terms were temporarily set to zero. Hence:

$$\delta N_{tg} = \frac{\delta \rho}{\rho} \cdot N_{tg} \quad (5.36)$$

2.  $N_{efficiency}$ : 1% systematic errors is assigned to each of VDC One-Track efficiency, trigger efficiency, detection and cut efficiencies of Gas Cherenkov and Calorimeters.

3.  **$\delta p$  correction (HRS-R only):** The error caused by correcting the un-calibrated  $\delta p$  on HRS-R as given in Appendix D has to be evaluated. 0.3% is assigned in this thesis. The value will be updated afterwards.
4. **Cross section model and radiative correction:** The error from the cross section models and the radiative correction. An estimation of 3% is given in this thesis. The value will be updated afterwards.

# Chapter 6

## Results

In this chapter, the preliminary results of cross sections, momentum distribution and cross section ratios will be presented. The error bars shown in this chapter are calculated based on the discussion given in previous chapter, and include statistical errors and parts of systematic errors, such as detector efficiencies, target thickness uncertainty and electron charge uncertainty. Systematic uncertainties coming from Monte Carlo simulation and cross section errors will be included in the final results.

### 6.1 Yields

### 6.2 Cross Sections

The measured born cross sections for  $^2H$ ,  $^3He$ ,  $^4He$ ,  $^{12}C$ ,  $^{40}Ca$ , and  $^{48}Ca$  are showed in Fig. 6.1 through Fig. 6.6, respectively. The detailed kinematic settings of two HRSs and list of targets measured are given in Table 6.1 and Table 6.2. For each setting, if data are available from both arms, the cross section values are given as the average of individual cross sections extracted from both arm.

Fig. 6.1 shows the cross section of  $^2H$ , where the Quasi-Elastic peak can be clearly identified at  $x_{bj} = 1$  due to the relatively small Fermi motion of nucleons in the target.

Name	$\theta_0(^o)$	$P_0$ ( $GeV/c$ )	$Q^2$ ( $GeV^2$ )	Target
Kin3.1	21	2.905	1.295	$^2H, ^3He, ^4He, ^{12}C, ^{40}Ca, ^{48}Ca$
Kin3.2	21	3.055	1.362	$^3He, ^4He, ^{12}C,$
Kin4.1	23	2.855	1.523	$^3He, ^{12}C, ^{40}Ca, ^{48}Ca$
Kin4.2	23	3.035	1.619	$^3He, ^4He, ^{12}C, ^{40}Ca, ^{48}Ca$
Kin5.0	25	2.505	1.575	$^3He, ^4He, ^{12}C, ^{40}Ca, ^{48}Ca$
Kin5.05	25	2.650	1.667	$^3He, ^{12}C, ^{40}Ca, ^{48}Ca$
Kin5.1	25	2.795	1.758	$^2H, ^3He, ^4He, ^{12}C, ^{40}Ca, ^{48}Ca$
Kin5.2	25	2.995	1.883	$^2H, ^3He, ^4He, ^{12}C$
Kin6.5	28	2.845	2.235	$^3He, ^{12}C,$

Table 6.1: List of Kinematic settings and targets measured on HRS-L

Name	$\theta_0(^o)$	$P_0$ ( $GeV/c$ )	$Q^2$ ( $GeV^2$ )	Target
Kin3.1	21	2.905	1.295	$^2H, ^4He, ^{12}C, ^{40}Ca, ^{48}Ca$
Kin3.2	21	3.055	1.362	$^3He, ^4He, ^{12}C, ^{40}Ca, ^{48}Ca$
Kin4.1	23	2.855	1.523	$^3He, ^{12}C, ^{40}Ca, ^{48}Ca$
Kin4.2	23	3.035	1.619	$^3He, ^4He, ^{12}C, ^{40}Ca, ^{48}Ca$
Kin5.0	25	2.505	1.575	$^3He, ^4He, ^{12}C, ^{40}Ca, ^{48}Ca$
Kin5.05	25	2.650	1.667	
Kin5.1	25	2.795	1.758	$^2H, ^3He, ^4He, ^{12}C, ^{40}Ca, ^{48}Ca$
Kin5.2	25	2.995	1.883	$^2H, ^3He, ^4He, ^{12}C$
Kin6.5	28	2.845	2.235	$^3He, ^{12}C,$

Table 6.2: List of Kinematic settings and target measured on HRS-R

The results shows good agreement with the calculation from XEMC model.  $^4He$  and  $^{12}C$  agree nicely with the model prediction (Fig. 6.3 and Fig. 6.4). For  $^3He$  target, additional works are required on the XEMC model to correct the rapidly decreasing of cross section values when  $x_{bj} \rightarrow 3$ . Cross sections of  $^{40}Ca$  and  $^{48}Ca$  are firstly available in high  $Q^2$  ( $> 1 GeV^2$ ) from this experiment and more iterations of the cross section models are necessary until the model and the data have stable agreement.

### 6.3 Momentum Distribution

### 6.4 SRC Ratio

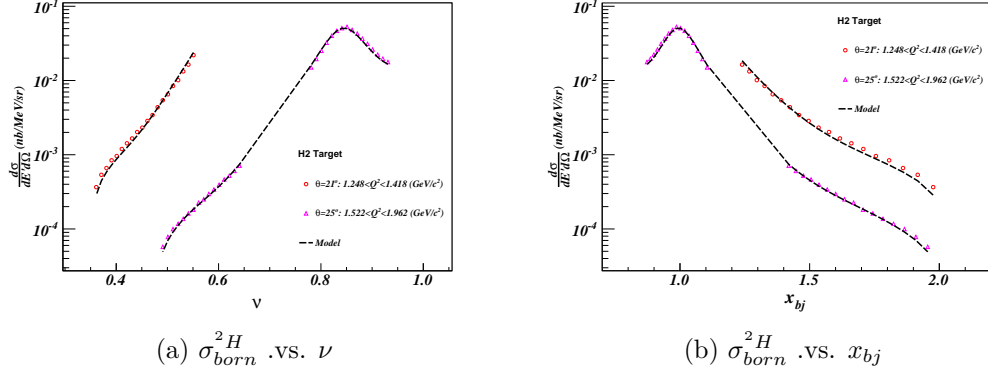


Figure 6.1:  $^2H$  Born Cross Sections, where dots are from experimental results and lines are calculated from XEMC model

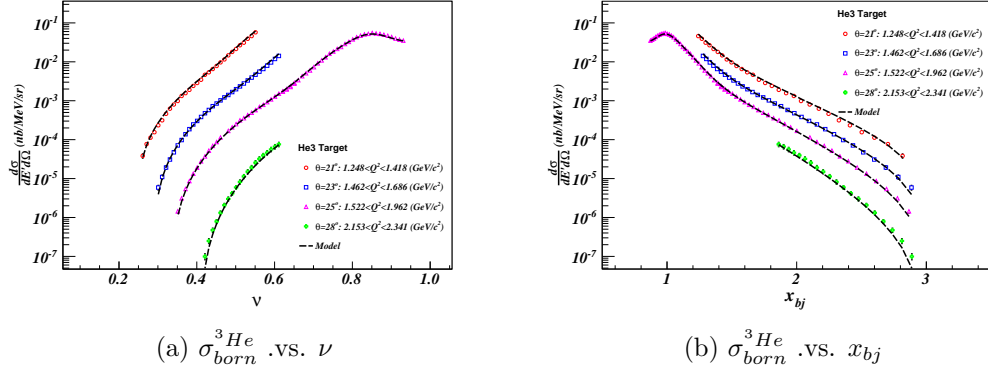


Figure 6.2:  $^3He$  Born Cross Sections, where dots are from experimental results and lines are calculated from XEMC model

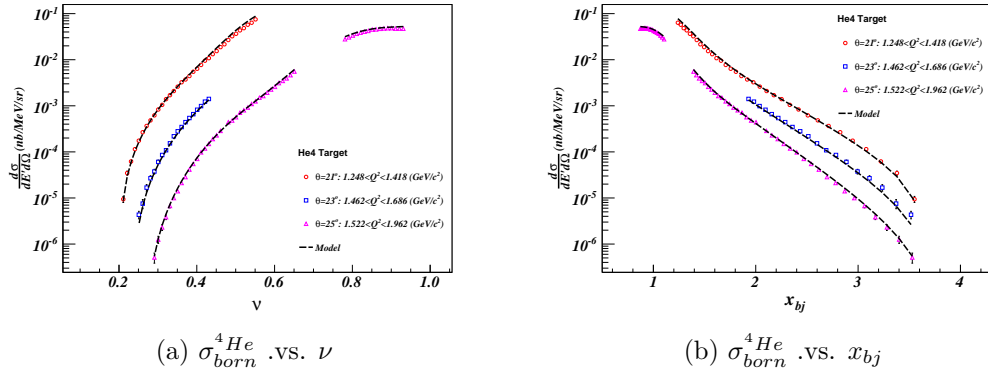


Figure 6.3:  $^4He$  Born Cross Sections, where dots are from experimental results and lines are calculated from XEMC model

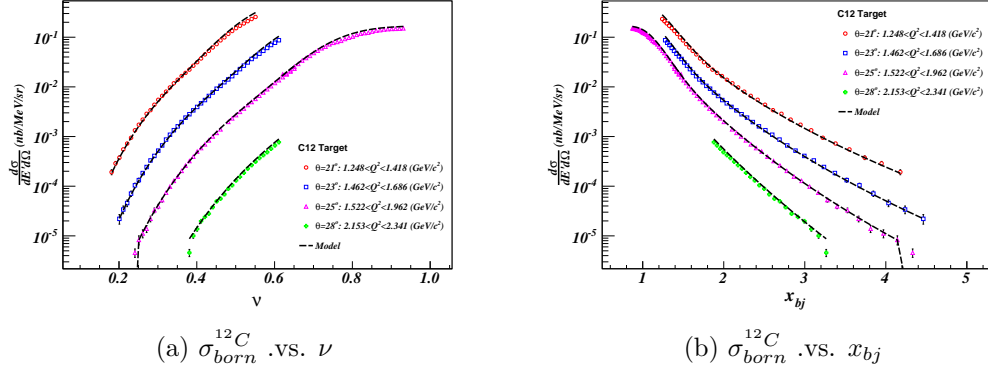


Figure 6.4:  $^{12}C$  Born Cross Sections, where dots are from experimental results and lines are calculated from XEMC model

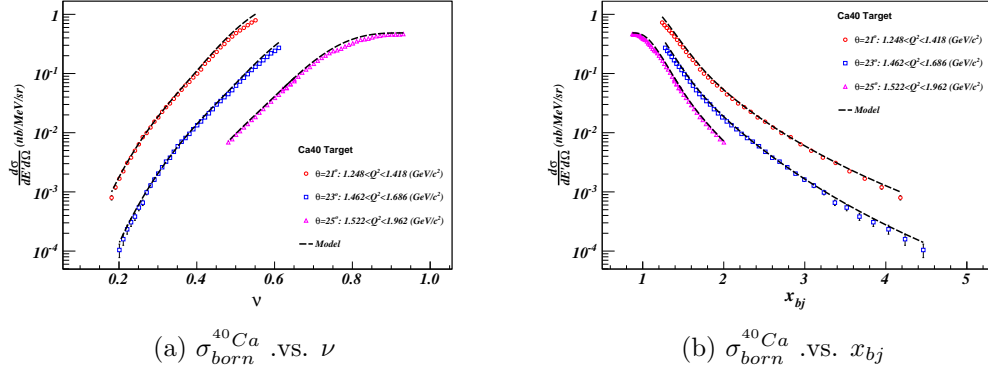


Figure 6.5:  $^{40}Ca$  Born Cross Sections, where dots are from experimental results and lines are calculated from XEMC model

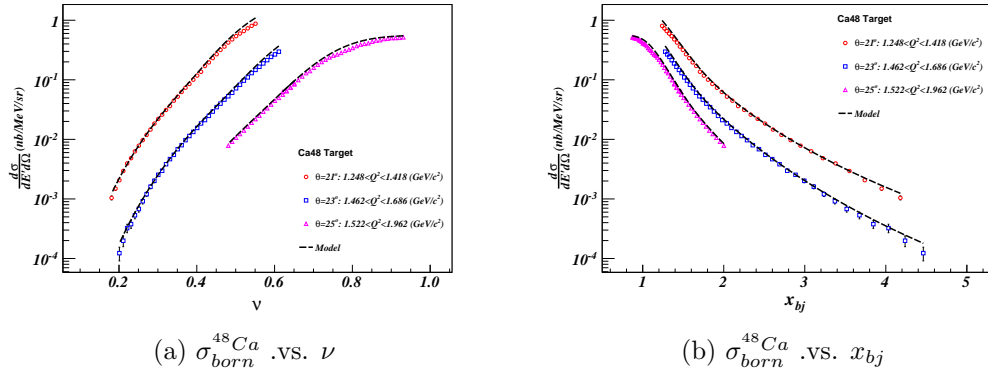


Figure 6.6:  $^{48}Ca$  Born Cross Sections, where dots are from experimental results and lines are calculated from XEMC model

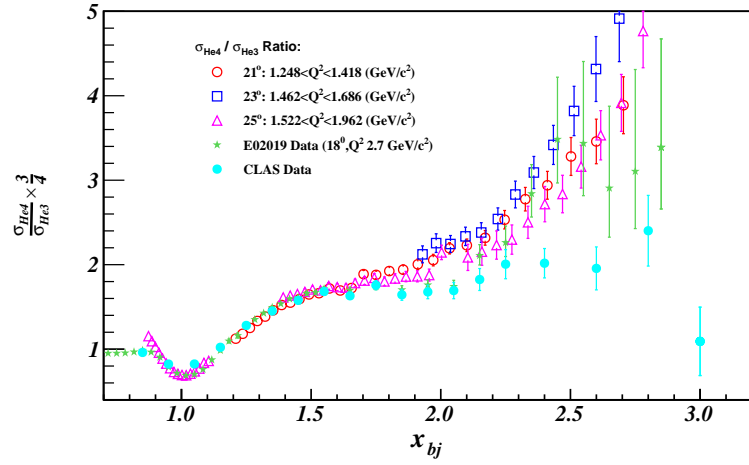


Figure 6.7: Cross Section Ratio of  $^4\text{He}$  to  $^3\text{He}$ , where the ratio results from E02-019 data and CLAS data are also included from comparison.

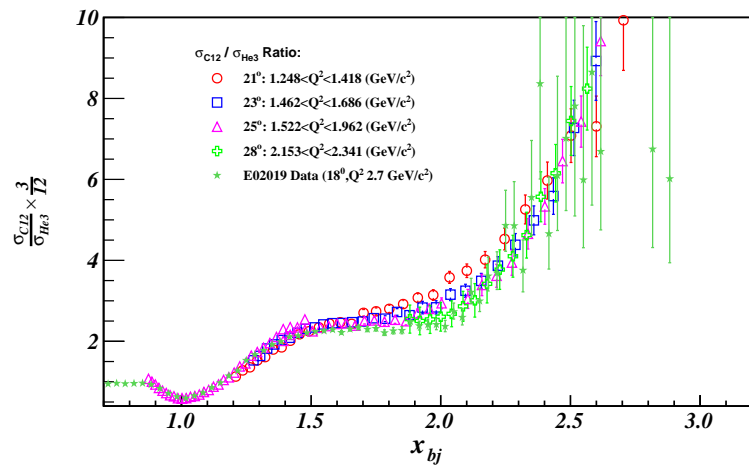


Figure 6.8: Cross Section Ratio of  $^{12}\text{C}$  to  $^3\text{He}$ , comparing with E02-019 results.

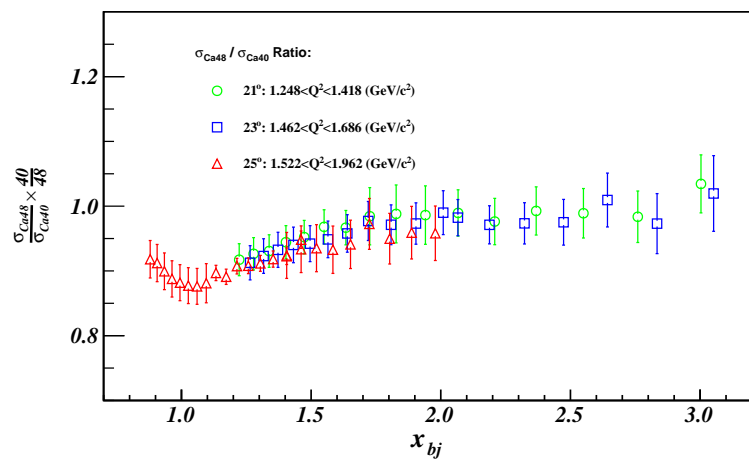


Figure 6.9: Cross Section Ratio of  $^{48}\text{Ca}$  to  $^{40}\text{Ca}$

## Appendix A

### Triggers in Data Analysis

When an scattered electron goes through the detectors located in the detector hut of each High Resolution Spectrometers (HRS), the signals created in certain detectors form different triggers based on the design of the trigger system. The traditional single arm trigger, T1 for HRS-R or T3 for HRS-L, requires both S1 and S2m scintillator planes fired in a narrow overlap time window. During E08-014 experiment, the gas Cerenkov detector (GC) was also added to the main trigger to exclude most of pions events, which dramatically reduced the total event rate and the dead-time. The new main triggers were the coincidence of logic signals from S1, S2m and GC. The original triggers were still used for the PID study but were assigned with different names, T6 for HRS-R and T7 for HRS-L, respectively.

Two other triggers, T2 for HRS-R and T4 for HRS-L, are designed for the trigger efficiency study. T2 (T4) requires only one of S1 and S2m logic signals coinciding with the logic signal from a third detector plane, such as the GC in this experiment. T2 and T4 triggers are generated by sending logic signals from S1, S2m and Cerenkov into a programmable module, called MLU <sup>1</sup>.

Ideally, before the pre-scaling, T6 (T7) should be exactly the same as T1 (T3), if the GC has 100% of detection efficiency and the electron signal has very clean back-

---

<sup>1</sup>For more detail about Hall A trigger design, visit [http://hallaweb.jlab.org/equipment/daqtriggersetup\\_2003.html](http://hallaweb.jlab.org/equipment/daqtriggersetup_2003.html)

ground. However, T6 (T7) has much higher event rates than T1 (T3) mainly because of the pion contamination. During the process of data taking, T1 and T3 were the major production triggers, the rates of which were kept as high as possible till the dead time became high. T3, T4, T6 and T7 were prescaled to fix their rates no more than  $50 \sim 100$ Hz. T5 is the coincident trigger of T1 and T3, which was not used in this experiment. T8 is the signal from the CPU clock. Other trigger types can be defined in different experiments which requires additional devices.

Trigger:	T1	T2	T3	T4	T5	T6	T7	T8
TDC Channel:	1	2	3	4	5	6	7	8
Decimal:	$2$	$2^2$	$2^3$	$2^4$	$2^5$	$2^6$	$2^7$	$2^8$
Hex:	0x02	0x04	0x08	0x10	0x20	0x40	0x80	0x100

Table A.1: Triggers and their corresponding data types in data stream

All these trigger signals are sent to a 16-channel TDC port. Signals produced by an events can generate several types of triggers in a very narrow time window. Once one of the triggers is accepted by the DAQ system, all of the event's signals from detectors and other instruments are recorded by TDCs and ADCs. The trigger signals associated with this event are also stored. The analyzer decodes the TDC values of these triggers as Hex format and issues these values into a pointer-like variable in the **T** tree, "DBB.evtypebits". Table A.1 lists the triggers and their corresponding values in different digital types.

Based on this table, events belonged to the same trigger can be identified by applying cuts on the trigger variable. Note that an event can be affiliated with more than one trigger types. There are several kinds of trigger cuts used during data analysis, the difference in between which is listed below:

1. **DBB.evtypebits=0x02:**

Cuting only T1 trigger and no other trigger types co-exist.

2. **(DBB.evtypebits&0x02)==0x02:**

Cutting T1 trigger but don't care whether other trigger types co-exist or not.

### 3. DBB.evtypebits $\gg$ 1&1:

The same as (2).

### 4. DBB.evtypebits &(1 $\gg$ 1):

Exactly the same as (2) and (3), but returning a value of "2" instead of "1" (all non-zero values mean "TRUE")

*The following two trigger cuts are not recommended:*

### 5. DBB.evtype==1:

Select events only triggered by T1, and no other trigger present within 5 ms window when the TS registers an event. This is almost the same as (1) but there is a slight difference and the reason is unknown.

### 6. fEvtHdr.fEvtType==1:

Exactly the same as (5)

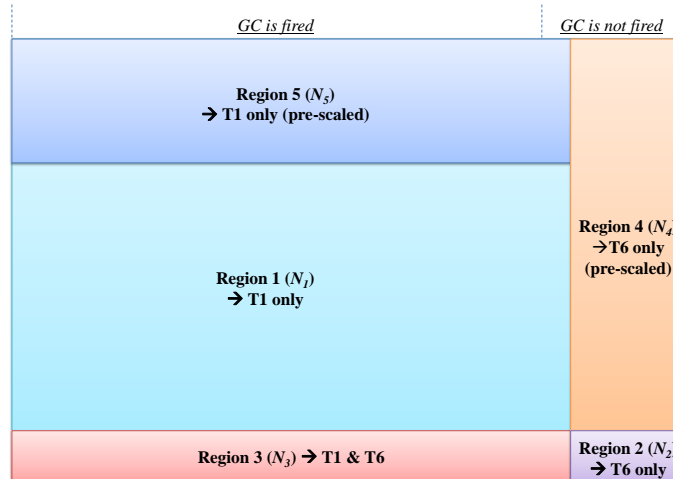


Figure A.1: A scheme of events with different Trigger cuts. Each box denotes the number of events associated with certain trigger types. The size of each box does not necessarily reflect the real distribution of events in the data.

Not all events created by the scattered electrons can be recorded by the DAQ system because the detectors do not have 100% detection efficiencies and a certain portion of detected events are skipped due to the pre-scaling. For each run, the pre-scale factors for different trigger types are recorded in the raw data as well as in the log files created at the start and at the end of each run. The total number of events from a trigger has to be corrected by the efficiency of the trigger system (i.e. the trigger efficiency) including the electronic, the computer and the detectors (S1, S2m and GC for E08014). The procedure to extract the trigger efficiency has been discussed in Section 5.5.1. In the rest of this section, all variables related to the number of events are assumed to have been corrected by the trigger efficiency.

Assuming the total number of the scattered electrons which fire both S1 and S2m on HRS-R is given as the big box in Fig. A.1, the area of each small box represents the number of electrons (events) associated with different trigger types after applying the pre-scale factors. Region 1 gives the number of events ( $N_1$ ) from T1 only, and region 2 gives the total number of event ( $N_2$ ) from T6 only. Region 3 represents the events associated with both T1 and T6 ( $N_3$ ). The portions of events which are not recorded due to the pre-scaling are given as  $N_4$  in Region 4 for T6 and  $N_5$  in Region 5 for T1, respectively.  $N_2 + N_4$  denotes the number of events which are not detected by the GC, and the value should be small since the GC has very high detection efficiency. So the relationship between the number of events in those regions and the pre-scale factors can given as:

$$PS1 = \frac{N_1 + N_3 + N_5}{N_1 + N_3}, PS6 = \frac{N_1 + N_2 + N_3 + N_4 + N_5}{N_2 + N_3} = \frac{N_2 + N_4}{N_2}, \quad (A.1)$$

where  $N_1$ ,  $N_2$  and  $N_3$  can be extracted from data by applying Trigger cuts:

If the pre-scale factors are known, the total number of trigger events in the box

Events	Cut
$N_1$	<b>DBB.evtypebits &gt;&gt; 1&amp;1&amp;&amp;!(DBB.evtypebits &gt;&gt; 6&amp;1)</b>
$N_2$	<b>DBB.evtypebits &gt;&gt; 6&amp;1&amp;&amp;!(DBB.evtypebits &gt;&gt; 1&amp;1)</b>
$N_3$	<b>DBB.evtypebits &gt;&gt; 1&amp;1&amp;&amp;DBB.evtypebits &gt;&gt; 6&amp;1</b>
$N_1 + N_3$	<b>DBB.evtypebits &gt;&gt; 1&amp;1</b>
$N_2 + N_3$	<b>DBB.evtypebits &gt;&gt; 6&amp;1</b>

Table A.2: Events types with different Trigger cuts

can be mathematically calculated:

$$N_0 = N_1 + N_2 + N_3 + N_4 + N_5 = PS6 \times (N_2 + N_3). \quad (\text{A.2})$$

However, since T6 was assigned with big pre-scale factor to keep the trigger rate as low as 50Hz, the value of  $N_2 + N_3$  should be very small and the statistical error of  $N_0$  would be very large. Instead,  $N_1$  has much more statistics since T1 was maintained to have big trigger rate. Combined with  $N_4$  and  $N_5$ , it gives the total number of electrons in that box as:

$$N_0 = N_1 + N_2 + N_3 + N_4 + N_5 = PS1 \times (N_1 + N_3) + PS6 \times N_2. \quad (\text{A.3})$$

where the term,  $PS1 \times (N_1 + N_3)$ , denotes the number of events which fired the GC, while  $PS6 \times N_2$  is the number of electrons which did not fire the detector.

Eq A.3 can be further simplified. From Fig. A.2, a new region, called Region 4' ( $N_{4'}$ ), can be defined:

$$\frac{N_{4'}}{N_1} = \frac{N_2}{N_3} = \frac{N_2 + N_4}{N_1 + N_3 + N_5}, \quad (\text{A.4})$$

which gives:

$$N_2 + N_{4'} = PS6 \times N_2 = PS1 \times (N_2 + N_{4'}) = PS1 \times (N_2 + N_1 N_2 / N_3). \quad (\text{A.5})$$

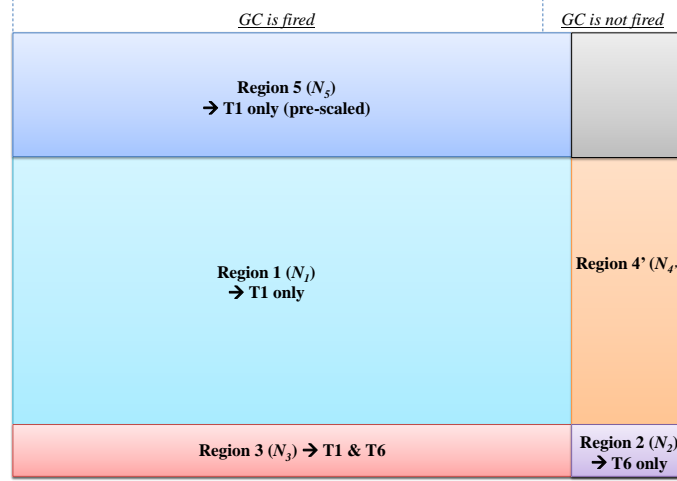


Figure A.2: Another scheme of electrons with different Trigger cuts

and the relationship between PS1 and PS6 can be given by:

$$PS6 = PS1(1 + N_1/N_3). \quad (A.6)$$

So PS6 can be substituted by the formula above, and Eq A.3 becomes:

$$N_0 = PS1 \times (N_1 + N_3) \times \frac{N_2 + N_3}{N_3} = \frac{PS1 \times (N_1 + N_3)}{\epsilon}, \quad (A.7)$$

where  $\epsilon = \frac{N_3}{N_2 + N_3}$  is the percentage of electrons firing GC when they pass through the detector, i.e., the exact definition of the GC detection efficiency. Since the number of events from T6 is very small, to reduce the statistical error, the typical way to get the detection efficiency of the GC is to select good electron samples from T1 events by applying a tight cut on the calorimeter and calculating how many of them are detected by the GC (see Section 5.x.x):

$$\epsilon_{det}^{GC} = \frac{N^{GC}}{N^{Sample\_from\_Calo}}. \quad (A.8)$$

$N_0$  now becomes straightforward: the total number of electrons passing through

the HRS detectors is equal to the number of events triggered by S1, S2m and GC and corrected by the detection efficiency of the GC. It is important to emphasize that the value of  $N_0$  has to also be corrected by the trigger efficiency.

The total number of trigger events from T3 on HRS-L can also be given in the same way.

## Appendix B

# XEMC: A Package for Inclusive Cross Section Models

### B.1 Overview

XEMC is a stand-alone package written in C++ to calculate the inclusive cross section of electron-nucleus scattering. It is composed of three cross section models for the inelastic (DIS) process, three cross section models for the quasi-elastic (QE) process, and a radiative correction (RC) subroutine based on the peak approximation. The parameters of kinematic settings and target configurations are all defined in an external file.

Cross section models are usually developed based on theoretical calculations, world data fittings and any additional corrections. Different models are applied on the specific kinematic region, depending on the physics processes and the final states. The inclusive cross section measured by E08-014 was above the QE peak and can be well modelled by the y-Scaling [8,11–13]. The QE model was further iterated by using experimental data with similar kinematic settings. The DIS contribution to the born cross section was small and was calculated with the most updated DIS model [66].

The basic structure of the package will be briefly introduced here, followed by an discussion of the cross section models. The results calculated using this code will be compared with experiment results. And a simple example of how to use this code is also given at the end.

## B.2 Code Structure

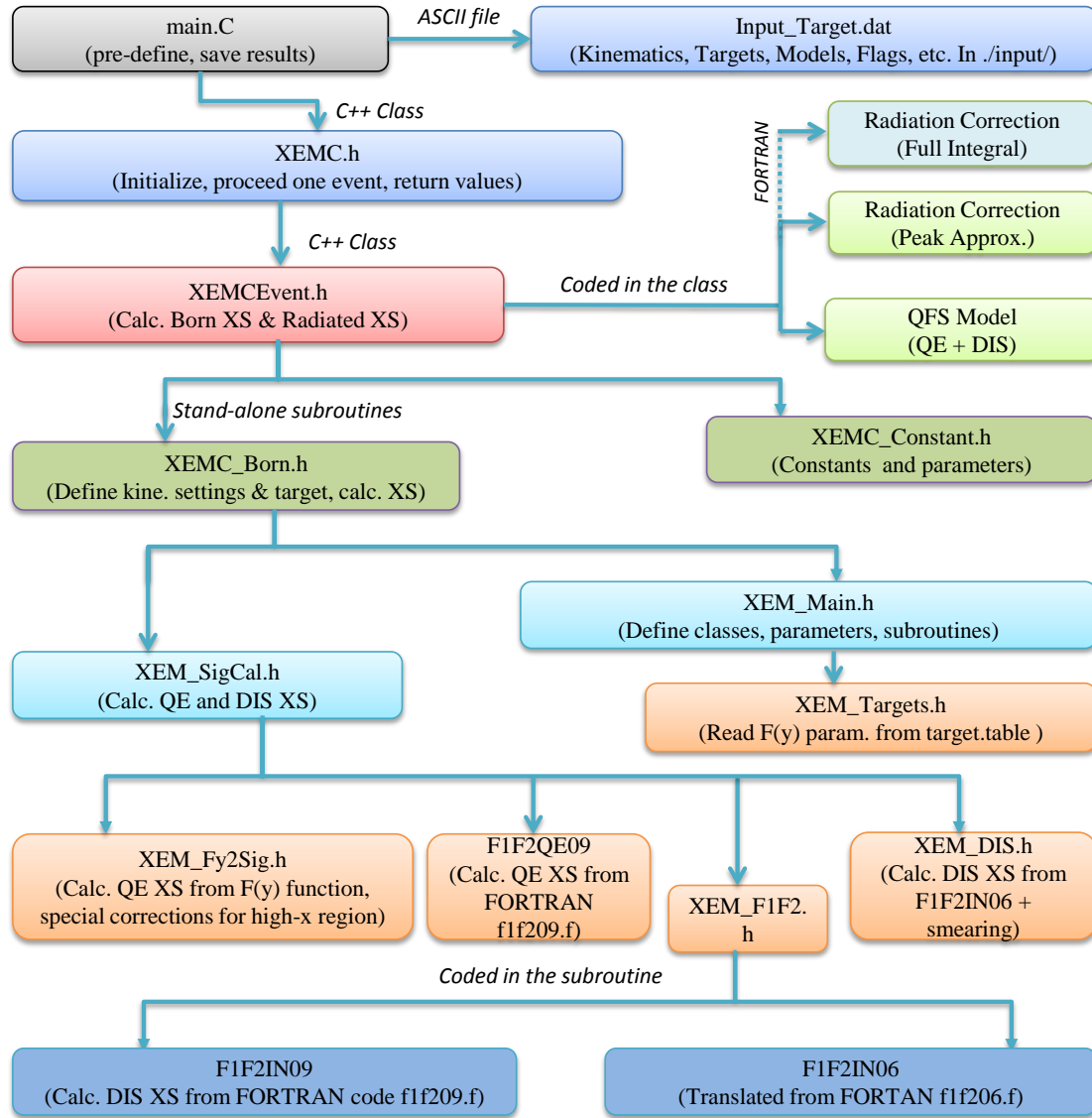
Fig. B.1 shows the basic structure of the XEMC package. Outside the main code, the input file (Fig. B.2) is defined to specify the choice of cross section models and any additional physics processes, such as the radiative correction. The reaction location can be corrected by giving the spectrometer center offset and beam position offset. The input file also includes the configuration of the target system, i.e., the target's name, mass and thickness. For cryo-targets, the materials of the target cell, the entrance and the exit of the target chamber are also given. Parameters in the input file are initialized only once in *XEMC.h*.

A XEMC event has its specified values of the initial and scattered energies as well as the scattering angle. The born cross section and radiated cross section of this event are calculated in *XEMCEvent.h* where the QFS model are embedded by default. Other born cross section models are stored in an independent subroutine, *XEMC\_Born.h*, which will be introduced in next few sections. Once the target configuration and the kinematic setting are pre-defined, the RC subroutine in *XEMCEvent.h* calculates the radiated cross section.

## B.3 Quasi-Elastic Cross Section Models

Three different QE cross section models, QE-XEM, QE-QFS, and QE-F1F209, are coded in this package. Each model will be introduced below.

## Structure of XEMC Package



### Other Files:

target.table  
(F(y) parameters for targets)

f1f209.f  
(arXiv:1203.2262)

Makefile

--- By Zhihong Ye, for XEMC V0.5, Mar. 2013

Figure B.1: Structure of XEMC Package

```

1 #####Debug Flags
2 0 #IsDebug (default=false)
3 0 #Enable energy loss (default=false)
4 119.25 #HRS Length (HRS_L or HRS_R) (cm)
5 0.0 #D_x X offset(cm in TCS) between TCS and HCS
6 0.0 #D_y Y offset(cm in TCS) between TCS and HCS
7 -0.2668 #Beam X Center (cm), -0.02668 for x>2
8 0.30220 #Beam Y Center (cm), 0.03022 for x>2
9 0 #Enable QFS cross section model to replace XEMC, default=false
10 0 #Enable Q2dep when Calculating Q.E. Peak (QFS model, default=false, not used in XEMC)
11 160.00000 #Fermi_Moment, fermi momentum of target(MeV) (QFS model,not used in XEMC)
12 15.000000 #NIE,nuclon interaction energy(MeV), shift QE central value (QFS model,not used in XE...
13 -5.50 #DEL_SEP,delta separation energy(MeV), shift central value (QFS model,not used in XEMC)
14 2 #Which form factor: (QFS model,not used in XEMC)
15 # 1: Proton 2:He3 3:He4 4:deuterium 5: Point 6: Uniform 7: Gaussian 8: Exponential
16 # 9: Shell 10: Hollow exponential 11: ... 12: Yukawa I 13: Yukawa II
17 # 14: Hollow Gaussian 15: Generalized shell model 16: Modified exponential
18 # 17: C/Fe/Pb (QFS model,not used in XEMC)
19 1 #Internal Bremsstrahlung 0/1 Disable/Enable (Calculate Elastic Tail)
20 1 #Peak approximation of Internal Bremsstrahlung 0/1 Disable/Enable (Calculate Elastic T...
21 1 #External Bremsstrahlung 0/1 Disable/Enable (Calculate Elastic Tail)
22 1 #Multiple-Photon Correction 0/1 Disable/Enable (Calculate Elastic Tail)
23 1 #Enable radiative correction (default=true)
24 5.0 #DeltaE (MeV) only for Quasielastic radiative correction
25 1 #XEMC Model Flag, 1->QE+DIS, 2->QE only, 3->Dis only
26 ######Target
27 He3 #Name
28 2 #Z: Atomic Number
29 3.0160293 #A: Atomic Weight(g/mol)
30 0.65626 #T target thickness(g/cm^2)
31 0.032810 #target density(g/cm^3)
32 0.000000 #z0 target center(cm)
33 20.00000 #T_L target length(cm)
34 2.000000 #T_H target height(cm)
35 Entrance #Name for target cell
36 13 #Z_i of initial window ( no zero )
37 26.982 #A_i of initial window (g/mol) ( no zero )
38 0.0741 #T_i target thickness of initial window(g/cm^2)
39 2.700 #density of initial window(g/cm^3)
40 Exit #Name for target cell
41 13 #Z_f of initial window ( no zero )
42 26.982 #A_f of initial window (g/mol) ( no zero )
43 0.0953 #T_f target thickness of initial window(g/cm^2)
44 2.700 #density of final window(g/cm^3)
45 0.0 #T_Theta target angle(deg) angle between beam and target(top view)
46 0 #IsBump
47 #####Windows Before Magnetic
48 #At least two materials, 1st and last
49 #For 1st material, need distance to TCS Origin
50 #For the other, just length
51 #For the rest between those materials, assume it's air
52 Vacuum #Name
53 1 #Z: Atomic Number
54 1.0 #A: Atomic Weight(g/mol)
55 51.75 #D: Distance to TCS Origin (cm)
56 #L will be changed according to Target Block
57 0.0 #density(g/cm^3)
58 0.0 #Radiation Length(g/cm^2)
59 Al #Name
60 13 #Z: Atomic Number
61 26.982 #A: Atomic Weight(g/mol)
62 3.048e-02 #L: Length (cm)
63 2.70 #density(g/cm^3)
64 24.01 #Radiation Length(g/cm^2)
65 Kapton #Name
66 5 #Z: Atomic Number
67 9.80 #A: Atomic Weight(g/mol)
68 1.778e-02 #L: Length (cm)
69 1.42 #density(g/cm^3)
70 40.61 #Radiation Length(g/cm^2)

```

Figure B.2: Input file for  $^3He$  target

### B.3.1 QE-XEM

QE-XEM was converted from the XEM cross section model, a FORTRAN package developed by EMC collaboration in Hall-C at JLab [67, 68]. XEM includes a QE model (QE-XEM) based on y-scaling [8, 11–13], a DIS model (DIS-XEM, see next section), and a RC subroutine. The entire subroutines have been converted into C++ (except the RC part) and coded in *XEMC\_Born.h*. QE-XEM is the default QE model in the package.

The scaling function,  $F(y)$  (Eq (1.21) in Section 2.x.x), is directly fitted from experimental data.  $F(y)$  for  ${}^2H$  can be extracted from the function [69]:

$$F(y) = (f_0 - B) \frac{\alpha^2 e^{-(\alpha y)^2}}{\alpha^2 + y^2} + B e^{-b|y|}, \quad (\text{B.1})$$

where,  $f_0$ ,  $B$ ,  $\alpha$ ,  $a$  and  $b$  are the parameters corresponding to the target. For heavy targets, the second term in the formula above is written differently:

$$F(y) = (f_0 - B) \frac{\alpha^2 e^{-(\alpha y)^2}}{\alpha^2 + y^2} + B e^{-(b y)^2}. \quad (\text{B.2})$$

For a list of targets, the parameters of  $F(y)$  function ( $f$ ,  $B$ ,  $\alpha$ ,  $a$ , and  $b$ ) are stored in an external ASCII file, called *target.table*. To extract the parameters, one needs to obtain the distribution of  $F(y)$  from the experimental cross sections:

$$F(y) = \sigma_{EX}^{QE} \cdot \frac{1}{Z\sigma_p + N\sigma_n} \frac{q}{\sqrt{M^2 + (y + q)^2}}, \quad (\text{B.3})$$

where  $q = \sqrt{Q^2 + \nu^2}$  and  $y$  is the solution of the equation:

$$M_A + \nu = \sqrt{M^2 + q^2 + y^2 + 2yq} + \sqrt{M_{A-1}^2 + y^2}, \quad (\text{B.4})$$

where  $M$  is the mass of the knock-out nucleon,  $M_A$  and  $M_{A-1}$  are the mass of the

#	Name	A	Z	Mass	R.L.	RESOL	ESEP	f0	BigB	a	b	alpha
1	H	1	1	1.007940	61.28	0.00	0.0000	5.6000	0.0000	0.0000	0.0000	20.0000
2	D2	2	1	2.014102	122.60	0.14	2.2500	8.82084	0.26811	6.12654	5.59714	40.9566
3	He3	3	2	3.016029	71.07	0.10	5.4900	4.97806	1.25747	2.69986	9.76214	59.9070
4	He4	4	2	4.002602	94.32	0.16	20.2000	3.27526	1.41069	2.72064	7.49020	129.0620
5	Be	9	4	9.012182	65.19	0.10	9.2800	3.4814	1.1608	3.1195	7.8398	110.9670
6	C	12	6	12.010700	42.70	0.25	17.2700	3.12386	1.47238	3.07786	7.01660	174.8817
7	Al	27	13	26.981539	24.01	0.25	9.9000	3.2783	1.3474	2.9698	6.5760	131.8450
8												
9	Ca40	40	20	40.078000	16.14	0.25	10.1569	2.93995	1.03813	3.10460	7.27470	149.0793
10	Ca48	48	20	47.952534	16.14	0.25	13.9418	2.75391	1.22894	3.06320	6.99963	177.7476
11	Fe	56	26	55.845000	13.84	0.25	10.0600	2.8900	1.4016	3.1802	7.2635	165.7000
12	Cu	64	29	63.546000	12.86	0.10	8.5500	2.8740	0.8866	3.0959	7.0945	132.4577
13	Au	197	79	196.966569	6.46	0.25	6.9300	2.6424	0.7632	3.0654	6.7678	132.4517
14												
15												
16												
17												
18												
19												
20												
21												
22												
23												
24												
25												
26												
27												
28												
29												

Figure B.3: Target table for  $F(y)$  parameters. The values had been refitted using cross section results from E02-019 and E08-014.

target nucleus and the mass of the recoil system, respectively.

The QE born cross sections,  $\sigma_{EX}^{QE}$ , can be extracted by subtracting the experimental born cross sections from the DIS cross sections calculated from the model. Consequently, different DIS models used to perform the subtraction yield different fitting values of the  $F(y)$  parameters. Fig. B.3 gives the values of these parameters for all target listed in the target table. The parameters have been fitted with data from the E02-019 [67] and E08-014, where the born cross sections were subtracted by DIS cross section using DIS-F1F209.

### B.3.2 QE-QFS

QE-QFS is based on the QFS model, an phenomenological model [70, 71] which has been used since 1960s. The model was designed to calculate both QE and DIS cross section models with Plane-Wave Impulse Approximation (PWIA) and it works better at lower  $Q^2$  region. The complete description of QFS model is referred to [70, 72]. The subroutines of the QFS model are coded in *XEMCEvent.h* and were originally developed and maintained by the collaboration from Temple University [63, 73, 74].

### B.3.3 QE-F1F209

QE-F1F209 is a part of the cross section model, F1F2QE09 which was developed by P. Bosted and V. Mamyan [66] based their work on empirical fit to electron-nucleus scattering. The model is coded in a stand-alone FORTRAN program, *f1f209.f*. An external link is given in the XEMC package to call the subroutines in the FORTRAN code. To successfully compile the code, a library named *libg2c.so* must be specified in the *Makefile*.

## B.4 DIS Models

The DIS cross section model not only calculates the cross section of the deep inelastic scattering process but also includes other inelastic processes, such as resonances. There are three DIS models coded in the package. Since the kinematic settings of E08-014 experiment was well above the QE peak, the contribution from inelastic processes is relatively small, and these models were not iterated with the existing DIS data.

### B.4.1 DIS-QFS

DIS-QFS is also a part of the QFS subroutines [63]. This model includes the following processes:

- Scattering from two interaction nucleons (Dip region),
- Delta Electroproduction ( $\Delta$ ),
- Two resonances at 1500  $MeV$  and 1700  $MeV$ , and,
- Deep inelastic scattering (DIS).

### B.4.2 DIS-XEM

DIS-XEM were specially designed for the EMC experiment based on P. Bosted previous empirical fit, F1F2IN06 [75]. To agree with the EMC data, the model was twisted with several corrections in different range of  $0.8 < x_{bj} < 1.0$  , and the code becomes complicated and runs slowly, especially when performing radiative correction. The subroutines have been converted from FORTRAN into C++ and coded in *XEMC\_Born.h*.

### B.4.3 DIS-F1F209

DIS-F1F209 also comes from F1F2IN09 and is coded in *f1f209.f*. It is the default DIS model in XEMC.

## B.5 Radiative Corrections

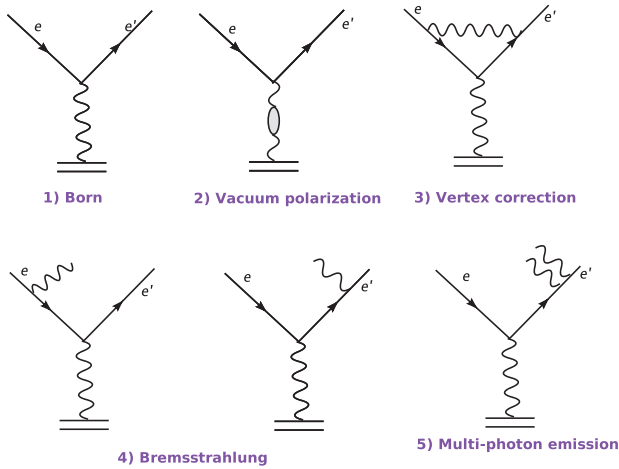


Figure B.4: Feynman diagrams for radiation effect in inclusive lepton-nucleon scattering. Only the lowest orders are shown here.

The electron-nucleon scattering process can be modelled by one-photon-exchange-approximation (OPEA), where the electron and the nucleon interact by exchanging one photon. The inclusive cross section of the process is called the born cross section. There are higher order processes, called radiative effects, contribute to the measured cross sections, as shown in Fig. B.4. The experimental raw cross section is named as the radiated cross section, which has to be corrected to obtain the experimental born cross section:

$$\sigma_{\text{born}}^{\text{EX}} = \frac{\sigma_{\text{born}}^{\text{Model}}}{\sigma_{\text{rad}}^{\text{Model}}} \cdot \sigma_{\text{rad}}^{\text{EX}}, \quad (\text{B.5})$$

where  $\sigma_{\text{born}}^{\text{Model}}$  and  $\sigma_{\text{rad}}^{\text{Model}}$  are the born and radiated cross section calculated from the model, while  $\sigma_{\text{born}}^{\text{EX}}$  and  $\sigma_{\text{rad}}^{\text{EX}}$  are the born and radiated cross sections measured from

the experiment. The ratio term is generally called the radiative correction factor.

The radiation effects contain the external radiation and the internal radiation. The external radiation, including external bremsstrahlung and ionization, happens when the incoming or the outgoing electron radiates a real photon when it interacts with the nuclear medium other than the target nucleon. This effect mainly depends on the material and thickness of the target. The internal radiation contains the soft processes, such as internal bremsstrahlung, and the hard processes, such as vacuum polarization, vertex correction and multiple-photon exchange. The initial and final energies of the electron have been modified during those processes, which causes the measure cross section deviated from the true value.

The idea of radiative correction is carefully discussed in [76, 77], and an radiative correction package, RadCor, was developed based on the idea [63, 73]. Peak approximation method was used in the package to increase the speed of the radiated cross section calculation. Important subroutines in this package have been migrated to XEMC.

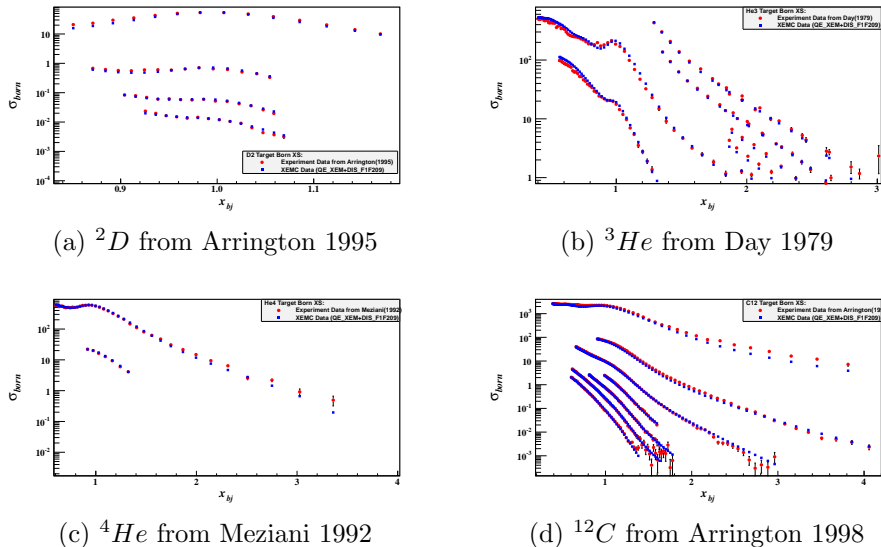


Figure B.5: Comparing XEMC models and Experiment data, where the data are from QE-Achieve [7]

## B.6 Performance

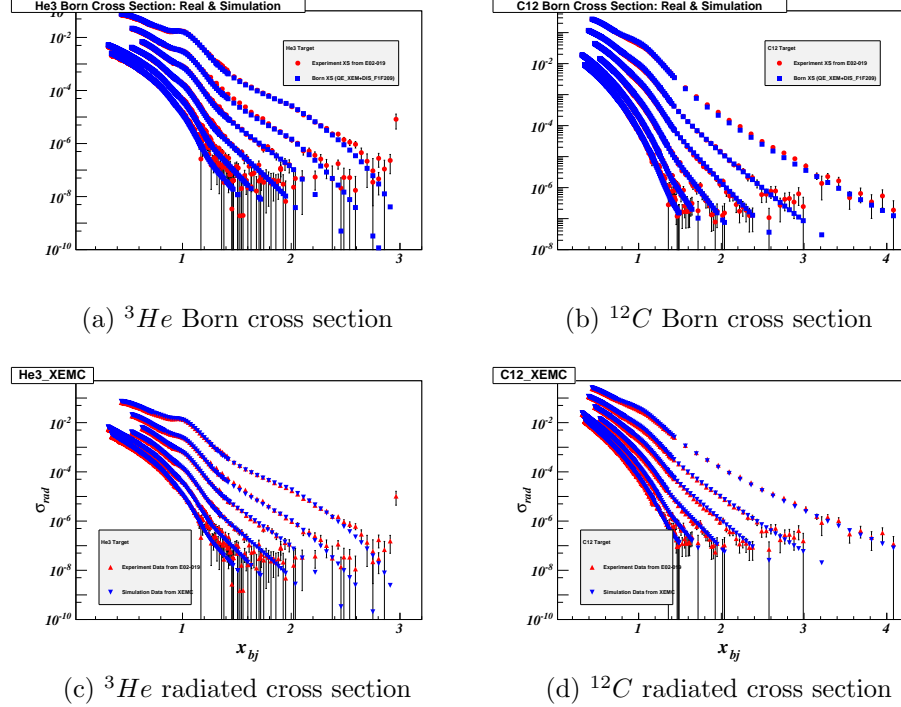


Figure B.6: Check radiative correction using E02-019 data, where the target thickness and target system are included [67]

In this section, the cross sections calculated from XEMC with the QE-XEM model and the DIS-F1F209 model are directly compared with several experiments results stored in the QEArxive [7] (Fig. B.5) as well as the E02-019 data (Fig. B.6a and Fig. B.6b). Overall, the model and the data agree nicely. The performance of radiative correction is examined with the E02-019 data of which the target configurations were known. From Fig. B.6c and Fig. B.6d, the radiated cross sections from XEMC agree well with the data above the QE region, where at  $x_{bj} < 1$  a small deviation can be noticed due to the use of the peak approximation method. The E08-014 data is well above the QE peak so the deviation wasn't important.

## B.7 Examples

A simple example to use the XEMC package is given in this section.

---

```

#include "XEMC.h"

int main(int argc,char** argv){
    XEMC* Event = new XEMC();
    TString Target_Name = "C12";
    //For flags and target info
    Event->Init(Form("./input/%s_Input.dat",Target_Name.Data()));

    //Kinematic setting
    int A = 12, Z = 6; //Target
    double E0 = 3.356; //GeV
    double Ep = 2.505; //GeV/c
    double Theta = 25.00; //Degree

    //Reaction location in the target, usually Radiation Effect
    //is calculated at the target center.
    //It is useful for targets with non-uniform density.
    int L = 0.0;

    //Calculate XS for the event
    int err = Event->Process(E0,Ep,Theta,A,Z,);
    if(err>=0){
        //Return values
        double xs_rad = Event->XS_Rad();
        double xs_qe = Event->XS_QE();
        double xs_dis = Event->XS_DIS();
        double xs_born = Event->XS_Born();
    }
    cerr<<Form("@@@ For %s Target, E0=%5.3f GeV, Ep=%5.3f GeV, Theta=%5.3f: ", Target_Name.Data(), E0, Ep, Theta)<<endl;
    cerr<<Form("  XS_Born=%e, XS_QE=%e, XS_DIS=%e, XS_Rad=%e", xs_born, xs_qe, xs_dis, xs_rad)<<endl;

    delete Event;
}

```

---

## Appendix C

# Momentum Correction in HRS-R

Each HRS is composed of a Dipole and three quadrupoles in the order of Q1, Dipole, Q2 and Q3. Four magnets usually have the same central momentum value. Using the focal plane quantities which are provided by the VDC tracking, a HRS optics matrix reconstructs  $\delta p$ ,  $y_{tg}$ ,  $\theta_{tg}$ , and  $\phi_{tg}$ , which are the target plane quantities of an event at the reaction point. As discussed in Section 3.3, during E08-014 experiment the field of the Q3 magnet on HRS-R (RQ3) was scaled to 87.72% of its normal value, and the transportation of particles in the HRS-R had be changed. While the matrix elements of  $y_{tg}$ ,  $\theta_{tg}$ , and  $\phi_{tg}$  have been properly optimized, the momentum matrix (the D-terms) was not able to be calibrated since the momentum calibration data could not be taken at elastic region. It requires an additional correction to get the correct value of  $\delta p$ . In this section, a method will be introduced to correct the  $\delta p$  on HRS-R using SAMC data and the SNAKE model.

In the Hall-A Single Arm Monte Carlo tool (SAMC), each HRS magnet's transportation from the entrance to the exit is simulated in the SNAKE model as a series of forward transportation functions (FWDs). For example, the quantities at the Q1 exit,  $x_{Q1}^{ex}$ ,  $y_{Q1}^{ex}$ ,  $\theta_{Q1}^{ex}$ ,  $\phi_{Q1}^{ex}$ , and  $l_{Q1}^{ex}$  are calculated with corresponding five FWDs using the same set of quantities at the Q1 entrance which can be directly deduced from

the target plane quantities. These quantities can be further used as the inputs to calculate the quantities at the Dipole exit, and so on. The focal plane quantities,  $x_{fp}$ ,  $y_{fp}$ ,  $\theta_{fp}$ , and  $\phi_{fp}$ , are given by the FWDs of Q3. The focal plane quantities are smeared with the resolution of the HRS VDCs defined in the simulation.

Similar to the HRS optics matrix, a set of backward polynomial functions (BWDs) directly calculates each target plane quantity with the four focal plane quantities as inputs, instead of performing the backward transports among individual magnets.

To simulate the HRS-R setting during this experiment, new FWDs were generated for the RQ3 with the twisted field, named as  $FWD_{twist}^{Q3}$ , and they replaced the FWDs with the normal field setting ( $FWD_{norm}^{Q3}$ ) in the simulation.

Two sets of new BWDs were produced by SNAKE to describe the twisted RQ3 field. The first set ( $BWD_{twist}^D$ ) has updated reconstruction of all target plane quantities. The second set ( $BWD_{norm}^D$ ) has also included the new reconstruction of target plane quantities, except the  $\delta p$  reconstruction which was generated with the normal RQ3 field.

In SAMC, two types of simulation events were generated with the same event seeds. The HRS-R in first type of events was simulated with  $FWD_{twist}^{Q3} + BWD_{twist}^D$ , and the values of  $\delta p$  in these events should be correctly reconstructed and are labelled as  $\delta p_{right}$ . In the second type, the HRS-R was simulated with  $FWD_{twist}^{Q3} + BWD_{normal}^D$  which reconstructs incorrect values of  $\delta p$ , named as  $\delta p_{wrong}$ .

In the real data, the error of the momentum reconstruction caused by using the un-calibrated D-terms can be simulated by the difference of  $\delta p_{right}$  and  $\delta p_{wrong}$  in the simulation data:

$$\Delta\delta p = \delta p_{right} - \delta p_{wrong}, \quad (C.1)$$

which can be corrected by a correction function defined as:

$$\begin{aligned} f(x_{fp}, \theta_{fp}, y_{fp}, \phi_{fp}) &= \sum_{i=0}^{N_A} A_i x_{fp}^i + \sum_{j=0}^{N_B} B_j \theta_{fp}^j + \sum_{k=0}^{N_C} C_k y_{fp}^k \\ &+ \sum_{l=0}^{N_D} D_l \phi_{fp}^l + \sum_{m=0}^{N_E} E_m \delta p_{wrong}^m, \end{aligned} \quad (\text{C.2})$$

where the first four terms are the polynomial functions of the focal plane quantities, and the last term is used to correct any high-order optics effect. The procedure to obtain the correction function from the simulation data is presented below.

First of all, the first term in Eq (C.2) is fitted with  $x_{fp}$ :

$$\Delta \delta p(x_{fp}) = \delta p_{right} - \delta p_{wrong} = \sum_{i=0}^{N_A} A_i x_{fp}^i, \quad (\text{C.3})$$

which gives a new momentum value,  $\delta p_{x_{fp}} = \delta p_{wrong} + \sum_{i=0}^{N_A} A_i x_{fp}^i$ , and the residual error,  $\Delta \delta p = \delta p_{right} - \delta p_{x_{fp}}$ , is further fitted with  $\theta_{fp}$ :

$$\Delta \delta p(\theta_{fp}) = \delta p_{right} - \delta p_{x_{fp}} = \sum_{j=0}^{N_B} B_j \theta_{fp}^j, \quad (\text{C.4})$$

which gives  $\delta p_{\theta_{fp}} = \delta p_{x_{fp}} + \sum_{j=0}^{N_B} B_j \theta_{fp}^j$ . Similar corrections are applied to  $y_{fp}$ ,  $\phi_{fp}$  and  $\delta p_{wrong}$ :

$$\Delta \delta p(y_{fp}) = \delta p_{right} - \delta p_{\theta_{fp}} = \sum_{k=0}^{N_C} C_k y_{fp}^k, \quad (\text{C.5})$$

$$\Delta \delta p(\phi_{fp}) = \delta p_{right} - \delta p_{y_{fp}} = \sum_{l=0}^{N_D} D_l \phi_{fp}^l, \quad (\text{C.6})$$

$$\Delta \delta p(\delta p_{wrong}) = \delta p_{right} - \delta p_{\phi_{fp}} = \sum_{m=0}^{N_E} E_m \delta p_{wrong}^m. \quad (\text{C.7})$$

Combining equations from Eq (C.3) to Eq (C.7), Eq (C.2) leads to:

$$\delta p_{right} = \delta p_{wrong} + f(x_{fp}, \theta_{fp}, y_{fp}, \phi_{fp}), \quad (C.8)$$

Fig. C.1 shows the fitting result the distribution of  $\Delta\delta p$  for each corrections. The final residual error,  $\Delta\delta p(\delta p_{wrong})/\delta p_{right}$ , is close to 0.03% (Fig. C.2) indicating that the un-calibrated momentum reconstruction in RQ3 has been corrected.

Eq C.8 can be applied to the experimental data to correct the value of  $\delta p$  for each event which is firstly reconstructed by the un-calibrated HRS optics. The performance of the correction can be examined by comparing the momentum distribution of the data taken in two HRSs with the same setting. Shown in Fig. C.3, the momentum distribution on HRS-R should be identical to the one on HRS-L after applying the correction function, but its acceptance would be slightly wider than the one of HRS-L because of the defocussing effect of RQ3.

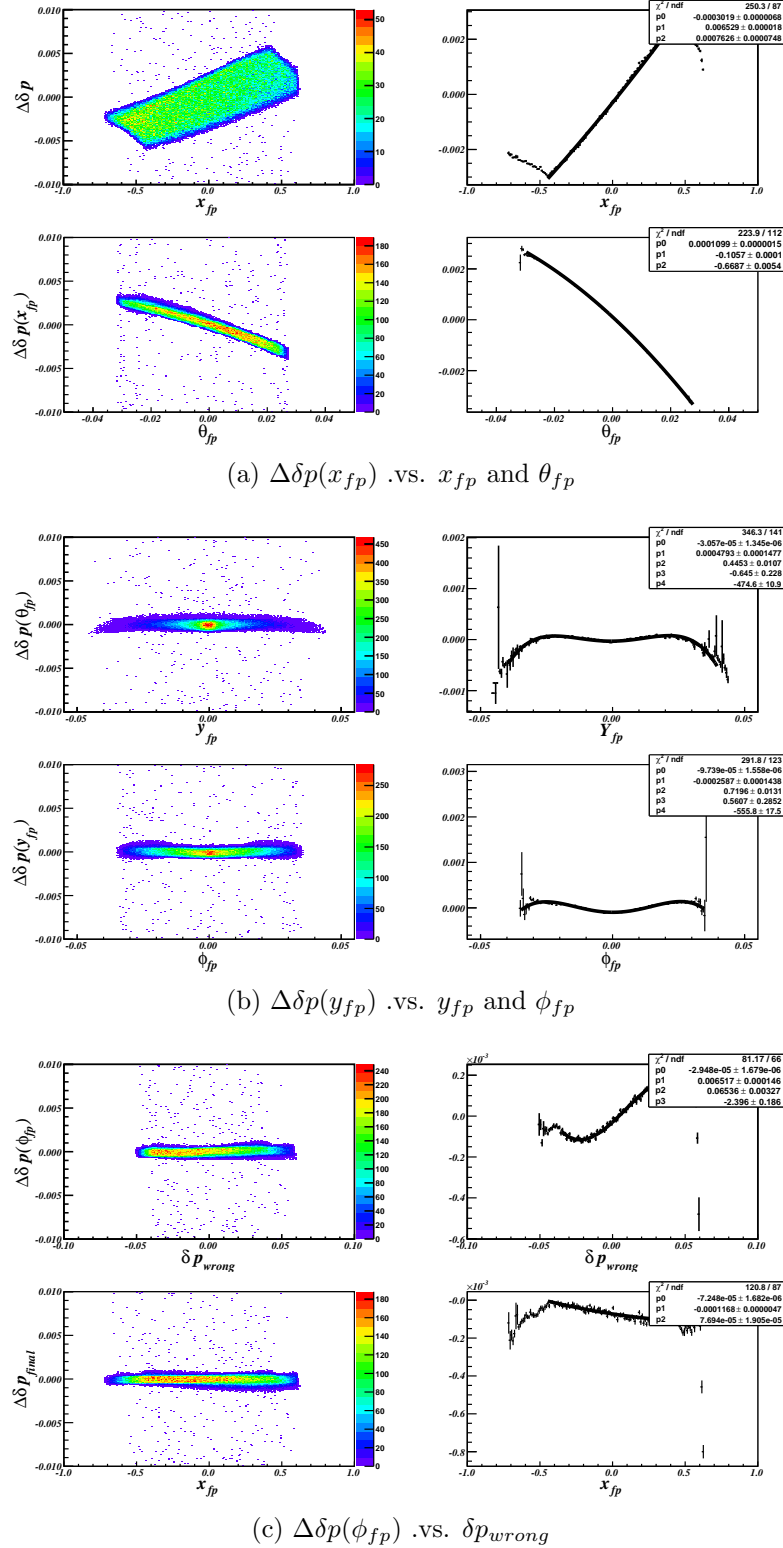


Figure C.1:  $\delta p$  correction function fitting with the focal plane variables. In each raw, the left is the 2-D histogram of  $\Delta\delta p$  versus each fitting variable, while the right plot is the profile of the 2-D histogram, which is fitted with the polynomial function defined in Eq (C.8). The bottom two plots give the final result after applying all corrections.

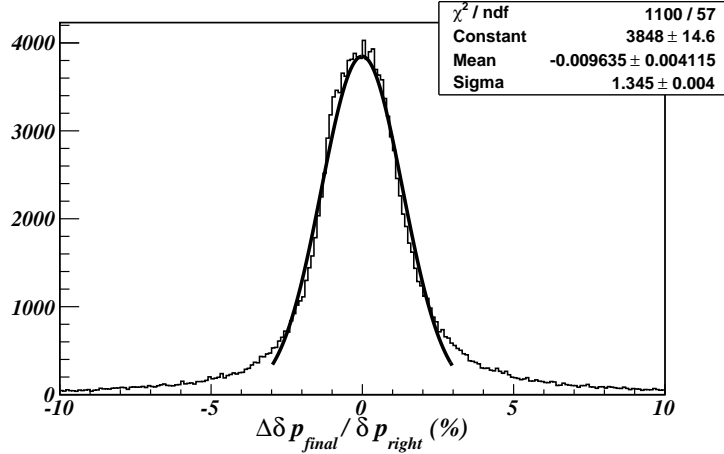


Figure C.2: The residual error of  $\delta p$  correction function. The momentum reconstruction value can be corrected with the error around 1.3%.

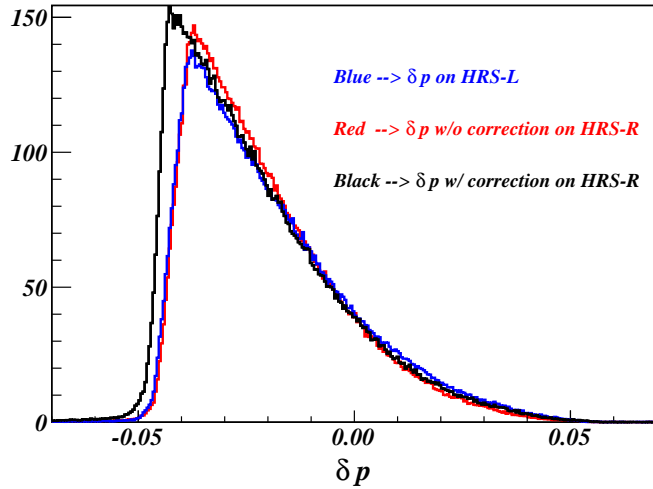


Figure C.3:  $\delta p$  correction function applying on real data. The data was taken on the carbon target with both HRSs at Kin5.0. The momentum distribution on HRS-R without the correction is different from the one on HRS-L (blue), which, however, agrees with the momentum distribution on HRS-R after the correction (black) at the central region. The  $\delta p$  acceptance range on HRS-R is wider than the one on HRS-L, which can be explained by the defusing effect of RQ3.

## Appendix D

# Non-Uniform Cryogenic Targets

As discussed in Section 5.4.2, the cryogenic targets (cryo-targets) used in E08-014 presented strange distributions of  $z_{react}$  which gives the yield of reaction points along the beam direction. These distributions indicate that their densities were not uniform but instead, vary along the 20 cm cells. As proved by a Monte Carlo simulation of the cryogenic target system [78], such non-uniform density profiles were caused by the special design of the target cells and the direction of the cryogenic flow, as shown in Fig. D.1.

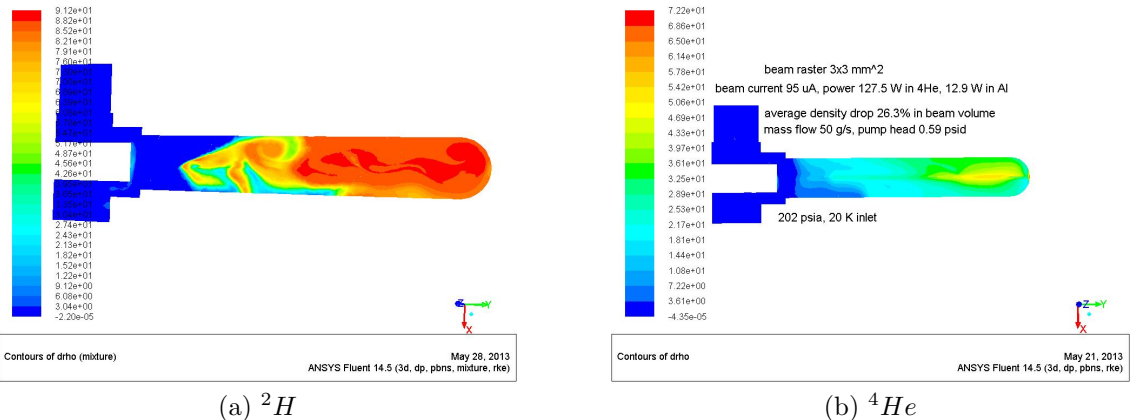


Figure D.1: Cryo-target density profiles from simulation. The color contour denotes the value of the target density. The left plot is for  $^2H$  and the right plot is for  $^4He$ . The density profile of  $^3He$  is not shown here. Both plots present fluctuation of the target density along the cell.

The absolute target density is important to extract the cross sections of electron scattering on the target nucleus as well as to perform the radiative correction. The initial the target density when beam is off can be surveyed before the experiment. When beam is on, however, it varies with the beam current because of the boiling effect. Such an effect is negligible for solid targets but it should be significant for cryo-targets. Especially for non-uniform cryo-targets, the boiling effect differs along the target cell, and meanwhile, the radiation correction becomes more complicated since the radiation effect largely depends on the location and direction of the electron-scattering process. In this chapter, a detailed study of the boiling effect is given, followed by a discussion of extracting the cry-target density distributions. A procedure to evaluate the radiation correction factors for non-uniform cryo-targets will be introduced in the end.

## D.1 Boiling Study

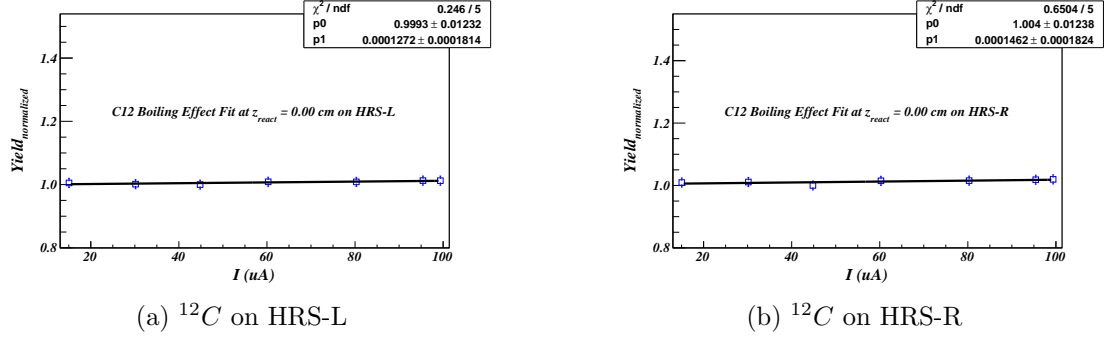


Figure D.2:  $^{12}C$  boiling effect fitting. Since  $^{12}C$  should have very small boiling effect, this study is used to check any rate-dependence effect at different current settings

During E08-014, several boiling study runs were taken with different beam current on these cryo-targets, as well as on the  $^{12}C$  target, which was used to check any rate-dependence effects.

The experimental yield depends on the target density, the beam charge and the

cross section of electron-nucleus scattering. While the average cross section shouldn't change for one kinematic setting, the yield normalized by the beam charge should be directly proportional to the target density:

$$Y(I) = Y(0) + Slop \cdot I, \quad (D.1)$$

where  $Y(I)$ , the yield for one run with beam current  $I$ , is equal to the total number of experimental events after all necessary cuts divided by the the total accumulated charge.  $Y(0)$  is the yield extrapolated to zero beam current. By fitting Eq (D.1) with the data of the boiling study runs, one can obtain the variation of the target density at different current, given as:

$$\rho(I) = \rho(0) \cdot (1.0 + BF \cdot I/100), \quad (D.2)$$

where  $BF = Y(0)/Slop$  is the boiling factor of the target.

Shown in Fig. D.2, the fitting result of  $^{12}C$  indicates that for a fixed target density, the yield does not change at different current. For cryo-target, the data was binned in  $z_{react}$  which was divided into 60 bins. In each bin, the yield was calculated and one can fit the boiling factor by the formula:

$$Y(I, z_{react}^i) = Y(0, z_{react}^i) + Slop(z_{react}^i) \cdot I, \quad \text{where } i = 1, \dots, 60, \quad (D.3)$$

which gives the variation of the density in each bin:

$$\rho(I, z_{react}^i) = \rho(0, z_{react}^i) \cdot (1.0 + BF(z_{react}^i) \cdot I/100), \quad (D.4)$$

where,

$$BF(z_{react}^i) = \frac{Y(0, z_{react}^i)}{Slop(z_{react}^i)}. \quad (D.5)$$

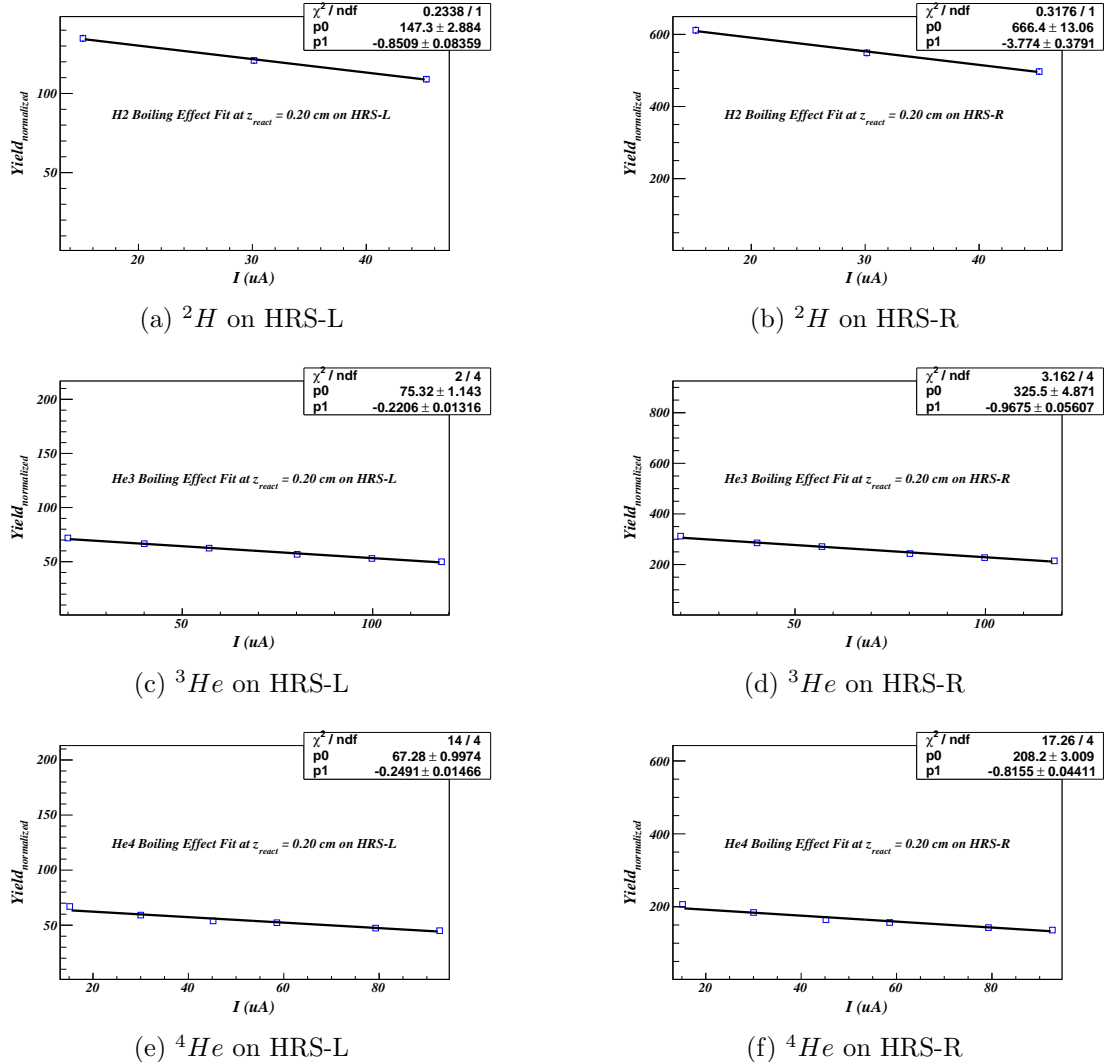


Figure D.3: Cryo-targets boiling effect fitting. They are examples near the center of the targets. Each target was divided into 60 bins along the target cell, where the boiling factor was individually fitted.

During the fitting, the values of yields have been normalized to their minimum values since the absolute values are irrelevant.

As examples, Fig. D.3 shows the fitting results of boiling factors at the center of  $z_{react}$  for three cryo-targets, where the curves are well fitted by linear functions. The curve of normalized  $Y(0, z_{react}^i)$  denotes the target density profile along the cell, as shown in Fig. D.4, where the peaks of end-cups are clearly presented. The distribution of  $BF(z_{react}^i)$  for each target, given in Fig. D.5, shows the boiling effect

at different  $z_{react}$ , and demonstrates that the non-uniform cryo-target densities were mainly caused by the highly localized boiling effects. In the plot the values of  $z_{react}$  at the positions of end-cups are close to zero which agree with the fact that the density of aluminium walls shouldn't change with beam current. Results from both HRSs were compared and found out to agree nicely with each other.

## D.2 Extracting Density Distributions

From Eq (D.3), the target density profile can be obtained by extracting the distribution of  $Y(0)$  during the boiling study. In this section, a different method is applied to extract the density distribution by using the experimental data and simulation data.

Since  $z_{react}$  is along the incoming beam direction which is also the orientation of the target cell, the  $z_{react}$  distribution in the experimental data,  $z_{react}^{EX}$ , gives the distribution of yields in a certain current setting, which also corresponds to the variation of density along the target. However,  $z_{react}^{EX}$  should also contain the acceptance effect of the HRS and the cross section effect, which statistically weights the yields in different  $z_{react}$  location where the central scattering angle varies. One can apply the simulation data generated by SAMC, which simulates the acceptance effect of HRSs, to plot the simulated  $z_{react}$  distribution,  $z_{react}^{MC}$ , which is furthered weighted by the cross section values calculated from XEMC. When the target density distribution in the simulation data is uniform,  $z_{react}^{MC}$  only carries the acceptance effect and the cross section effect. By plotting the histograms of  $z_{react}^{EX}$  and  $z_{react}^{MC}$  with the same range and bin-size, one takes to ratio of two histogram, which leads to a clean relative density distribution of the target at the current setting.

The plots on the left hand side of Fig. D.6 show the distribution of  $z_{react}^{EX}$  and  $z_{react}^{MC}$  at three different current settings for each target, while the plots on the right hand side give the fitting results of the relative density distributions. A polynomial

function is used for each fitting process.

One can use the density distributions at the minimum current (15 uA, 20 uA and 15 uA for  $^2H$ ,  $^3He$  and  $^4He$ , respectively), and apply the boiling factors to calculate the density distribution at beam current equal to zero,  $\rho(0)$ . Then the density distribution at any current settings,  $\rho_{Calc}(I)$  can be calculated using Eq (D.4). To verify the boiling study results and the density distributions at different current settings, the distributions of  $\rho_{Calc}(I)$  and  $\rho(I)$  extracted in Fig. D.6 were compared, as shown in Fig. D.7. Note that the contribution from the two end-cups were removed by applying the cut,  $|z_{react}| \leq 7.5\text{ cm}$ . The plots reveal that the results of boiling study successfully characterize the change of target density with different beam current.

Fig. D.7 also compares the distributions of the target density obtained from the boiling study and from the method discussed in this section. Ignoring the statistical fluctuation of the histograms, both methods give similar density profiles, and the small difference can be explained by the errors of the HRS acceptance simulation in SAMC and the cross section model in XEMC.

### D.3 Absolute Density

When the density distribution is uniform, the absolute density of a cry-target can be calculated using the temperature and pressure readings from the target system with the fixed volume of the target cell. However, the calculation becomes impossible when the density is not uniform since the temperature and pressure fluctuate inside the target. While the relative density distribution has been extracted as discussed in previous section, one can obtain the absolute density distribution by calculating the density at the entrance of the target cell where the temperature and pressure were monitored.

Whereas, the extracted relative density distribution at the entrance does not re-

flect the true density profile of the cryo-target due to the contamination of the aluminium end-cup during the boiling study, and an assumption has been made to assign the density value at the entrance to the value at  $-10 \leq z_{react} \leq -7.5 \text{ cm}$ . The true value should not deviate too far away from this value since this location is very close to the entrance and the coolant flow should be able to maintain the same temperature as at the entrance. The deviation can be corrected when comparing the experimental yield and the simulation yield, while the last one, yet, depends on the cross section model. To obtain the accurate density, one can utilize the 2N-SRC plateaus of cross section ratio of the carbon target to the cryo-targets [28–30], which have been well measured in previous experiments. Table D.1 gives the densities of cryo-targets at the entrance and the yield-normalized density at  $z_{react} = 7.5 \text{ cm}$ , where the values will be updated when they are further normalized by the 2N-SRC plateaus.

Target:	$^2H$	$^3He\text{-I}$	$^3He\text{-II}$	$^4He$
$\rho_{\text{entrance}} \text{ (g/cm}^3\text{):}$	0.1676	0.0213	0.0296	0.0324
$\rho_{z_{react}=-7.5 \text{ cm}} \text{ (g/cm}^3\text{):}$	0.1906	0.0210	0.0292	0.0280

Table D.1: Cryo-targets densities, where two values of the  $^3He$  density refer to two different run periods. The values of  $\rho_{\text{entrance}}$  are calculated from the temperature and pressure reading [48]. The values of  $\rho_{z_{react}} = -7.5 \text{ cm}$  are the values of  $\rho_{\text{entrance}}$  normalized by the ratio of the experimental yield and the simulation yield and will be further corrected by comparing the 2N-SRC plateaus.

## D.4 Radiative Correction

The most essential parameter during the radiative correction is the radiation length of the target. For uniform target, the radiation length is usually evaluated at the center of the target. For non-uniform targets, such an approximation has to be carefully examined.

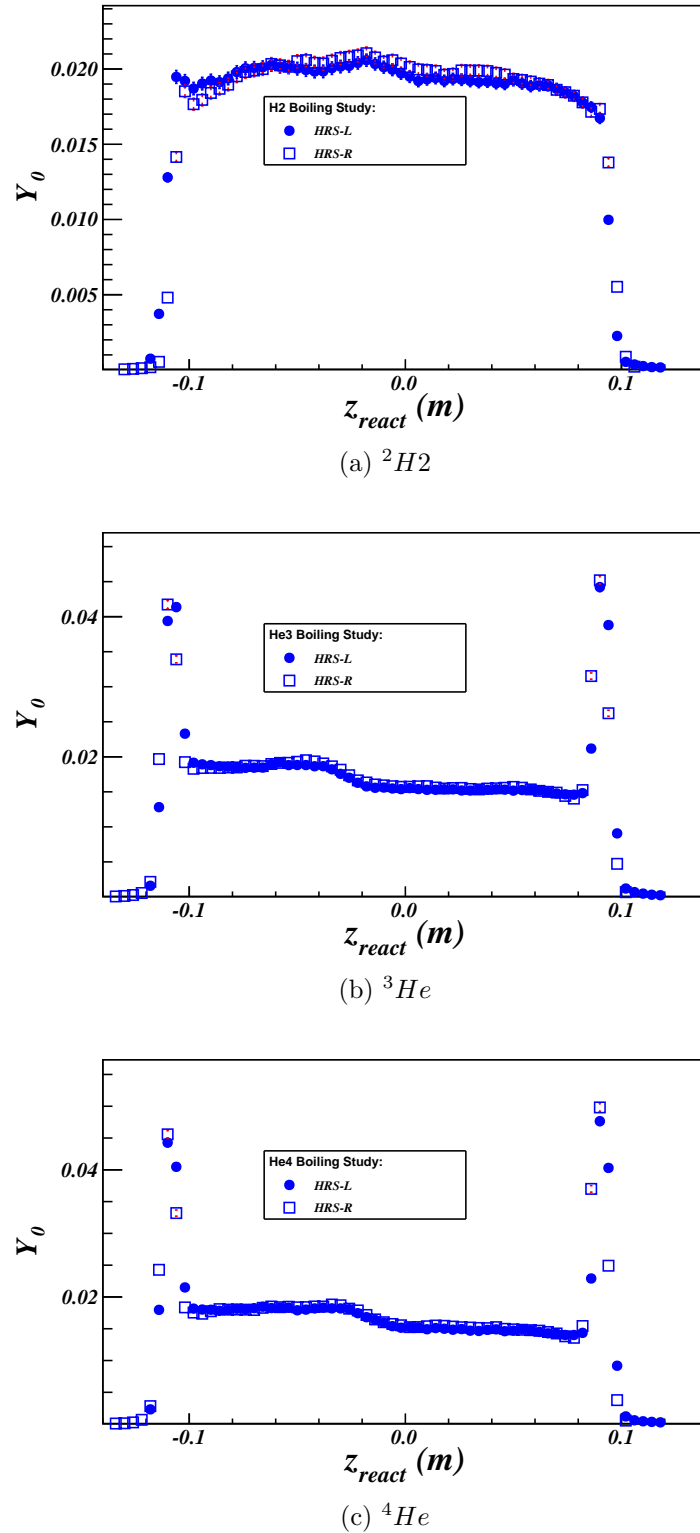


Figure D.4: Cryo-target density profiles from boiling study. The results from both HRSs agree with each other for each target, and the peaks denote the contributions from the end-cups of the target cell.

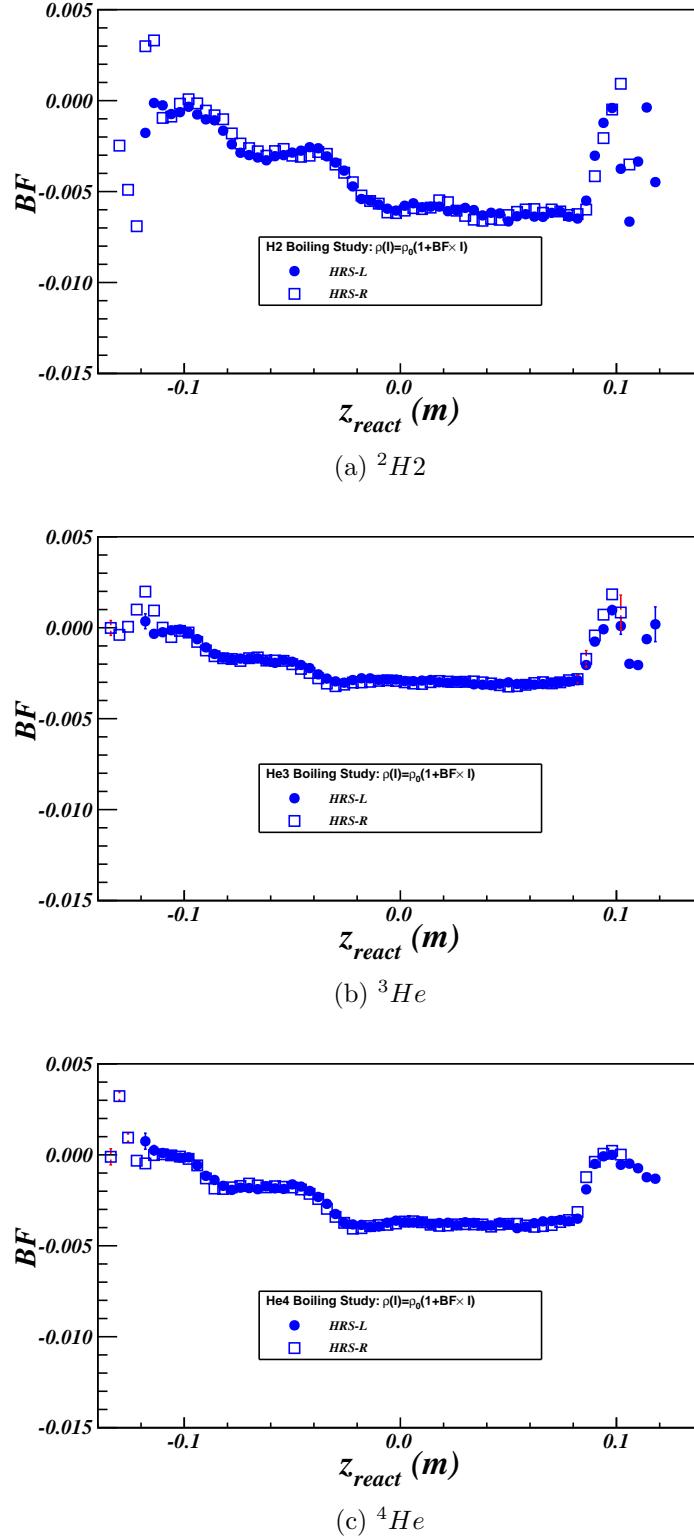


Figure D.5: Cryo-target boiling factor distribution. Each plot clearly shows that the boiling effect varies along the target cells. The boiling factors at the end-cups are reasonably close to zero. The studies from both HRSs give consistent results.

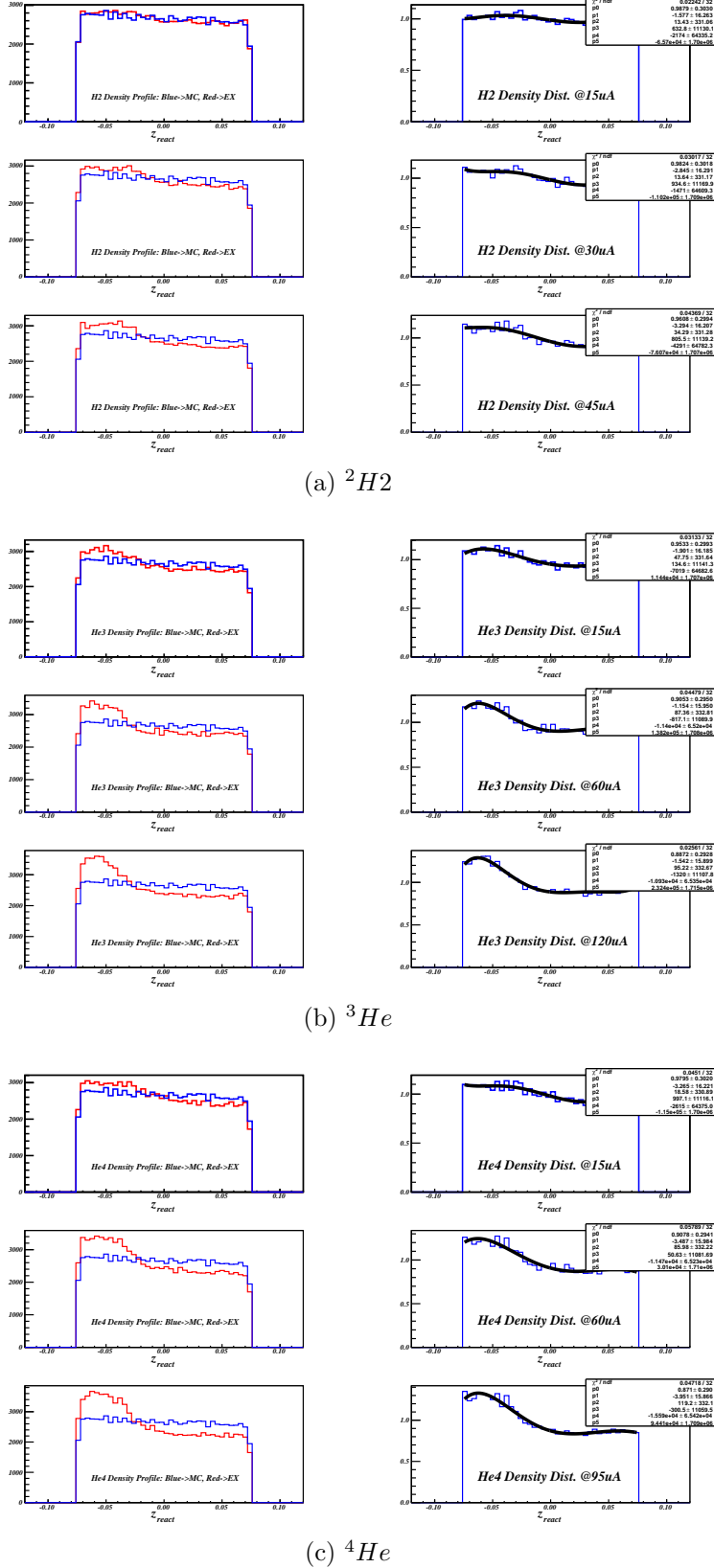


Figure D.6: Cryo-target density distributions extracted from data. The density distribution was extracted by taking the histogram ratio of  $z_{react}$  from experimental data (red lines in plots on the right panel) and from simulation data with flat density distribution (blue lines in plots on the right panel). For each target, the density distributions at the minimum, middle and maximum currents were individually extracted (on left panel). The current settings are given in the plots.

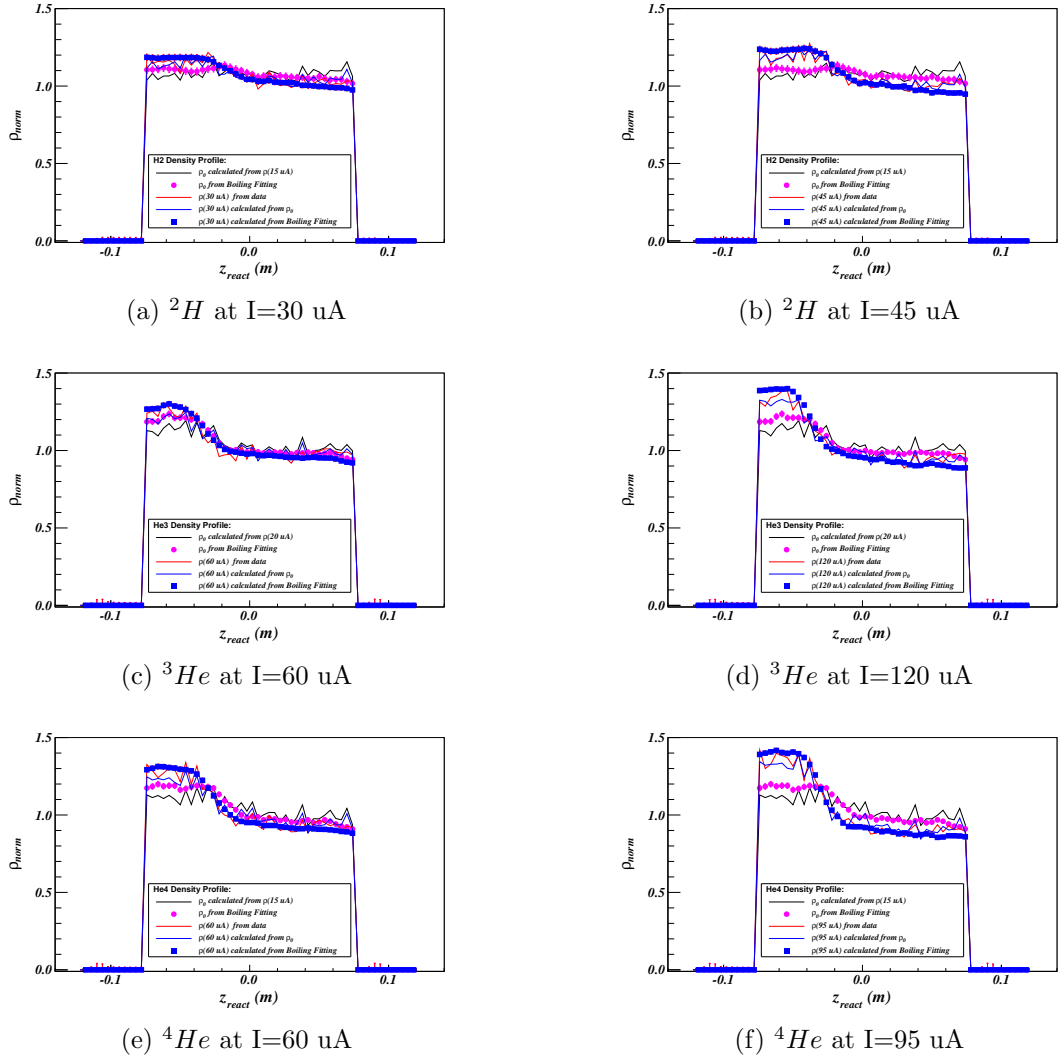


Figure D.7: Cryo-targets relative density distribution extracted from data and corrected by the boiling factors. The density values were calculated in each  $z_{react}$  bin and the peaks in these distribution were due to the statistical fluctuation. To remove the contribution of the end-cups, a cut was apply on the target length,  $|z_{react}| \leq 7.5 \text{ cm}$

# Bibliography

- [1] P. Navrátil *et al.*, Phys. Rev. Lett. **87**, 172502 (2001).
- [2] D. Day, private communication.
- [3] L. Lapiks, Nuclear Physics A **553**, 297 (1993).
- [4] J. Kelly, Adv. Nucl. Phys. **23**, 75 (1996).
- [5] N. S. Szabo and A. Ostlund, Modern quantum chemistry.
- [6] B. Frois and C. N. Papanicolas, Ann.Rev.Nucl.Part.Sci. **37**, 133 (1987).
- [7] O. Benhar, D. Day, and I. Sick, Rev. Mod. Phys. **80**, 189 (2008).
- [8] J. Arrington, Inclusive Electron Scattering From Nuclei at  $x_f 1$  and High  $Q^2$ , 1998.
- [9] D. Tomańek and M. A. Schluter, Phys. Rev. B **36**, 1208 (1987).
- [10] J. D. Forest, Nucl. Phys. **A392**, 232 (1983).
- [11] G. B. West, Physics Reports **18**, 263 (1975).
- [12] C. Ciofi degli Atti, S. Liuti, and S. Simula, Phys. Rev. C **41**, R2474 (1990).
- [13] S. Boffi, C. Giusti, and F. Pacati, Physics Reports **226**, 1 (1993).
- [14] C. Ciofi degli Atti, D. B. Day, and S. Liuti, Phys. Rev. C **46**, 1045 (1992).
- [15] O. Benhar, Phys. Rev. C **87**, 024606 (2013).
- [16] C. Ciofi degli Atti and S. Simula, Phys. Rev. C **53**, 1689 (1996).
- [17] J. Arrington, D. Higinbotham, G. Rosner, and M. Sargsian, Progress in Particle and Nuclear Physics **67**, 898 (2012).
- [18] L. FRANKFURT, M. SARGSIAN, and M. STRIKMAN, International Journal of Modern Physics A **23**, 2991 (2008).
- [19] M. Alvioli, C. C. d. Atti, and H. Morita, Phys. Rev. C **72**, 054310 (2005).
- [20] R. Subedi *et al.*, Science **320**, 1476 (2008), 0908.1514.

- [21] S. C. Pieper and R. B. Wiringa, Annual Review of Nuclear and Particle Science **51**, 53 (2001).
- [22] R. Schiavilla, R. B. Wiringa, S. C. Pieper, and J. Carlson, Phys. Rev. Lett. **98**, 132501 (2007).
- [23] J. Arrington, D. Day, D. Higinbotham, and P. Solvignon, Three-nucleon short range correlations studies in inclusive scattering for  $0.8 < Q^2 < 2.8(GeV/c)^2$ , <http://hallaweb.jlab.org/experiment/E08-014/>, 2011.
- [24] J. Arrington, D. Day, D. Higinbotham, and P. Solvignon, Precision measurement of the isospin dependence in the 2N and 3N short range correlation region, [http://www.jlab.org/exp\\_prog/proposals/11/PR12-11-112.pdf](http://www.jlab.org/exp_prog/proposals/11/PR12-11-112.pdf), 2014.
- [25] L. Frankfurt and M. Strikman, Physics Reports **76**, 215 (1981).
- [26] M. Sargsian *et al.*, Journal of Physics G: Nuclear and Particle Physics **29** (2003).
- [27] L. Frankfurt and M. Strikman, Physics Reports **160**, 235 (1988).
- [28] L. L. Frankfurt, M. I. Strikman, D. B. Day, and M. Sargsyan, Phys. Rev. C **48**, 2451 (1993).
- [29] CLAS Collaboration, K. S. Egiyan *et al.*, Phys. Rev. Lett. **96**, 082501 (2006).
- [30] N. Fomin *et al.*, Phys. Rev. Lett. **108**, 092502 (2012).
- [31] Jefferson Lab Hall A Collaboration, F. Benmokhtar *et al.*, Phys. Rev. Lett. **94**, 082305 (2005).
- [32] J. Laget, Physics Letters B **609**, 49 (2005).
- [33] D. Higinbotham, E. Piasetzky, and S. Wood, J.Phys.Conf.Ser. **299**, 012010 (2011), 0908.0062.
- [34] D. Abbott *et al.*, Phys. Rev. Lett. **80**, 5072 (1998).
- [35] K. Garrow *et al.*, Phys. Rev. C **66**, 044613 (2002).
- [36] E97-006 Collaboration, D. Rohe *et al.*, Phys. Rev. C **72**, 054602 (2005).
- [37] Jefferson Lab Hall A Collaboration, M. M. Rvachev *et al.*, Phys. Rev. Lett. **94**, 192302 (2005).
- [38] A. Tang *et al.*, **90**, 042301 (2003).
- [39] Jefferson Lab Hall A Collaboration, R. Shneor *et al.*, Phys. Rev. Lett. **99**, 072501 (2007).
- [40] Jefferson Lab Hall A Collaboration, R. Subedi *et al.*, Science **320**, 1476 (2008).

- [41] D. Day *et al.*, Phys.Rev.Lett. **59**, 427 (1987).
- [42] J. Alcorn *et al.*, Nucl. Instrum. Meth. **A522**, 294 (2004).
- [43] B. Reitz, Hall-A BPM Calibration Procedure, <http://hallaweb.jlab.org/podd/doc/bpm.html>.
- [44] P. Solvignon-Sliifer, E08-014 BCM calibration report, 2012.
- [45] P. V. J. Berthot, Nucl. Phys. News **9**, 12 (1990).
- [46] O. Ravel, 1997.
- [47] Jefferson lab cryogenic group, [wwwold.jlab.org/eng/cryo](http://wwwold.jlab.org/eng/cryo).
- [48] D. Meekins, E08-014 target report, [http://hallaweb.jlab.org/experiment/E08-014/analysis/HallA\\_Target\\_Configuration\\_Apr2011.pdf](http://hallaweb.jlab.org/experiment/E08-014/analysis/HallA_Target_Configuration_Apr2011.pdf), 2011.
- [49] R. Bock and A. Vasilescu, The Particle Detector Brief Book.
- [50] E. Jastrzembski, 1997.
- [51] ROOT/C++ Analyzer for Hall A.
- [52] ROOT - A Data Analysis Framework by CERN, <http://root.cern.ch/drupal/>.
- [53] E08-014 Harp scan results, 2011.
- [54] A. Ketikyan *et al.*, About Shower Detector Software, 1997.
- [55] H. Lu *et al.*, Shower Calibration and Efficiency for E97-110, ShowerCalibrationandEfficiencyforE97-110,[http://hallaweb.jlab.org/experiment/E97-110/tech/shower\\_calib.ps.gz](http://hallaweb.jlab.org/experiment/E97-110/tech/shower_calib.ps.gz)", 2005.
- [56] N. Liyanage, Optics Calibration of the Hall A High Resolution Spectrometers using the new optimizer, <http://hallaweb.jlab.org/publications/Technotes/files/2002/02-012.pdf>, 2002.
- [57] Hall A survey report 1343, <http://www.jlab.org/eng/survalign/documents/dthalla/A1343.pdf>, 2010.
- [58] Hall A survey report A1249, <http://www.jlab.org/eng/survalign/documents/dthalla/A1239.pdf>, 2009.
- [59] Hall A survey report A1239, <http://www.jlab.org/eng/survalign/documents/dthalla/A1249.pdf>, 2009.
- [60] G. Jin, Measurement of the Target Single-Spin Asymmetry in Quasi-Elastic  $^3\text{He}$ , 2011.

- [61] J. Huang, HRS Optics Optimizer, 2009.
- [62] A. Duer, Single Arm Monte Carlo for Polarized 3He experiments in Hall A v.0.2, <http://hallaweb.jlab.org/publications/Technotes/files/2001/01-004.pdf>, 2002.
- [63] H. Yao, Ph.D Thesis, Temple University , 2011.
- [64] J. LeRose, HRS transportation functions.
- [65] V. Sulkosky, Ph.D Thesis, College of William and Mary, 2007.
- [66] P. Bosted and V. Mamyany, Empirical Fit to electron-nucleus scattering, 2012, arXive 1203.2262.
- [67] N. Fomin, Ph.D Thesis, University of Virginia, 2008.
- [68] A. Daniel, Ph.D Thesis, Houston University, 2007.
- [69] R. D. McKeown, Phys. Rev. Lett. **56**, 1452 (1986).
- [70] J. S. O'Connell *et al.*, Phys. Rev. C **35**, 1063 (1987).
- [71] J. Bevelacqua, FIZIKA **1**, 129 (1992).
- [72] J. W. Lightbody and J. S. O'Connell, Comput. Phys. **2**, 57 (1988).
- [73] K. Slifer, Ph.D Thesis, Temple University , 2003.
- [74] W. Armstrong, InSane - QFS model, [http://quarks.temple.edu/~whit/code/InSANE++/html/da/dfc/group\\_xsections.html](http://quarks.temple.edu/~whit/code/InSANE++/html/da/dfc/group_xsections.html).
- [75] P. E. Bosted and M. E. Christy, Phys. Rev. C **77**, 065206 (2008).
- [76] L. W. Mo and Y. S. Tsai, Rev. Mod. Phys. **41**, 205 (1969).
- [77] S. Stein *et al.*, Phys. Rev. D **12**, 1884 (1975).
- [78] S. Covrig, E08-014 Cryogenic Target System Simulation, 2013.